Biomimetics through nanoelectronics: development of three-dimensional macroporous nanoelectronics for building smart materials, cyborg tissues and injectable biomedical electronics.

Biomimetics through nanoelectronics: development of three-dimensional macroporous nanoelectronics for building smart materials, cyborg tissues and injectable biomedical electronics.

A dissertation presented

by

Jia Liu

to

The Department of Chemistry and Chemical Biology

in partial fulfillment of the requirements

for the degree of

Doctor of Philosophy

in the subject of

Chemistry

Harvard University

Cambridge, Massachusetts

April 2014

Research Advisor: Professor Charles M. Lieber Jia Liu

Biomimetics through nanoelectronics: development of three-dimensional macroporous nanoelectronics for building smart materials, cyborg tissues and injectable biomedical electronics.

Abstract

Nanoscale materials enable unique opportunities at the interface between physical and life sciences. The interface between nanoelectronic devices and biological systems makes possible communication between these two diverse systems at the length scale relevant to biological functions. The development of a bottom-up paradigm allows the nanoelectronic units to be synthesized and patterned on unconventional substrates. In this thesis, I will focus on the development of three-dimensional (3D) nanoelectronics, which mimics the structure of porous biomaterials to explore new methods for seamless integration of electronics with other materials, with a special focus on biological tissue.

First, I introduce the fabrication of ultra-flexible macroporous nanoelectronic with 3D structure, porosity larger than 99%, hundreds of addressable nanodevices and feature sizes ranging from 10 micrometers to 10 nanometers. Second, I demonstrate that these nanoelectronics as nanoelectronic scaffolds (nanoES) may be easily integrated with organic gel, polymers and biomaterials without altering their physical/chemical properties. Notably, these devices can have multiple functions in hybrid materials as photodetectors, electrical and chemical sensors, and strain sensors. Third, I present the culture of synthetic tissues within these nanoES to generate “cyborg” tissues, introducing a fundamentally new way to seamlessly integrate nanoelectronics with tissues in 3D to

interrogate tissue activity. The response of cyborg tissue to external drug stimulation or microenvironment pH change can be monitored in real time by the embedded devices. Finally, I report a method by which freestanding macroporous nanoelectronics can be manipulated by syringe injection and self-restore their geometric configuration. The electronics can be injected into *in-vivo* systems to facilitate in a minimally invasive way chronic neuron communications, electrode implantation and active tissue scaffold implantation. Multiplexed recording of brain signals from nanodevices on the scaffold shows promise for studying functional brain activity. The macroporous structure of the scaffold allows reorganization of the tissue within the scaffold and promotes migration of adult neural stem cells from the subventricular zone to the electronics network. Together, these results open up new directions in merging nanoelectronics with living tissue, organs and other systems, bringing many opportunities to fields ranging from smart materials design and brain-machine interface to regenerative medicine.

Table of Contents

Abstract iii

Table of Contents v

Acknowledgements ix

Abbreviations xii

List of Tables and Figures xiii

Chapter 1. Introduction 1

1.1 Synthesis of nanowires as nanoelectronic units 2

1.2 Assembly of nanowires for flexible and 3D high-performance nanoelectronics 4

1.3 Nanoelectronics in biology: interfacing with cells and tissues 8

1.4 Overview of thesis 12

1.5 Bibliography 14

Chapter 2. Three-dimensional macroporous nanoelectronics network 21

2.1 Introduction 21

2.2 Experimental 22

2.2.1 Nanowire synthesis 22

2.2.2 2D and 3D macroporous nanowire nanoelectronic network fabrication…… 22

2.2.3 Freestanding three-layer interconnect ribbon fabrication and mechanical testing 25

2.2.4 3D nanoelectronics structure simulation 28

2.2.5 Characterization of macroporous nanoelectronic networks 28

2.2.6 Electrical measurement of 3D macroporous nanoelectronic networks…….. 28

2.3 Results and discussion 29
2.3.1 Nanoelectronics fabrication and structure characterization 29
2.3.2 Mechanics analysis 34
2.4 Conclusions 36
2.5 Bibliography 37

Chapter 3. Integration of three-dimensional macroporous nanoelectronics with materials 39
3.1 Introduction 39
3.2 Experimental 40
3.2.1 3D macroporous photodetectors and device localization in 3D 40
3.2.2 3D macroporous chemical sensors 40
3.2.3 3D macroporous strain sensors in elastomer 41
3.3 Results and discussion 42
3.4 Conclusion 54
3.5 Bibliography 55

Chapter 4. Three-dimensional macroporous nanoelectronics scaffold for synthetic tissue 57
4.1 Introduction 57
4.2 Experimental 60
4.2.1 Device fabrication and characterization 60
4.2.2 NanoES/tissue scaffold 61
4.2.3 Scaffold mechanical properties 62
4.2.4 Cell culture 64
4.2.5 Immunochemical staining 70
4.2.6 Fluorescent dye labeling of devices and PLGA fibers 71

4.2.7 Hematoxylin-eosin and Masson trichrome staining 71
4.2.8 Optical microscopy and image analysis..... 72
4.2.9 Micro-computed tomography 73
4.2.10 Cell viability assays..... 73
4.2.11 Electrical measurements..... 74
4.3 Results and discussion 75
4.3.1 nanoES characterization..... 75
4.3.2 Mechanical design 80
4.3.3 Characterization of nanoES/tissue scaffold hybrids 82
4.3.4 Characterization of nanoES/tissue interface 85
4.3.5 Monitoring of cellular activity and microenvironment and its change due to external stimulations 89
4.4 Conclusion 94
4.5 Bibliography 95

Chapter 5. Syringe Injectable Electronics 98
5.1 Introduction..... 98
5.2 Experimental..... 99
5.2.1 Nanowire synthesis 99
5.2.2 Freestanding syringe injectable electronics fabrication..... 100
5.2.3 Structure characterization 102
5.2.4 Surface modification of electronics for syringe injectable 103
5.2.5 Mesh structure design 103
5.2.6 Glass needle and fluidic channel preparation 105
5.2.7 Surface-to-volume-ratio calculation 106
5.2.8 Injection by metal gauge needles..... 106
5.2.9 Injection by glass needle..... 107

5.2.10 Yield of injection 108
5.2.11 ACF bonding process 110
5.2.12 Imaging of electronics in glass channel 111
5.2.13 Mechanical simulations 112
5.2.14 Inject electronics in soft matters 116
5.2.15 Inject electronics in Matrigel™ with and without neurons 117
5.2.16 Inject electronics in Matrigel™ with neurons 117
5.2.17 Immunostaining and imaging of neurons and electronics 118
5.2.18 Mouse Surgery 119
5.3 Results and discussion 124
5.3.1 Syringe injectable electronics 124
5.3.2 Parameters for syringe injectable electronics 129
5.3.3 Inject electronic into soft matters 137
5.3.4 Inject electronics into *in-vivo* system 139
5.4 Conclusion 144
5.5 Bibliography 144

Acknowledgements

The life in graduate school has been one of the most important experiences in my life. I would like to express my appreciation to many people who made this possible.

First of all, I would like to thank my advisor, Professor Charles M. Lieber for his advice and inspiration, who has offered me great opportunities and constant inspiration. Professor Lieber is an incredible advisor and a great mentor. I want to thank him for providing invaluable guidance to me in science and research. I admire his constant enthusiasm and persistence for exploring new things and concepts. I greatly appreciate his support, which has been critical to my research at Harvard these years and his patience to help me improve my capability of research, writing and presentation.

My sincere gratitude is also due to members of my Graduate Advising Committee, Professor Xiaowei Zhuang, Professor Daniel Nocera and Professor Sunney Xie for the time they spent discussing my research and giving me invaluable advice for achieving my results, and great support they offered.

I also want to thank Dr. Jinlin Huang, for his valuable advice, tremendous support and trust throughout these years. It is very pleasure to me to work with Jinlin, who is a very experienced person in electronics. His exceptional insights are greatly appreciated.

I would like to acknowledge Professor Bozhi Tian, Professor Quan Qing and Professor Zhe Yu, who gave me great help and bring me into the field of nanoscience, nanoelectronics and nanobiotechnology area. Without them, the work in this thesis would not have been possible achieved. I would like to acknowledge Prof. Tal Dvir, Zengguang

Cheng, Xiaochuan Dai, Wei Zhou, Prof. Xiaojie Duan, Tian-ming Fu and Chong Xie for the fruitful collaborations. The many hours of discussion have enriched my knowledge in many ways. I also want to thank Dr. Ping Xie for his tremendous help for the fabrication, electronics and measurement, Dr. Jun Yao for his inspiration in nanowire assembly and electronics characterization, and Lu Wang and Sirui Zou for their great help in the biomolecular sensing experiments. I would like to thank Zhe Jiang, Thomas Kempa, Hao Yan, Xiaochen Jiang and Prof. Tzahi Cohen-Karni, for their great help in experiments. Discussions with them inspired me in many ways. I also want to thank Robert Day and Max Mankin for their great efforts on maintaining the nanowire growth set-up and bring me lots of tips for the chemical vapor growth. My sincere thanks are also due to James Cahoon, Yongjie Hu, SungWoo Nam, Hwan Sung Choe, Dr. Jang-Ung Park, Dr. Steffen Strehle, Yajie Dong, Ruixuan Gao, Dr. Didier Casanova, Lin Xu, Peter Kruskal, Jae-Hyun Lee, Tao Zhou, Wenshan Zheng and Sean You for the help and support, and making lab such a pleasure place to work. I want to express my great gratitude to Dr. Yue Yang for teaching my skill for neuron cell culture, Jiang He for immunostaining, and Dr. Lihua Jin and Prof. Zhigang Suo for their great help in mechanical simulation and subsequent inspiration for electronics design. I appreciate technical help from Yuan Lu, Jiandong Deng and Steve Shepard, and also the administrative assistance from Purvant Patel, Kathleen Ledyard and Renée Donlon.

I would like to thank my parents for their endless love, unfailing support, tremendous trust and encouragement for all these years of my studies and helped me go through those difficult times.

Finally, I am grateful to all of you who have directly or indirectly contributed to the completion of this work.

Abbreviations

FET	Field-effect transistor
CVD	Chemical vapor deposition
S/D	Source/Drain
SEM	Scanning electron microscopy
I-V	Current-Voltage
PLGA	Poly(lactic-co-glycolic acid)
GFAP	Glial fibrillary acidic protein
DAPI	4',6-diamidino-2-phenylindole
NeuN	Hexaribonucleotide Binding Protein-3
Tuj 1	Anti-beta III tubulin
SVZ	Subventricular zone

List of Tables and Figures

Figure 1-1 Schematic of VLS growth of Si nanowires 3
Figure 1-2 Contact printing nanowire for assembly. 6
Figure 1-3 Intracellular electrical recording by nanowire nanoFET device 9
Figure 2-1 Schematic of mesh nanoES fabrication 25
Figure 2-2 Bending stiffness measurements 27
Figure 2-3 Strategy for preparing 3D macroporous nanoelectronic networks 30
Figure 2-4 Organized 2D and 3D macroporous nanoelectronic networks 31
Figure 2-5 Schematics for bending stiffness calculation 34
Figure 3-1 Strategy for integration of 3D macroporous nanoelectronics with host materials 42
Figure 3-2 3D macroporous photodetectors and device localization 44
Figure 3-3 Localization of 3D macroporous nanoelectronic devices 46
Figure 3-4 3D macroporous chemical sensors 49
Figure 3-5 3D macroporous strain sensors embedded in elastomer 51
Figure 3-6 Calibration of the 3D macroporous nanoelectronic strain sensors 52
Figure 4-1 Integrating nanoelectronics with cells and tissue 60
Figure 4-2 Chip assembly for neuronal 3D cultures 66
Figure 4-3 Schematic of cardiomyocyte 3D culture. 68
Figure 4-4 Schematic of vascular nanoES construct preparation and pH sensing. 70
Figure 4-5 Macroporous and flexible nanowire nanoES. 75
Figure 4-6 Reticular nanowire nanoES. 77
Figure 4-7 Mesh nanowire nanoES 78
Figure 4-8 Device performance characterization. 79

Figure 4-9 Geometry control by design in nanoES. 80
Figure 4-10 Design and fabrication of reticular nanoES. 81
Figure 4-11 Reticular-mesh nanoES. 82
Figure 4-12 Hybrid macroporous nanoelectronic scaffolds 83
Figure 4-13 3D reconstructed confocal fluorescence image of rat hippocampal neurons within a reticular nanoES. 85
Figure 4-14 Fluorescence images of cardiac cell-seeded nanoES. 86
Figure 4-15 Biocompatibility test. 88
Figure 4-16 Multiplexed electrical recording can show cellular heterogeneity in drug response 90
Figure 4-17 Multiplexed 3D recording from hybrid reticular nanoES/neural constructs. 91
Figure 4-18 Synthetic vascular construct by mesh nanoES. 92
Figure 4-19 Synthetic vascular construct enabled for sensing. 94
Figure 5-1 Optical images of electronics structure. 102
Figure 5-2 Schematics of mesh design. 105
Figure 5-3 Loading in needle. 108
Figure 5-4 Bonding process. 111
Figure 5-5 Mechanics of mesh during rolling. 114
Figure 5-6 Concept for injectable electronics. 124
Figure 5-7 Stepwise injection. 126
Figure 5-8 Control of injection process. 127
Figure 5-9 Yield of injection. 128
Figure 5-10 Parameters for injection. 132
Figure 5-11 Mechanical analysis for injection process. 133
Figure 5-12 Control experiments of thin film electronics in needle. 136
Figure 5-13 Injectable electronics in PDMS 138
Figure 5-14 Inject electronics into gel. 139

Figure 5-15 Injectable electronics in biological system. 141

Figure 5-16 Interface between electronics and tissue in in-vivo system. 143

Chapter 1. Introduction

In the past half-century, advances in electronics have been driven by increases in their complexity and performance, and decreases in unit size (Moore's law)[1]. The mainstream microelectronics industry continues to provide ever-increasing performance and functionality and brings new technologies in computing, memory, and telecommunication that change the way we live[2]. These developments have in turn spurred interest in "macroelectronics," which requires the low-cost distribution of nanoelectronic units and circuits over the largest possible area in unconventional configurations, for instance on flexible substrates and in 3D geometries[3]. This new type of electronics is expected to bring new applications in flexible displays and integrated circuits (ICs)[4], from paper-like computers[5-6] to novel methods and solutions for seamless integration of electronics with our daily life or even our bodies (for example, wearable and implantable biomedical electronics)[7-18].

Traditional nanoelectronics fabrication technology mainly relies on the "top-down" paradigm, in which nanostructures of electronic units are patterned by lithography techniques and subsequently etched from single-crystalline bulk materials (for example, silicon wafers)[19-20]. This fabrication paradigm intrinsically precludes the transfer of nanoelectronic units from the rigid wafer to the other substrates. Although several unconventional transfer techniques have been developed[21-22], they are still at an early stage, with operation resolution at the micro- or even millimeter scale, and lack promise for large-scale fabrication and manufacturing. Another possible solution may involve

patterned organic electronic materials instead of inorganic materials[6, 11-13]. Although their flexible properties and fabrication processes are promising for potential use in flexible display and consumer electronic devices, those materials do not offer high performance, and have uncertain reliability for integrated circuits and stability for ambient sensing.

As an alternative, inorganic nanomaterials synthesized through the "bottom-up" paradigm are more promising for this goal[23-26]. In the bottom-up paradigm, nanomaterials are synthesized from the most primitive units, atoms, molecules and nanoclusters, and assembled into complex structures[27-30]. The synthesized nanomaterials can be manipulated in 3D and can be used to make high-performance electronics and sensors, which are patterned on virtually any substrate. In addition, the size of these synthetic nanomaterials is comparable to, or even smaller than, state-of-the-art nanoelectronic units[31].

In addition, nanoelectronic units synthesized by bottom-up methods show great promise for interfacing with biological cells and tissues due to: 1) their nanoscale features, 2) their unique engineered geometry and composition, which is made possible by controlled growth and they cannot be achieved by "top-down" fabrication, and 3) the unprecedented integration of functions in a small volume allowed by synthesized heterostructures. These advantages are reviewed below.

1.1 Synthesis of nanowires as nanoelectronic units

Of all nanoelectronic building blocks for macroelectronics, semiconductor nanowires have the most flexible yet controllable structures and electronic properties for the following reasons: (1) Through rational design of catalyst and precursor, virtually all kinds of semiconductor nanowires can be formed[32-39]; (2) nanowire structure and doping

can be rationally modulated to meet different requirements, which is very difficult to achieve by traditional fabrication technology[40-44] and (3) high-performance electronics can be realized by synthetic nanowire circuits[45-48].

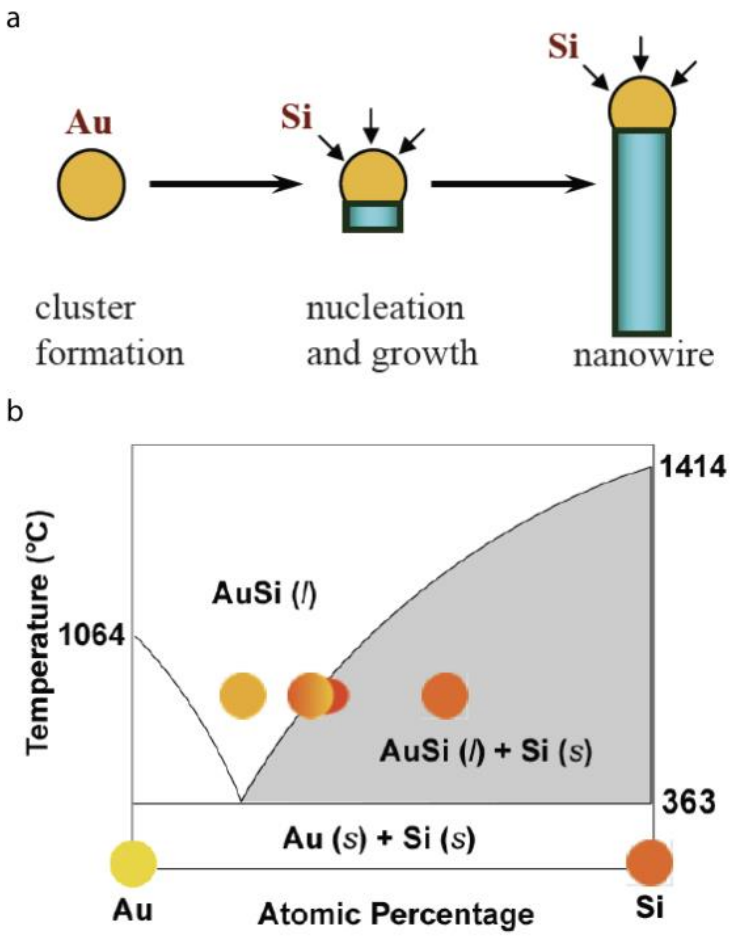

Figure 1-1 Schematic of VLS growth of Si nanowires. **a**, A liquid alloy droplet AuSi is first formed above the eutectic temperature (363 °C) of Au and Si. The continued feeding of Si in the vapor phase into the liquid alloy causes oversaturation of the liquid alloy, resulting in nucleation and directional nanowire growth. **b**, Binary phase diagram for Au and Si illustrating the thermodynamics of VLS growth.

The most general process for synthesis of high quality nanowires is nanocluster-catalyzed vapor-liquid-solid (VLS) growth (**Fig. 1-1**)[49-53]. In this process, the metal nanoclusters are heated to form a liquid solution. The presence of a vapor-phase source of the semiconductor results in nucleation sites for crystallization. The solid-liquid interface

forms the growth interface, causing the continued incorporation of precursor gas and precipitation of semiconductor atoms into the lattice, leading to preferential one-dimensional growth. Different methods have been explored to grow semiconductor nanowires. The chemical vapor deposition (CVD) process is the most popular technique for VLS growth, in which the metal nanocluster serves as a catalyst. In the case of Si nanowire growth, Au nanoparticles serve as catalyst sites where the gaseous precursor silane decomposes to provide semiconductor reactant[26,50]. With appropriate selection of nanocluster catalyst diameter, reactant gases, pressure and temperature, one can easily design nanowire structures *de novo* and synthesize these structures with different modulations of composition, doping defects and geometry[44]. Based on reports in the literature[18, 44, 54-55], virtually all electronic units can be synthesized and implemented into single-nanowire structures *via* the bottom-up paradigm. For example, nanowires involving *p*-*i*-*n* dopant modulation in axial and coaxial geometries have been explored to synthesize nanowire photovoltaics[54]. Branched nanowires involving nanowire heterostructures, including single-crystalline semiconductor groups IV, III-V and II-VI and metals, have been explored to synthesize nanowire light-emitting diodes (LEDs), field-effect transistors (FET) and biosensors[55]. Kinked nanowires, with precise geometry design and dopant modulation in the axial direction, have been utilized in the design of localized FET detectors[18,44].

1.2 Assembly of nanowires for flexible and 3D high-performance nanoelectronics

Due to the rapid pace of development in recent decades, a wide range of semiconductor nanowires have been produced via CVD growth with high carrier mobility, including Ge/Si core-shell nanowires (ca. 730 $cm^2V^{-1}s^{-1}$)[45], GaAs nanowires

(ca. 4100 $cm^2V^{-1}s^{-1}$)[56] and InAs nanowires (ca. 2000 $cm^2V^{-1}s^{-1}$)[57]. Several assembly methods such as flow-directed alignment[58-59], blown-bubble technique[60], Langmuir-Blodgett approaches[30, 61-62] and shear-printing methods[63-65] have been developed to to form large-scale oriented nanowire arrays at room temperature on virtually all kinds of substrates, including silicon wafer, glass, plastics, paper, etc. With standard lithography, nanoelectronic units can be coated with a dielectric layer and connected by metal wires to form electronic circuitry on those substrates[47].

Among the different patterning methods, shear-printing methods, especially the lubricant-assisted contact printing method[64], show great promise due to their ability to assemble nanowires uniformly on large scales (several centimeters) and create high-density individually connected nanowire arrays at high efficiency and with high alignment ratios (ca. 90-95% at a ±5º misalignment angle) (**Fig. 1-2a**). This process uses the nanowire growth substrate as a donor substrate to directionally slide over a receiver substrate, which is pre-treated to affiliate with the nanowire surface chemically or physically. Lubricants such as octane and mineral oils are used between the two substrates to reduce friction. During the contact sliding process, nanowires are detached from the donor substrate by adhesive interactions with the receiver substrate and ultimately realigned by the sliding shear force, resulting in the direct transfer of parallel nanowires to the receiver substrate. After further standard fabrication processes, a well aligned multiple-nanowire device can be fabricated. Through pre-alignment and transfer, McAlpine *et al.*[66] demonstrated the fabrication of chemical sensors on a flexible substrate. Timko *et al.*[67] demonstrated the use of contact printing to assemble silicon nanowires on a polymeric substrate to create nanowire FET arrays for electrical detection

and recording from chicken cardiomyocytes. Multiplexed recording from these arrays recorded signal propagation times across the myocardium with high spatial resolution. Takei *et al.*[68] used a contact printing technique to assembly Ge/Si core-shell nanowire on a polyimide substrate to form fully integrated nanowire active matrix circuitry. Integrating it with pressure-sensitive rubber, they demonstrated this circuitry as electronic "skin" for pressure sensing with lower operation voltages (<5V) than its organic counterparts.

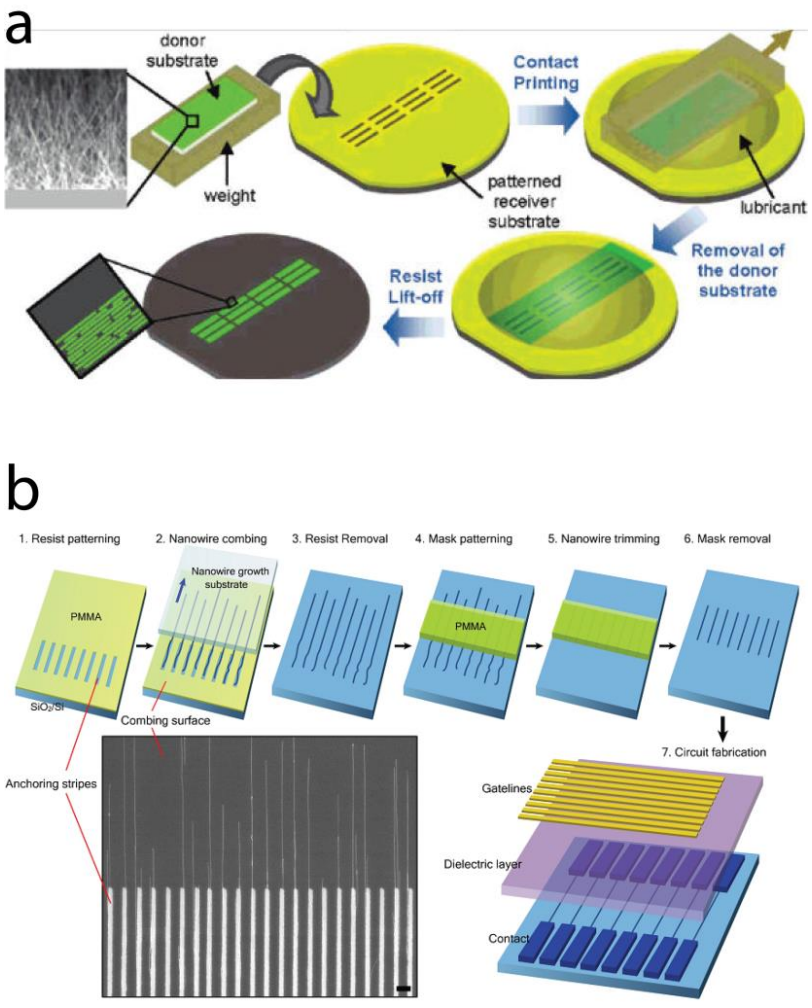

Figure 1-2 Contact printing nanowire for assembly. a, Schematics of contact printing nanowire by lubricant-assisted process (courtesy of Ref. 63). **b**, Schematics and SEM image of contact printing nanowire by deterministic nanocombing (courtesy of Ref . 69).

However, this technique has limitations with respect to fabrication of high-performance single-nanowire electronics. While the process enables large-scale and uniform assembly of nanowires, it lacks the control to precisely integrate individual nanowires at the nanometer scale, causing uneven electronic performance. To further extend the contact printing technique, Yao et al. have recently reported a nanocombing assembly technique[69]. This new technique involves defining regions of a surface that can physically or chemically anchor part of the nanowires and then drawing them out over a region of the surface that has little interaction with the nanowire, to stretch and align nanowires in highly oriented arrays (**Fig. 1-2b**). This method pushes the yield of arrays to greater than 98.5% of the nanowires aligned, to within ±1º of the combing direction. With lithography pre-patterning chemically distinct regions, a deterministic assembly has been demonstrated to produce a high yield of single-nanowire (20-30 nm in diameter) devices on different substrates.

In addition, post-growth assembly of nanowires and patterning techniques allow for the integration of electronic units through a layer-by-layer assembly process[64-65,70], opening up new opportunities for 3D integrated circuits (3D-ICs). 3D-ICs consisting of multiple layers of active electronic units enable more efficient interconnections, higher integration density, faster operation speed and lower power consumption. Moreover, this technology allows for the integration of different materials without the requirement of materials or processing compatibility. As an example, Nam et al. recently demonstrated the integration of the first layer *n*-InAs nanowire with a second layer *p*-Ge/Si core-shell nanowire to form a vertically interconnected 3D complementary metal–oxide–semiconductor (CMOS) inverter by contact printing[65].

Together, these growth and assembly technologies open up new opportunities to realize nanoelectronics on virtually any kind of substrate and 3D interconnections to usher nanoelectronics design into a new era.

1.3 Nanoelectronics in biology: interfacing with cells and tissues

Nanoelectronic detection of biomolecules and recording of cellular electrical activity have been highly successful. The capacity of nanoelectronics for high throughput, scalability and low cost has led to novel analytical devices for disease-marker detection, DNA sequencing and other applications[71-73]. Electrical recording of cellular activity is central to areas ranging from basic biophysical study to medical applications[74-88]. In past decades, glass micropipette intracellular probes and sharp electrode probes have been predominantly used to interface with the internal environment of cells[74-77], and multi-electrode arrays[78-81] and planar FETs[81-88] have been used to interface to and record from electrogenic cells. These technologies are either invasive or lack the ability to record signals in the intracellular and subcellular regions. Moreover, metal-based electrical recording suffers from the limitation of liquid-solid input impedance, which precludes further decrease of detector size[89].

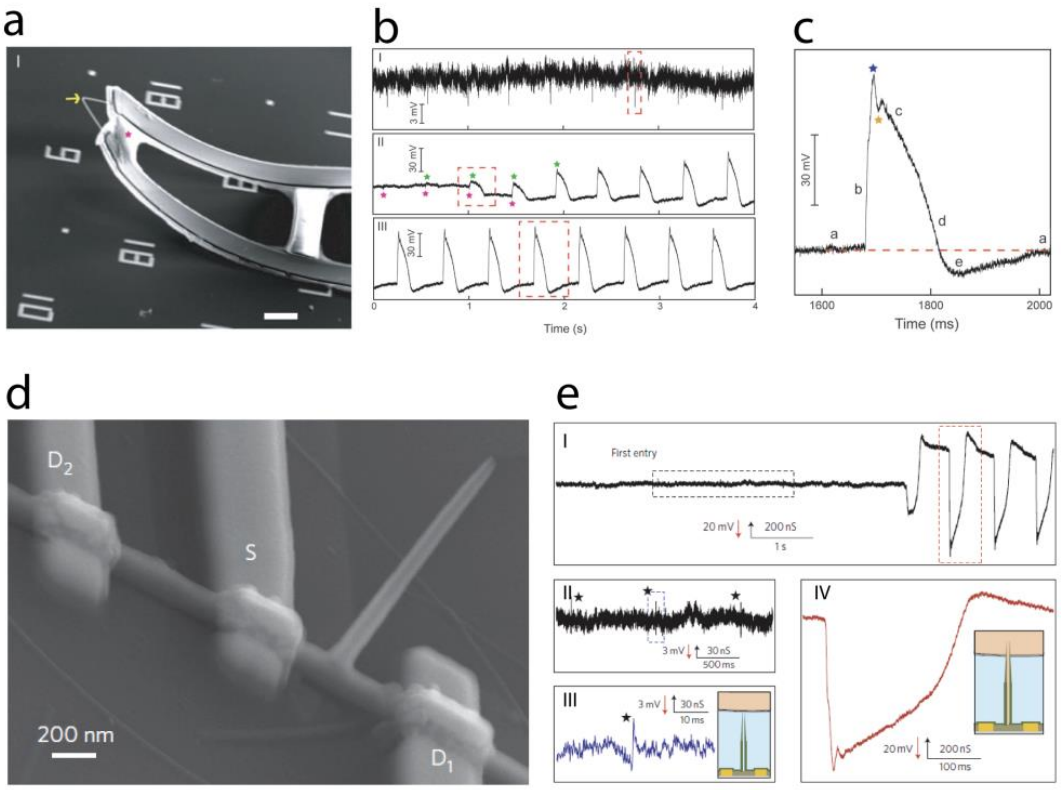

Figure 1-3 Intracellular electrical recording by nanowire nanoFET device. **a**, A 3D, free-standing kinked nanowire FET probe bent up by stress release of the metal interconnects. The yellow arrow and pink star mark the nanoscale FET and SU-8, respectively. Scale bars, 5μm. **b**, Transition from extracellular (**I**) to intracellular recordings during (**II**) cellular entrance recorded by a kinked nanowire FET probe from beating cardiomyocytes. Green and pink stars denote the peak positions of intracellular and extracellular signal components, respectively; (**III**) Steady-state intracellular recording. **c**, Zoom-in signals of an intracellular action potential peak. Blue and orange stars designate features that are possibly associated with inward sodium and outward potassium currents, respectively. The letters 'a' to 'e' denote five characteristic phases of a cardiac intracellular potential, as defined in text. The red-dashed line is the baseline corresponding to intracellular resting state. (Courtesy of Ref. 18). **d**, SEM image of a BIT-FET device (S–D1) and control device (S–D2). **e**, (**I**), Representative trace (conductance versus time) reflecting the transition from extracellular to intracellular recording. (**II**), Magnified view of the trace inside the black dashed rectangle in (**I**). (**III**), Magnified view of the trace inside the blue dashed rectangle in (**II**). The stars in (**II**) and (**III**) mark the position of extracellular spikes. (**IV**), Magnified view of the peak inside the red dashed rectangle in (**I**) (Courtesy of Ref. 93).

Recently, there have been several advances using nanowire-based nanoelectronics to interface with cells. One has been the use of metallic vertical nanowires as detectors to interface with the cells cultured directly on them. Through localized electroporation, the

nanowires can break the cell membrane to form a temporary connection between detectors and the intracellular environment[90-91]. However, this technique is still invasive to cells despite some modifications which allow longer intracellular detection time. Moreover, as mentioned above, metal-based electrical recording probes cannot be made smaller and less invasive without increasing the input impedance. In addition, the amplitude of signal, temporal resolution and signal-to-noise (S/N) are all limited by the sub-microscale size of the detector[89]. Importantly, those vertical metallic nanowires all fail to identify the subthreshold voltage change in action potential recording[90-91]. On the contrary, the FET has proved to be an "active" detector, in which the sensitivity will drop with decreasing detector size[71, 92]. In an FET device, the potential is recorded by measuring the conductance between the source and drain electrodes. The potential applied to the channels of the FET serves as a gate potential changing the carrier density in the FET channels, which leads to conductance change. This process is independent of the input impedance of the FET channels and source-drain electrodes; therefore, the size of the detector does not affect the sensitivity of the FET. As an example of such an FET detector, Tian *et al*. synthesized kinked nanowire with ca. 80-nm diameter and modulated its axial doping to localize a lightly doped nanoscale FET region on the tip of the kink with two metallic arms. Stressed metal contacts were formed to leverage the nanowire into a 3D probe. Phospholipid bilayers were coated on the surface of the kinked nanowire to facilitate the penetration of the nanowire into the cell. Using this nanoFET probe, a full amplitude cardiomyocyte action potential with 75-100 mV was recorded (**Fig. 1-3 a-c**)[18]. Moreover, Duan *et al.*[93] fabricated a silica nanotube, coated with a phospholipid bilayer, on a silicon nanowire to bring the cytosol into contact with the FET region on the bottom

when the tube was inserted into cells (**Fig. 1-3 d-e**). Multiplexed intracellular recordings from a single cell or cellular network have been demonstrated with this technique. Based on these two concepts, several different intracellular electrophysiological recording techniques have been further developed[94-96].

In addition to electrophysiological recording, nanowires and nanowire-related structures have been used for delivery of biomolecular materials into cells that are inaccessible by traditional methods[97-99] to interrogate genomic behavior of cells.

Nanotechnology has also significantly advanced our ability to interrogate tissue structure. Specifically, nanoparticles have been used to image tissue structure and activity *in vitro* and *in vivo*[100-101], and as drug delivery materials to control the release of drugs in tissue[102-103]; micro- and nanofluidic channels have been used to deliver or inject biomolecules and virus vectors to the targeted tissue region[104] and 3D macroporous materials with micro- and nanoscopic features have been developed to build synthetic tissue scaffolds[105].

However, there are surprisingly few reports on the use of nanoelectronics to interface to and interrogate cellular networks and tissues. The difficulties with this approach are that 1) tissue is 3D, irregular flexible structure and 2) in contrast to single cells, tissue is still inaccessible to electronic units, as tissues consist of cells closely packed in a 3D network and surrounded by dense extracellular matrix. Some flexible electronics have been used to interface to the surface of tissue with good attachment and adhesion[16-17, 106-107]. However, the surface of tissue provides only limited information that can also be acquired by optical methods[108]. To be delivered into tissues, nanoelectronics need to be loaded by a rigid substrate so as to mechanically penetrate the tissue, pushing

the sensing or stimulation unit close to cells[109-113]. Importantly, the dimensions of this rigid substrate must be micro- to millimeter scale in order to maintain enough mechanical strength to penetrate the tissue. Consequently, the electronics will occupy a large volume inside the tissue. Furthermore, the mechanical mismatch between rigid substrate and soft tissue will cause chronic damage during long-term implantation and recording, resulting in severe immunoreactivity in the tissue and further degrading the quality of recording and stimulation. At the same time, there is an ever-increasing necessity to deliver and seamlessly integrate nanoelectronic units within tissue in 3D. For example, the integration of billions of sensing units with neuron and cardiac tissue with single-cell addressability to monitor the activity of single neurons in a 3D network in real-time with minimal or no invasiveness is key for brain activity mapping[114-115]. Other examples include a smart 3D drug release system with the ability to sense microenvironment changes throughout tissue[116-117], a 3D in-situ sequencing technique based on integration of nanopore technique with 3D tissue[118-120], and the development of a completely cybernetic organism. These advances would significantly impact the fields of tissue engineering, drug delivery and clinical devices and lead to improvements in clinical medicine and our ability to model disease.

1.4 Overview of thesis

In this thesis, I first propose a fundamentally new idea for the interfacing and integrating nanoelectronics with tissue *in vitro* and *in vivo*. This new approach involves stepwise incorporation of biomimetic and biological elements into a network with addressable, nanoscale-feature units assembled on a centimeter-size scale in a 3D structure. This electronic network mimics the flexible and macroporous structure of the

extracellular matrix, which allows its integration with other soft materials and biomaterials without affecting their physical and chemical properties. I then introduce the culture of cells within tissue scaffolds hybridized with a nanoelectronic network to build a synthetic tissue with nanoelectronic units intrinsically embedded *in vitro* - a cyborg tissue. Finally, I show that the completely freestanding nanoelectronic network can be delivered to and integrated into an *in-vivo* system through a minimally invasive syringe-injection method in which the delivered nanoelectronics unfold within tissue to distribute nanosensors three-dimensionally in the largest possible volume and act as a scaffold to actively guide stem cell growth.

In Chapter 2, I first introduce a new method to pattern and fabricate a real 3D nanoelectronic network. This 3D network is initially fabricated on a 2D sacrificial layer. Using a contact printing technique and lithography patterning, single-nanowire based nanoelectronics are then patterned into regular arrays formed by polymers. Removing the underlying sacrificial layer allows the 2D nanoelectronics to be organized into 3D structures by either external manipulation or internal stress control.

In Chapter 3, I introduce the integration of these 3D nanoelectronic networks with other soft materials such as PDMS and gel. Moreover, use of nanoelectronic units such as photodetectors, chemical sensors and strain sensors will be demonstrated.

In Chapter 4, I focus on transforming the nanoelectronic network into a 3D network that mimics the structure of different extracellular matrices and integrates with synthetic or nature tissue scaffolds to form hybrid nanoelectronic scaffolds. Moreover, neurons and cardiomyocytes are cultured within this hybrid nanoelectronic scaffold to develop a synthetic cellular construct with embedded nanoelectronics. Their potential

application in pharmacology is discussed. Finally, I discuss using this nanoelectronic scaffold alone with smooth muscle cells to build a vascular construct that can act as nanoelectronic blood vessel, and discuss the functions of the nanoelectronic units in this nanoelectronic blood vessel.

In Chapter 5, I focus on how to deliver and integrate this nanoelectronic network into *in-vivo* systems, with emphasis on *in-vivo* brain tissue. Specifically, I introduce a syringe-injection method to deliver the nanoelectronic network. The behavior of the nanoelectronic network in the needle and tissue analogies is discussed. Implantation and the integration of nanoelectronics with brain tissue are analyzed, especially the immunoreactivity of the tissue to the electronics in chronic implantation. Finally, preliminary data are presented which show the promise of nanoelectronics as an active tissue scaffold for guiding the outgrowth of neuron stem cells in the subventricular zone.

1.5 Bibliography

1. Moore, G. *Electronics* **38**, 114 (1965).

2. *International Technology Roadmap for Semiconductors, 2005 Ed.*, www.itrs.net/common/2005ITRS/Home2005.htm.

3. Reuss, R. H., Hopper, D. G. & Park, J. G. *MRS Bull.* **31**, 447 (2006).

4. Gelinck, G. H. et al. *Nat. Mater.* **3**, 106 (2004).

5. Rogers, J. A. *et al. Proc. Natl. Acad. Sci. U. S. A.* **98**, 4835 (2001).

6. Forrest S. R. *Nature* **428**, 911 (2004).

7. Dodabalapur, A. *Mater. Today* **9**, 24 (2006).

8. Someya, T. *et al. Proc. Natl. Acad. Sci. U. S. A.* **102**, 12321 (2005).

9. Yu, G., Gao, J., Hummelen, J. C., Wudi, F. & Heeger, A. J. *Science* **270**, 1789 (1995).

10. Shaheen, S. E., Ginley, D. S. & Jabbour, G. E. *MRS Bull.* **30**, 10 (2005).

11. Ouyang, J., Chu, C. W., Szmanda, C. R., Ma, L. & Yang, Y. *Nat. Mater.* **3**, 918 (2004).

12. Baude, P. F. *et al. Appl. Phys. Lett.* **82**, 3964 (2003).

13. Cantatore, E. *et al. IEEE J. Solid-State Circuits* **42**, 84 (2007).

14. Keefer, E. W., Botterman, B. R., Romero, M. I., Rossi, A. F. & Gross, G. W. *Nat. Nanotechnol.* **3**, 434 (2008).

15. Kim, D. H. *et al. Nat. Mater.* **10**, 316 (2011)

16. Kim, D. H. *et al. Nat. Mater.* **9**, 511 (2010).

17. Kim, D. H. *et al. Science* **333**, 838 (2011).

18. Tian, B. *et al. Science* **329**, 831 (2010).

19. Arns, R. G. *Eng. Sci. Educ. J.* **7**, 233 (1998).

20. Vogel, E. M. *Nat. Nanotechnol.* **2**, 25 (2007).

21. Meitl, M. A. *et al. Nat. Mater.* **5**, 33 (2006).

22. Sun, Y., Kim, S., Adesida, I. & Rogers, J. A. *Appl. Phys. Lett.* **87**, 083501 (2005).

23. Murray, C. B., Kagan, C. R. & Bawendi, M. G. *Ann. Rev. Mater. Sci.* **30**, 545 (2000).

24. Puntes, V. F., Krishnan, K. M. & Alivisatos, A. P. *Science* **291**, 2115 (2001).

25. Iijima, S. *Nature* **354**, 56 (1991).

26. Morales, A. M. & Lieber, C. M. *Science* **279**, 208 (1998).

27. Schreiber, F. *Prog. Surf. Sci.* **65**, 151 (2000).

28. Li, X. S. et al. *Science* **324**, 1312 (2009).

29. Kim, K. S. et al. *Nature* **457**, 706 (2009).

30. Whang, D., Jin, S., Wu, Y. & Lieber, C. M. *Nano Lett.* **3**, 1255 (2003).

31. Lieber, C. M. *MRS Bull.* **28**, 486 (2003).

32. Duan, X. F. & Lieber, C. M. *Adv. Mater.* **12**, 298 (2000).

33. Cui, Y., Duan, X. F., Hu, J. T. & Lieber, C. M. *J. Phys. Chem. B* **104**, 5213 (2000).

34. Yang, P. D. et al. *Adv. Funct. Mater.* **12**, 323 (2002).

35. Hu, J. T., Ouyang, M., Yang, P. D. & Lieber, C. M. *Nature* **399**, 48 (1999).

36. Huang, Y. et al. *Science* **294**, 1313 (2001).

37. Gudiksen, M. S. & Lieber, C. M. *J. Am. Chem. Soc.* **122**, 8801 (2000).

38. Zheng, G. F., Lu, W., Jin, S. & Lieber, C. M. *Adv. Mater.* **16**, 1890 (2004).

39. Zhong, Z. H., Qian, F., Wang, D. L. & Lieber, C. M. *Nano Lett.* **3**, 343 (2003).

40. Yang, C., Zhong, Z. H. & Lieber, C. M. *Science* **310**, 1304 (2005).

41. Gudiksen, M. S., Lauhon, L. J., Wang, J., Smith, D. C. & Lieber, C. M. *Nature* **415**, 617 (2002).

42. Lauhon, L. J., Gudiksen, M. S., Wang, C. L. & Lieber, C. M. *Nature* **420**, 57 (2002).

43. Wang, D., Qian, F., Yang, C., Zhong, Z. H. & Lieber, C. M. *Nano Lett.* **4**, 871 (2004).

44. Tian, B. Z., Xie, P., Kempa, T. J., Bell, D. C. & Lieber, C. M. *Nat. Nanotechnol.* **4**, 824 (2009).

45. Xiang, J. *et al. Nature* **441**, 489 (2006).

46. Lu, W. & Lieber, C. M. *J. Phys. D-Appl. Phys.* **39**, R387 (2006).

47. Yan, H. *et al. Nature* **470**, 240 (2011).

48. Yao, J., Yan, H., Das, S., Klemic, J., Ellenbogen, J. & Lieber, C. M. *Proc. Natl. Acad. Sci. USA* **111**, 2431 (2014).

49. Duan, X. F. & Lieber, C. M. *J. Am. Chem. Soc.* **122**, 188 (2000).

50. Liu, J. L., Cai, S. J., Jin, G. L., Thomas, S. G. & Wang, K. L. *J. Cryst. Growth* **200**, 106 (1999).

51. Wu, Y. Y. & Yang, P. D. *J. Am. Chem. Soc.* **123**, 3165 (2001).

52. Wu, Y. *et al. Nano Lett.* **4**, 433 (2004).

53. Hansen, M. & Anderko, K. *Constitution of binary alloys.* (McGraw-Hill, 1958).

54. Tian, B. *et al. Nature* **449**, 885 (2007).

55. Jiang, X. *et al. Proc. Natl. Acad. Sci. USA* **108**, 12212 (2011).

56. Fortuna, S. A. & Li, X. *IEEE Electron Device Lett.* **30**, 593 (2009).

57. Jiang, X., Xiong, Q., Nam, S., Qian, F., Li, Y. & Lieber, C. M. *Nano Lett.* **7**, 3214 (2007).

58. Duan, X. F., Niu, C. M., Sahi, V., Chen, J., Parce, J. W., Empedocles, S. & Goldman, J. L. *Nature* **425**, 274 (2003).

59. Huang, Y., Duan, X. F., Wei, Q. Q. & Lieber, C. M. *Science* **291**, 630 (2001).

60. Yu, G., Cao, A. & Lieber, C. M. *Nat. Nanotechnol.* **2**, 372 (2007).

61. Tao, A. R., Huang, J. & Yang, P. *Acc. Chem. Res.* **41**, 1662 (2008).

62. Wang, D. W., Chang, Y. L., Liu, Z. & Dai, H. *J. Am. Chem. Soc.* **127**, 11871 (2005).

63. Fan, Z. *et al. Nano Lett.* **8**, 20 (2008).

64. Javey, A., Nam, S., Friedman, R. S., Yan, H. & Lieber, C. M. *Nano Lett.* **7**, 773 (2007).

65. Nam, S., Jiang, X., Xiong, Q., Ham, D. & Lieber, C. M. *Proc. Natl. Acad. Sci. USA* **106**, 21035 (2009).

66. McAlpine, M. C., Ahmad, H., Wang, D. & Heath, J. R. *Nat. Mater.* **6**, 379 (2007).

67. Timko, B. P. *et al. Nano Lett.* **9**, 914 (2009).

68. Takei, K. *et al. Nat. Mater.* **9**, 821-826 (2010).

69. Yao, J., Yan, H. & Lieber, C. M. *Nat. Nanotechnol.* **8**, 329 (2013).

70. Ahn, J. H. *et al. Science* **314**, 1754 (2006).

71. Zheng, G. F., Patolsky, F., Cui, Y., Wang, W. U. & Lieber, C. M. *Nat. Biotechnol.* **23**, 1294 (2005).

72. Venkatesan, B. M. & Bashir, R. *Nat. Nanotechol.* **6**, 615 (2011).

73. Rothberg, J. M. *et al. Nature* **475**, 348 (2011).

74. Hille, B. *Ion channels of excitable membranes* (Sinauer Associates, Inc. 2001).

75. Zipes D. P. & Jalife, J. *Cardiac electrophysiology: From cell to bedside*. (Saunders, 2004).

76. Dhein, S., Mohr, F. W. & Delmar, M. *Practical methods in cardiovascular research*. (Springer, 2005).

77. Davie, J. T., Kole, M. H. P., Letzkus, J. J., Rancz, E. A., Spruston, N., Stuart, G. J. & Häusser, M. *Nat. Protocols* **1**, 1235 (2006).

78. Halbach, M. D., Egert, U., Hescheler, J. & Banach, K. *Cell. Physiol. Biochem.* **13**, 271 (2003).

79. Meyer, T., Boven, K. H., Gunther, E. & Fejtl, M. *Drug Safety* **27**, 763 (2004).

80. Erickson, J., Tooker, A., Tai, Y. C. & Pine, J. *J. Neurosci. Method.* **175**, 1 (2008).

81. Law, J. K. Y., Yeung, C. K., Hofman, B., Ingebrandt, S., Rudd, J. A., Offenhäusser, A. & Chan, M. *Physiol. Meas.* **30**, 155 (2009).

82. Ingebrandt, S., Yeung, C.-K., Krause, M. & Offenhausser, A. *Biosens. Bioelectron.***16**, 565 (2001).

83. Yeung, C.-K., Ingebrandt, S., Krause, M., Offenhausser, A. & Knoll, W. *J. Pharmacol. Toxicol. Meth.* **45**, 207 (2001).

84. Cohen, A., Shappir, J., Yitzchiak, S. & Spira, M. E. *Biosens. Bioelectron.* **22**, 656 (2006).

85. Cohen, A., Shappir, J., Yitzchaik, S. & Spira, M. E. *Biosens. Bioelectron.* **23**, 811 (2008).

86. Lu, Z.-L., Pereveraev, A., Liu, H.-L., Weiergräber, M., Henry, M., Krieger, A., Smyth, N., Hescheler, J. & Schneider, T. *J. Electrocardiology* **14**, 11 (2004).

87. Reppel, M., Pillekamp, F., Lu, Z. J., Halbach, M., Brockmeier, K., Fleischmann, B. K. & Hescheler, J. *J. Electrocardiology* **37**, 104 (2004).

88. Fromherz, P. *ChemPhysChem* **2**, 276 (2002).

89. Spira, M. E. & Hai, A. *Nat. Nanotechnol.* **8**, 83 (2013).

90. Xie, C., Lin, Z., Hanson, L., Cui, Y. & Cui, B. *Nat. Nanotechnol.* **7,** 185 (2012).

91. Robinson, J. T. *et al. Nat. Nanotechnol.* **7,** 180 (2012).

92. Cui, Y., Wei, Q., Park, H. & Lieber, C. M. *Science* **293**, 1289 (2001).

93. Duan, X. *et al. Nat. Nanotechnol.* **7,** 174 (2012).

94. Gao, R. *et al. Nano Lett.* **12,** 3329 (2012).

95. Qing, Q., Jiang, Z., Xu, L., Gao, R., Mai, L. & Lieber, C. M. *Nat. Nanotechnol.* **9**, 142 (2014).

96. Jiang, Z., Qing, Q., Xie, P., Gao, R. & Lieber, C. M. *Nano Lett.* **12**, 1711 (2012).

97. Shalek, A. K. *et al. Proc. Natl. Acad. Sci. USA* **107**, 1870 (2010).

98. Shalek, A. K. *et al. Nano Lett.* **12**, 6498 (2012).

99. Yosef, N. *et al. Nature* **496,** 461 (2013).

100. Empedocles, S. A. & Bawendi, M. G. *Science* **278**, 2114 (1997).

101. Michalet, X. *et al. Science*, **307**, 538 (2005).

102. Langer, R. *Nature*, **392**, 5 (1998).

103. Farokhzad, O. C. & Langer, R. *ACS Nano*, **3**, 16 (2009).

104. Retterer, S. T., Smith, K. L., Bjornsson, C. S., Neeves, K. B., Spence, A. J. H., Turner, J. N., Shain, W. & Isaacson, M. S. *IEEE Trans. Biomed. Eng.* **51**, 2063 (2004).

105. Dvir, T., Timko, B. P., Kohane, D. S. & Langer R. *Nat. Nanotechnol.* **6**, 13 (2011).

106. Viventi, J. *et al. Sci. Transl. Med.* **2**, 24ra22 (2010).

107. Viventi, J. *et al. Nat. Neurosci.* **14**, 1599 (2011).

108. Denk, W., Strickler, J. H. & Webb, W. W. *Science* **248**, 73 (1990).

109. Jones, K., Campbell, P. & Normann, R. *Ann. Biomed. Eng.* **20**, 423 (1992).

110. K. Bradley, *Pain Med.* **7**, S27 (2006).

111. Harnack, D., Winter, C., Meissner, W., Reum, T., Kupsch, A. & Morgenstern, R. *J. Neurosci. Meth.* **138**, 207 (2004).

112. Kerns, J. M., Fakhouri, A. J., Weinrib, H. P. & Freeman, J. A. *Neuroscience* **40**, 93 (1991).

113. Merrill, D. R., Bikson, M. & Jefferys, J. G. R. *J. Neurosci. Meth.* **141**, 171 (2005).

114. Alivisatos, A. P., Chun, M., Church, G. M., Greenspan, R. J., Roukes, M. L, Chun, M. & Yuste, R. *Neuron* **74**, 970 (2012).

115. Alivisatos, A. P. *et al. ACS Nano* **7**, 1850 (2013).

116. Ionescu, L. C., Lee, G. C., Sennett, B. J., Burdick, J. A. & Mauck, R. L. *Biomaterials* **31**, 4113 (2010).

117. Cao, H. Q., Jiang, X., Chai, C. & Chew, S. Y. *J. Cont. Release* **144**, 203 (2010).

118. Deisseroth, K. *Biol. Psychiatry* **71**, 1030 (2012).

119. Zamft, B. M., *et al. PLoS One* **7**, e43876 (2012).

120. Lee, J. H. *et al. Science* **343**, 1360 (2014).

Chapter 2. Three-dimensional macroporous nanoelectronics network

2.1 Introduction

Seamlessly merging functional electronic circuits in a minimally-invasive manner with host materials in 3D could serve as a pathway for creating "very smart" systems because this would transform conventional inactive materials into active systems. For example, embedded electronic sensor circuitry could monitor chemical, mechanical or other changes throughout a host material, thus providing detailed information about the host material's response to external environments as well as desired feedback to the host and external environment[1-2]. To achieve this goal, the addressable electronics should be firstly macroporous, not planar, to enable 3D interpenetration with the host materials. Second, to minimize invasiveness of the macroporous electronic network it must have (1) microscale to nanoscale feature sizes, (2) a small filling fraction with respect to the host (e.g., $\leq 1\%$), (3) comparable or softer mechanical properties than the host, and (4) an inert chemical response within the host material.

The constraints outlined above require the utilization of 3D nanoelectronic networks that are macroporous and have active elements (nanodevices). Two basic methods have been used to fabricate 3D integrated electronic circuits. The first involves bonding substrates, each containing devices/circuits integrated in 2D, together in a 3D stack[3-4]. The second exploits bottom-up assembly of nanoelectronic elements in a layer-by-layer manner[5-7]. However, both methods yield solid or nonporous 3D structures that

only allow the top-most layer of electronic elements to be merged directly with a second material and thus precluding integration of all of the electronic elements seamlessly with a host material in 3D. Here, we introduce a general strategy for preparing a 3D macroporous nanoelectronic network that contains regular arrays of addressable nanowire nanoelectronic elements distributed and patterned in 3D structure.

2.2 Experimental

2.2.1 Nanowire synthesis

Uniform 30 nm p-type silicon nanowires were synthesized using reported methods (37). Single-crystalline nanowires were synthesized using the Au nanocluster-catalyzed vapor-liquid-solid growth mechanism in a home-built chemical vapor deposition (CVD) system described previously[8]. Au nanoclusters (Ted Pella Inc., Redding, CA) with 30 nm diameters were dispersed on the oxide surface of silicon/SiO_2 substrates (600 nm oxide) and placed in the central region of a quartz tube CVD reactor system. In a typical synthesis, the total pressure was 40 torr and the flow rates of SiH_4, diborane (B_2H_6, 100 p.p.m. in H_2), and hydrogen (H_2, Semiconductor Grade), were 2, 2.5 and 60 standard cubic centimetres per minute (SCCM), respectively. The silicon-boron feed-in ratio was 4000:1, and the total nanowire growth time was 30 min.

2.2.2 2D and 3D macroporous nanowire nanoelectronic network fabrication

The 3D macroporous nanowire nanoelectronic networks was initially fabricated on the oxide or nitride surfaces of silicon substrates (600 nm SiO_2 or 100 nm SiO_2/200 Si_3N_4, *n*-type 0.005 V·cm, Nova Electronic Materials, Flower Mound, TX) prior to relief from the substrate. Key steps (**Fig. 2-1**) used in the fabrication of the 3D macroporous

nanowire nanoelectronic networks were as follows: (1) lithography and thermal deposition were used to pattern a 100 nm nickel metal layer, where the nickel served as the final relief layer for the 2D free-standing macroporous nanowire nanoelectronic networks. (2) A 300-500 nm layer of SU-8 photoresist (2000.5, MicroChem Corp., Newton, MA) was deposited over the entire chip followed by pre-baking at 65 ^{o}C and 95 ^{o}C for 2 and 4 min, respectively, then (3) the synthesized nanowires were directly printed from growth wafer over the SU-8 layer by the contact printing methods reported previously[6]. (4) Lithography (photolithography or electron beam lithography) was used to define regular patterns on the SU-8. After post-baking (65 ^{o}C and 95 ^{o}C for 2 and 4 min, respectively), SU-8 developer (MicroChem Corp., Newton, MA) was used to develop the SU-8 pattern. Those areas exposed to UV light or electron beam became dissolvable to SU-8 developer and other areas were dissolved by SU-8 developer. Those nanowires on the non-exposed area will be removed by further washing away in isopropanol solution (30 s) for twice leaving those selected nanowires on the regular pattern SU-8 structure. The SU-8 patterns were curing at 180 ^{o}C for 20 min. (5) A 300-500 nm layer of SU-8 photoresist was deposited over the entire chip followed by pre-baking at 65 ^{o}C and 95 ^{o}C for 2 and 4 min, respectively. Then lithography was used to pattern the bottom SU-8 layer for passivating and supporting the whole device structure. The structure was post-baked, developed and cured by the same procedure as described above. (6) Lithography and thermal deposition were used to define and deposit the metal contact to address each nanowire device and form interconnections to the input/output pads for the array. For the mesh device, in which the metal is non-stressed, symmetrical Cr/Pd/Cr (1.5/50-80/1.5 nm) metal was sequentially deposited followed by metal lift-off in acetone. For the self-

organized networks, in which the metals are stressed, nonsymmetrical Cr/Pd/Cr (1.5/50-80/50-80 nm) metal was sequentially deposited followed by metal lift-off in acetone. (7) A 300-500 nm layer of SU-8 photoresist was deposited over the entire chip followed by pre-baking at 65 ^{o}C and 95 ^{o}C for 2 and 4 min, respectively. Then lithography was used to pattern the top SU-8 layer for passivating the whole device structure. The structure was post-baked, developed and cured by the same procedure as described above. (8) The 2D macroporous nanowire nanoelectronic networks was released from the substrate by etching of the nickel layer (Nickel Etchant TFB, Transene Company Inc., Danvers, MA) for 60-120 min at 25 ^{o}C. (9) The 3D macroporous nanowire nanoelectronic networks were dried by a critical point dryer (Autosamdri 815 Series A, Tousimis, Rockville, MD) and stored in the dry state prior to use.

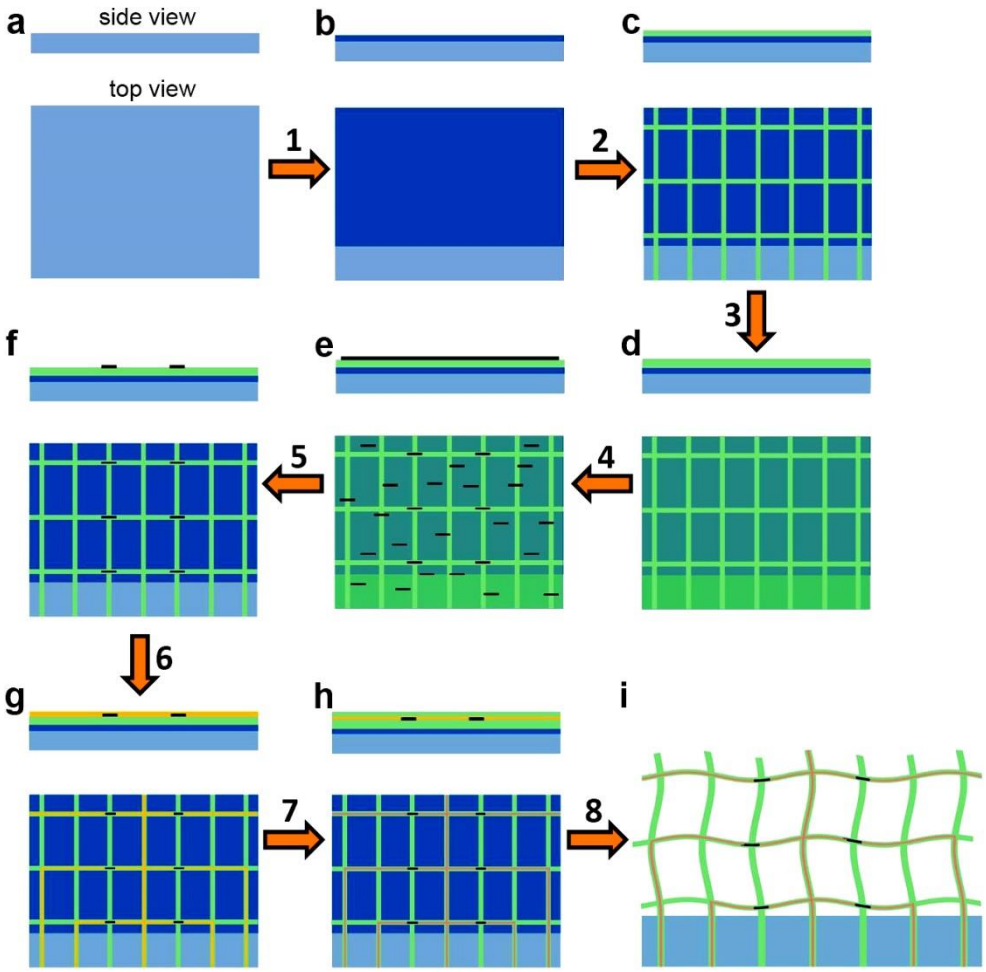

Figure 2-1 Schematic of mesh nanoES fabrication. Components include silicon wafer (cyan), nickel relief layer (blue), polymer ribbons (green), metal interconnects (gold) and silicon nanowires (black). The width of the polymer ribbons was 10-40 μm. Symmetrical Cr/Pd/Cr (1.5/50-100/1.5 nm) metals and asymmetrical Cr/Pd/Cr (1.5/50-100/50 nm) defined by photolithography were used as the minimally stressed nanowire interconnects. 3D device constructs were made by manual folding or rolling by internal stress of the mesh electronics after the step of (**i**).

2.2.3 Freestanding three-layer interconnect ribbon fabrication and mechanical testing

A Ni sacrificial layer was defined on a SiO_2/Si substrate (600nm SiO_2, *n*-type silicon 0.005 V·cm, Nova Electronic Materials, Flower Mound, TX) by EBL and thermal deposition. SU-8/metal/SU-8 elements with 100 μm long and 5 μm wide segments over the Ni-layer and wider segments directly on substrate were defined by EBL using the

same approach described above. In brief, a 500-nm-thick SU-8 layer was deposited by spin coating and defined by EBL to serve as the bottom SU-8 layer. Then EBL, thermal deposition and lift-off were used to define an asymmetrical metal layer consisting of a 3-μm-wide Cr/Pd/Cr (1.5/80/50 nm) ribbon centered on the bottom SU-8 element. Last, the top 500 nm thick SU-8 layer of the SU-8/metal/SU-8 elements were defined, and then the Ni sacrificial layer was removed by Ni etchant, where the final drying step was carried out by critical point drying (Autosamdri 815 Series A, Tousimis, Rockville, MD). A schematic and an optical image of the resulting sample element are shown in **Figure 2-2a** and **Figure 2-2b**, respectively. An atomic force microscope (AFM, MFP 3D, Asylum Corp.) was used to measure force versus displacement curves for the SU-8/metal/SU-8 elements (**Fig. 2-2a**). The tip of the AFM was placed at the free end of the ribbon element and then the applied force and displacement were recorded while the AFM tip was translated down (loading) and then up (unloading), with a typical data shown in **Figure 2-2c**. The spring constant of the AFM cantilever/tip assemblies used in the measurements were calibrated by measuring the thermal vibration spectrum[9].

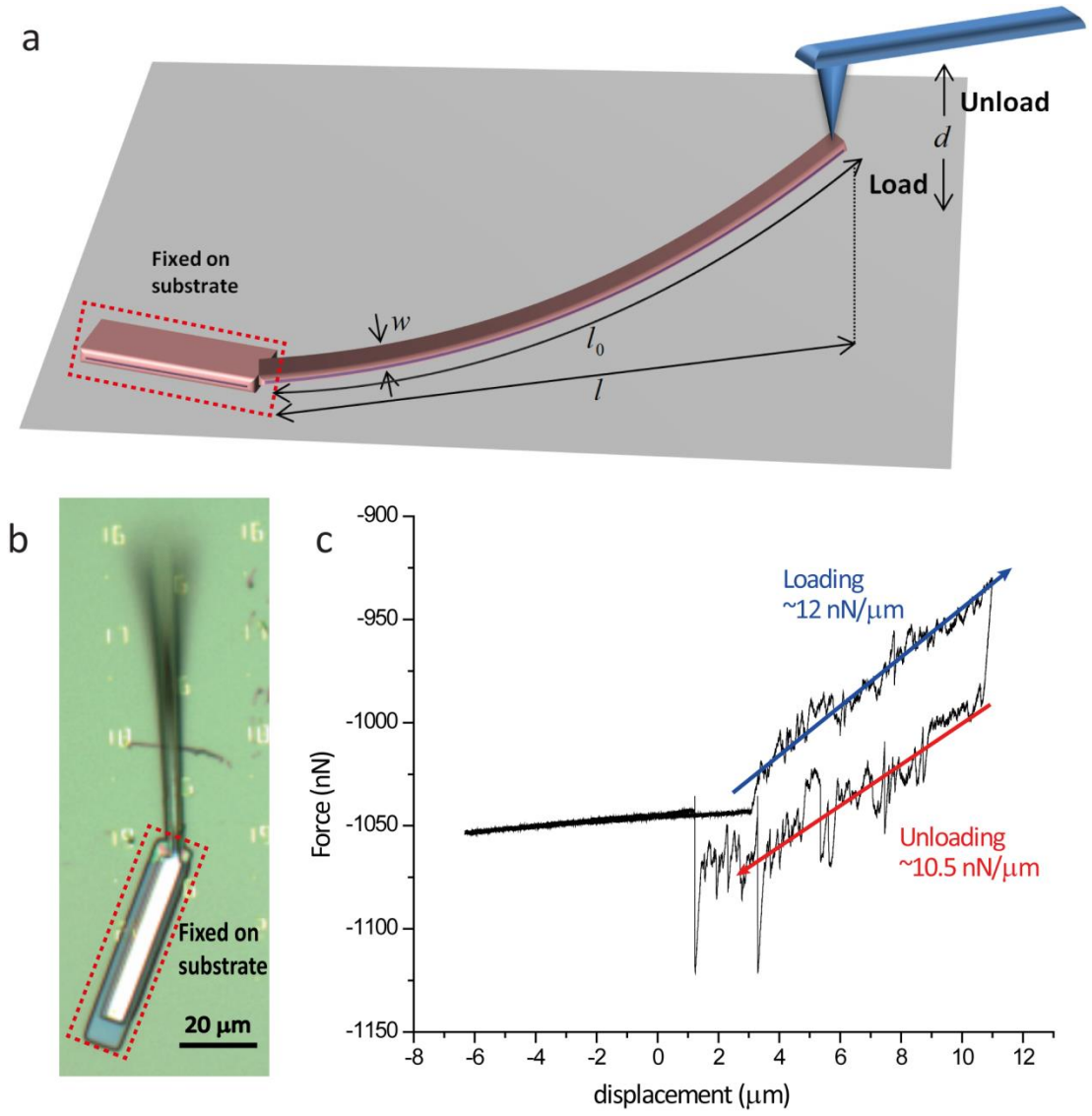

Figure 2-2 Bending stiffness measurements. **a**, Schematic illustrating the measurement of the bending stiffness of a representative SU-8/metal/SU-8 element in the macroporous nanoelectronic networks. EBL is used to define substrate-fixed and substrate free beams, where internal stress in the central metal layer causes the structure to bend-up upon relief from the substrate. The tip of the AFM is placed at the free end of the ribbon, and then translated vertically downward (loading) and upward (unloading) to yield the force-displacement curves. In the scheme, *w*: the width of the ribbon, l_0: the length of the ribbon, *l*: the projected length of the ribbon and *d*: the displacement of the AFM tip. **b**, Optical micrograph of the fabricated structural element, where the substrate fixed portion is highlighted by the red dashed rectangle and the free beam is in the upper portion of the image with a width of 5 μm and a length of 100 μm. **c**, A typical force – displacement curve with *F*/*d* for loading and unloading of 12 and 10.5 nN/μm, respectively. Similar deviation between the loading and unloading has been attributed to inelastic deformation[30]; hence, we use the larger loading value in calculations to provide an upper limit.

2.2.4 3D nanoelectronics structure simulation

The self-organization of the mesh structure due to residual stress was simulated by the commercial finite element software ABAQUS. Both the SU-8 ribbons and the SU-8 / metal ribbons were modeled as beam elements. The cross-sectional property of the SU-8 / metal ribbons was defined by the appropriate meshed beam cross-section, while the cross-sectional property of the SU-8 ribbons was set by defining the relevant rectangular profile. The equivalent bending moment on SU-8/metal ribbons was calculated using the residual stress measured by MET-1 FLX-2320-S thin film stress measurement system, which were 1.35 and 0.12 Gpa for Cr (50 nm) and Pd (75 nm), respectively.

2.2.5 Characterization of macroporous nanoelectronic networks

Scanning electron microscopy (SEM, Zeiss Ultra55/Supra55VP field-emission SEMs) was used to characterize the macroporous nanoelectronic networks. Bright-field and dark-field optical micrographs of samples were acquired on an Olympus FSX100 system using FSX-BSW software (ver. 02.02). Fluorescence images of the 3D macroporous nanoelectronic networks were obtained by doping the SU-8 resist solution with Rhodamine 6G (Sigma-Aldrich Corp., St. Louis, MO) at a concentration less than 1 μg/mL before deposition and patterning. *ImageJ* (ver. 1.45i, Wayne Rasband, National Institutes of Health, USA) was used for 3D reconstruction and analysis of the confocal and epi-fluorescence images.

2.2.6 Electrical measurement of 3D macroporous nanoelectronic networks

Nanowire device recording was carried out with a 100 mV DC source voltage, and the current was amplified with a home-built multi-channel current/voltage

preamplifier with a typical gain of 10^6 A/V. The signals were filtered through a home-built conditioner with band-pass of 0-3 kHz, digitized at a sampling rate of 20 kHz (Axon Digi1440A) and recorded using Clampex 10 software (MDS). The nanowire FET conductance and transconductance (sensitivity) were measured in 1× PBS as described previously[10]. The slope of a linear fit to conductance versus water-gate potential (V_{gate}) data was used to determine transconductance. Ag/AgCl reference electrodes were used in all recording experiments.

2.3 Results and discussion

2.3.1 Nanoelectronics fabrication and structure characterization

We have focused on a bottom-up approach for realizing 3D macroporous nanoelectronic networks in **Figure 2-3**. In this approach, we utilize functional nanowire nanoelectronic elements (**Fig. 2-3a**), where variations in composition, morphology and doping encoded during synthesis[11-19] define diverse functionality including devices for logic and memory[20,21], sensors[18,23], light-emitting diodes[17], and energy production and storage[24,25]. The macroporous nanoelectronic network with chosen nanowire elements (**Fig. 2-3b**) is realized through a combination of nanowire assembly and conventional 2D lithography carried out on a sacrificial substrate (see below); removal of the sacrificial layer yields free-standing and flexible 2D macroporous nanoelectronic networks (**Fig. 2-3b**). The 2D macroporous nanoelectronic networks are organized into 3D macroporous structures by either self- or directed-assembly.

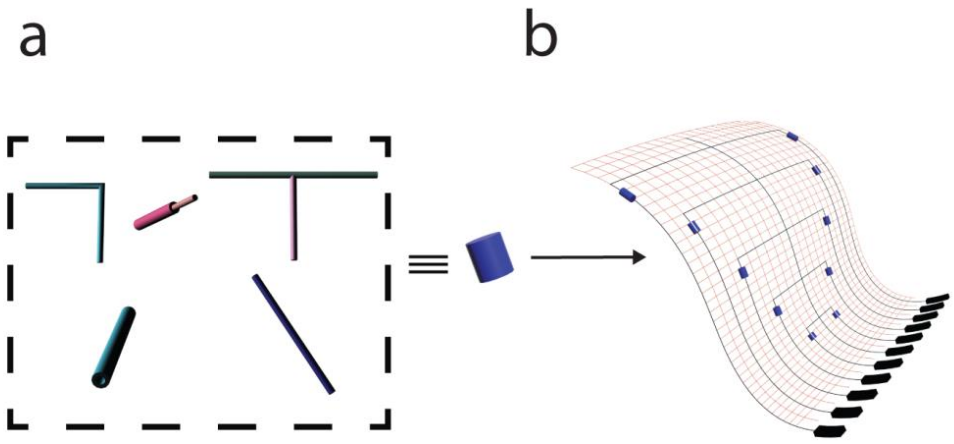

Figure 2-3 Strategy for preparing 3D macroporous nanoelectronic networks. **a**, Different nanowire nanoelectronic elements (from left to right): kinked nanowire, nanotube, core-shell, straight and branched nanowire. **b**, Free-standing 2D macroporous nanowire nanoelectronic "precursor". Blue: nanoelectronic element, orange: passivation polymer, black: metal contact and input/output (I/O).

The key steps involved in the fabrication, 3D organization and characterization of the macroporous nanoelectronic networks are outlined in **Figure 2-4**. First, nanowires were uniaxially-aligned by contact printing[14] on the surface of a layer of SU-8 negative resist, where the SU-8 was deposited by spin-coating on a Ni sacrificial layer deposited on a carrier substrate (**Fig. 2-4a, I**). Second, the SU-8 layer with aligned nanowires was patterned to define a periodic array by photolithography or electron beam lithography (EBL), and the excess nanowires on unexposed regions of the SU-8 were removed when the pattern was developed (**Fig. 2-4a, II**). The nanowire density and feature size in periodic arrays were chosen such that each element contained on average 1-2 nanowires. Third, a second SU-8 layer was deposited and patterned in a mesh structure by lithography (**Fig. 2-4a, III**). This SU-8 mesh serves to interconnect the nanowire/SU-8 periodic features and provides an adjustable support structure to tune the mechanical properties. Fourth, metal interconnects were defined by standard lithography and metal deposition on top of the appropriate regions of the SU-8 mesh, such that the end of

nanowires were contacted and the nanowire elements were independently addressable (**Fig. 2-4a, IV**). Last, a third SU-8 layer was lithographically patterned to cover and passivate the metal interconnects.

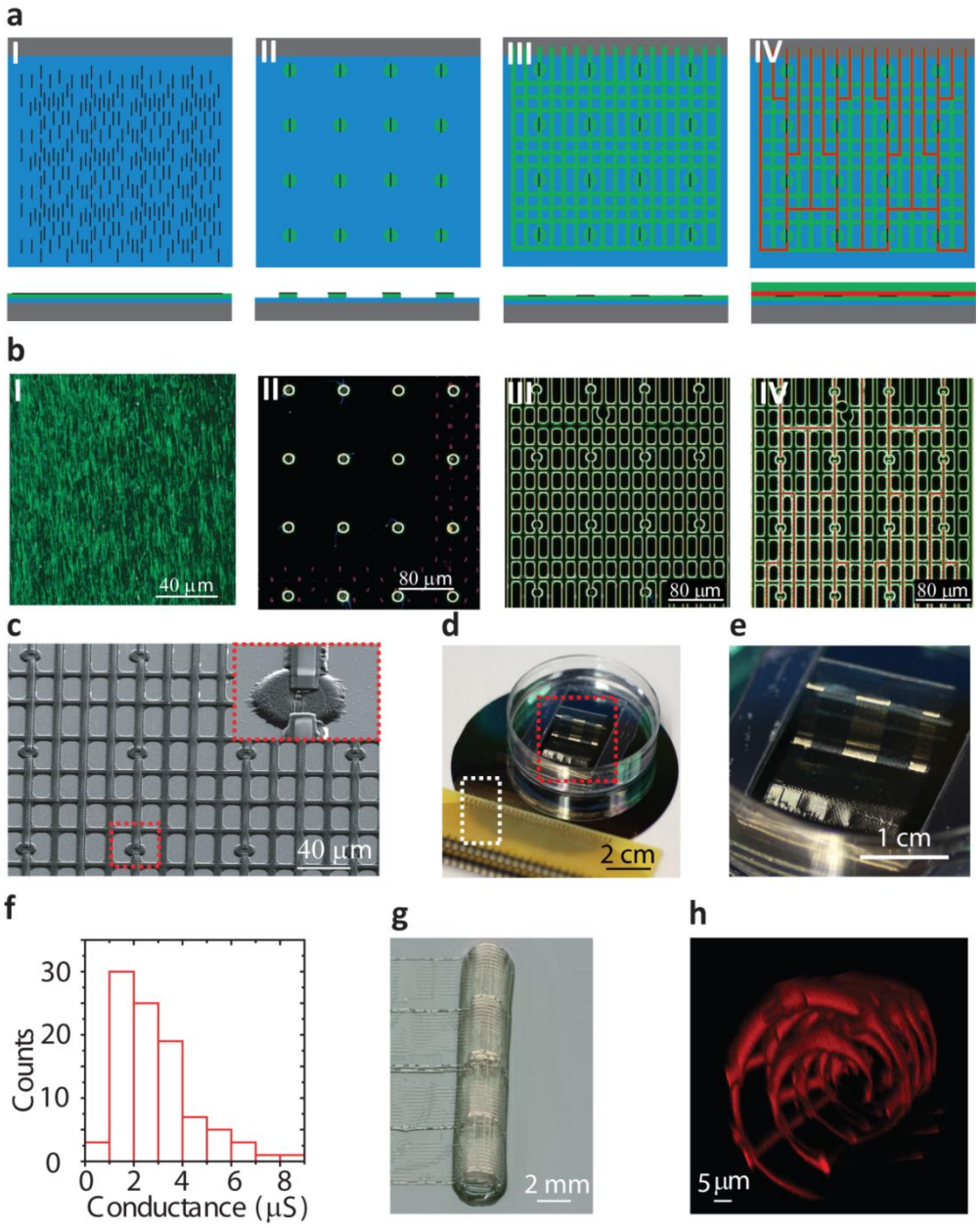

Figure 2-4 Organized 2D and 3D macroporous nanoelectronic networks. **a**, Schematics of nanowire registration by contact printing and SU-8 patterning. Gray: Silicon wafer, blue: Ni sacrificial layer, black ribbon: nanowire, green: SU-8, red: metal contact. (Top) shows top view and (bottom) shows side view. (**I**): Contact printing nanowire on SU-8. (**II**): Regular SU-8 structure was patterned by lithography to

(Continued) immobilize nanowires. Extra nanowires were washed away during the develop process of SU-8. (**III**): Regular bottom SU-8 structure was patterned by spin-coating and lithography. (**IV**): Regular metal contact was patterned by lithography and thermal evaporation, followed by top SU-8 passivation. **b**, Dark field optical images corresponding to each step of schematics in (**a**). The nanowire and SU-8 features appear green in these images. The small red features on the right and lower edges of the image in (**II**) correspond to metal lithography markers used in alignment. The red dashed line highlights metal contacts/interconnects in (**IV**). **c**, SEM image of a 2D macroporous nanoelectronic network prior to release from the substrate. Inset, corresponds to zoom-in of the region enclosed by the red dashed box containing a single nanowire device. **d**, Photograph of wire-bonded free-standing 2D macroporous nanoelectronic network in petri-dish chamber for aqueous solution measurements. The red dashed box highlights the free-standing portion of the nanoelectronic network and the white-dashed box encloses the wire-bonded interface between the input/output (I/O) and PCB connector board. **e**, Zoom-in of the region enclosed by the red-dashed box in (**d**). **f**, Histogram nanowire device conductance in the free-standing 2D macroporous nanoelectronic networks. g, Photograph of a manually scrolled-up 3D macroporous nanoelectronic network. **h**, 3D reconstructed confocal fluorescence images of self-organized 3D macroporous nanoelectronic network viewed along the x-axis. Nonsymmetrical Cr/Pd/Cr metal layers (see *Experimental section*), which are stressed, were used to drive self-organization. The SU-8 ribbons were doped with Rodamine-6G for imaging.

Dark-field optical microscopy images obtained from a typical nanoelectronic mesh fabrication corresponding to the steps described above (**Fig. 2-4b**) highlight several important features. First, the images recorded after contact printing (**Fig. 2-4b, I**) confirm that nanowires are well-aligned over areas where nanowire devices are fabricated. We can achieve good nanowire alignment on length scales up to at least several centimeters as reported elsewhere[6-7, 14]. Second, a representative dark-field image of the patterned periodic nanowire regions (**Fig. 2-4b, II**) shows that this process removes nearly all of the nanowires outside of the desired features. Nanowires can be observed to extend outside of the periodic circular feature (i.e., an end is fixed at the feature) at some points; however, these are infrequent and do not affect subsequent steps defining the nanodevice interconnections. Third, images of the underlying SU-8 mesh (**Fig. 2-4b, III**) and final device network with SU-8 passivated metal contacts and interconnects (**Fig. 2-4b, IV**) highlight the regular array of addressable nanowire devices realized in our fabrication

process. Last, scanning electron microscopy (SEM) images (**Fig. 2-4c**) show that these device elements have on average 1-2 nanowires in parallel.

The 2D nanoelectronic mesh structures were converted to free-standing macroporous networks by dissolution of the sacrificial Ni layers over a period of 1-2 h (see Experimental section). Representative images of a free-standing nanoelectronic network (**Fig. 2-4d** and **Fig. 2-4e**) highlight the 3D and flexible characteristics of the structure and show how input/output (I/O) to the free-standing network can be fixed at one end outside of a solution measurement petri-dish chamber. Electrical characterization of individually-addressable nanowire device elements in a free-standing mesh demonstrates that the device-yield is typically ~90% (from 128 device design) for the free-standing nanoelectronic mesh structures fabricated in this way. The average conductance of the devices from a representative free-standing mesh (**Fig. 2-4f**), 2.85 ± 1.6 μS, is consistent with 1-2 nanowires/device based on measurements of similar (30 nm diameter, 2 μm channel length) *p*-type Si single nanowire devices[26], and thus also agrees with the structural data discussed above. In addition, by varying the printed nanowire density and S/D metal contact widths, it is possible to tune further the average number of nanowires per device element.

These 2D free-standing macroporous nanoelectronic networks were transformed to 3D structures using two general methods. First, 2D macroporous nanoelectronic networks were manually rolled-up into 3D arrays (**Fig. 2-4g**) with nanoelectronic elements in different layers of the resulting "scroll". Second, by introducing built-in stress in metal interconnects with a trilayer metal stack, the mesh can be designed to self-organize into a similar scrolled structure as achieved by manual rolling[13, 27]. A

reconstructed 3D confocal fluorescent image of a 3D nanoelectronic mesh array produced in this manner (Fig. 2*H*) shows clearly the 3D macroporous nanoelectronic network and can be used to estimate a free volume of (>99%). More generally, these self-organized 3D macroporous nanoelectronic structures could be readily diversified to meet goals for different hybrid materials using established mechanical design and bifurcation strategies[28].

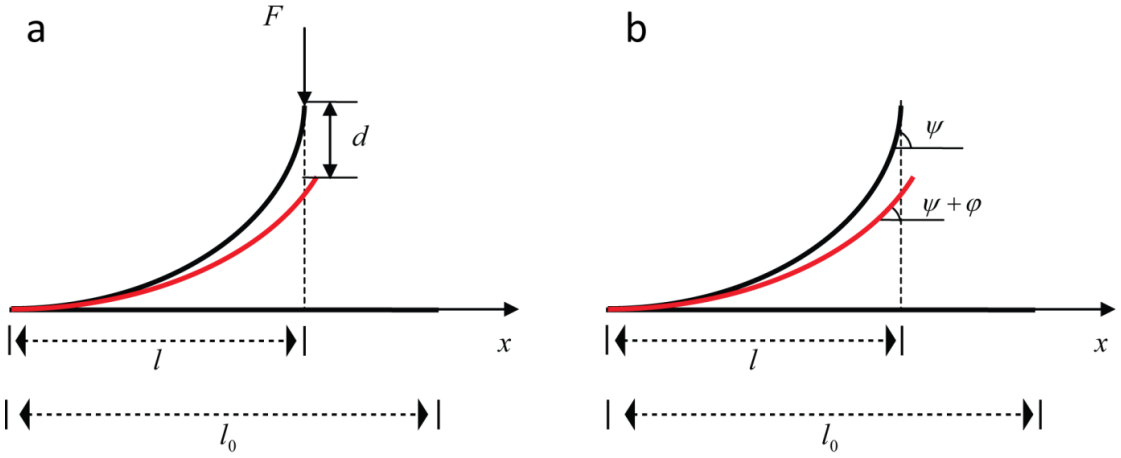

Figure 2-5 Schematics for bending stiffness calculation. **a**, A schematic of the position of the substrate free beam before (black) and after (red) applying a calibrated force, *F*, and vertical displacement, *d*, at the end of the beam with the AFM. **b**, The angle between the tangential direction of a material point on the beam and the horizontal direction, ψ, of the ribbon before (black) and after displacement, $\psi+\varphi$, (red). l_0: the total length of the ribbon. *l*: projection of the ribbon.

2.3.2 Mechanics analysis

The 3D macroporous nanoelectronic networks consist of single-layer polymer (SU-8) structural and three-layer ribbon (SU-8/metal/SU-8) interconnect elements. The effective bending stiffness per unit width of the 3D macroporous nanoelectronic networks can be estimated[29] by equation (1)

$$\overline{D} = \alpha_s D_s + \alpha_m D_m \quad (1)$$

where α_s and α_m are the area fraction of the single-layer polymer and three-layer interconnect ribbons in the networks. $D_s=E_sh^3/12$ is the bending stiffness per unit width of the single-layer polymer, where E_s = 2 GPa and h are the modulus and thickness of the SU-8. For a SU-8 ribbon with 500 nm thickness, D_s is 0.02 nN·m. D_m is the bending stiffness per unit width of a three-layer structure, which includes 500 nm lower and upper SU-8 layers and 100 to 130 nm metal layer, and was measured experimentally as described below and shown in **Figure 2-2**.

Qualitatively, the facile manipulation of the macroporous nanoelectronic networks to form 3D structures suggests a very low effective bending stiffness. We have evaluated the effective bending stiffness, $\overline{D}$, using a combination of calculations and experimental measurements. Due to the residual stress, the SU-8/metal/SU-8 elements bend upward from the substrate (due to internal stress of the asymmetric metal layers) with a constant curvature, K_0, and projected length, l, where l_0 is the free length defined by fabrication. We use the curvilinear coordinate, s, to describe the distance along the curved ribbon from the fixed end, and the coordinate, χ, to describe the projection position of each material point of the ribbon (**Fig. 2-5a**). For a specific material point with distance s, the projection position χ can be calculated as $x = \int \cos\psi ds$, where $\psi = K_0 s$ is the angle between the tangential direction of the curvilinear coordinate s and the horizontal direction (**Fig. 2-5b**). Integration yields $x = \sin(K_0 s)/K_0$ and when $\chi = l$ and $s = l_0$, K_0 = 0.0128 μm^{-1} for typical experimental parameters l_0 = 100 μm and l = 75 μm.

As the element is deflected a distance, *d*, by the AFM tip with a force, *F*, each material point is rotated by an angle, φ, (**Fig. 2-5b**), where the anti-clockwise direction is defined as positive. Assuming a linear constitutive relation between the moment M and curvature change $d\varphi/ds$[30] yields

$$\frac{d\varphi}{ds} = \frac{M}{wD_m} \tag{2}$$

where M is the moment as a function of position, x (**Fig. 2-5**), and *w* is the width.

$$M(x) = -F(l - x) \tag{3}$$

Solving for the bending stiffness, D_m, with the assumption that φ is small so that $\sin\varphi \approx \varphi$ yields:

$$D_m = \frac{F}{wd}\left(\frac{ll_0\sin(K_0l_0)}{K_0} + \frac{1}{{K_0}^2}\left(l\cos(K_0l_0) - l + \frac{l_0}{2}\right) + \frac{1}{{K_0}^3}\left(\frac{\sin(2K_0l_0)}{4} - \sin(K_0l_0)\right)\right) \tag{4}$$

The slope of a representative loading force-deflection curve, yields F/d=12 nN/μm (**Fig. 2-2c**), and using equation (4) the calculated bending stiffness per width (w= 5 μm) is D_m = 0.358 nN·m. For typical 3D macroporous nanoelectronic networks the area fraction for both types of elements (i.e., SU-8 and SU-8/metal/SU-8) can range from 1–10%, yielding values of the effective bending stiffness from 0.0038 to 0.0378 nN·m.

2.4 Conclusions

We have demonstrated a general strategy for preparing ordered 3D interconnected and addressable macroporous nanoelectronic networks from ordered 2D nanowire nanoelectronic "precursors", which are fabricated by conventional lithography. The 3D networks have porosities larger than 99%, contain 100's of addressable nanowire devices, and have feature sizes from the 10 micron scale for electrical and structural

interconnections to the 10 nanometer scale for the functional nanowire device elements. The network is extremely flexible with the bending stiffness from 0.0038 to 0.0378, which is the most flexible electronics reported.

2.5 Bibliography

1. Reuss, R. H., Hopper, D. G. & Park, J. G. *MRS Bull.* **31**, 447 (2006).

2. Tian, B. *et al. Nat. Mater.* **11**, 986 (2012).

3. Al-sarawi, S. F., Abbott, D. & Franzon, P. D. *IEEE Trans Components Pag & Manuf Technol.* **21**, 2 (1998).

4. Benkart P, *et al. IEEE Des Test Comput.* **22**, 512 (2005).

5. Ahn, J. H. *et al. Science* **314**, 1754 (2006).

6. Javey, A., Nam, S., Friedman, R. S., Yan, H. & Lieber, C. M. *Nano Lett.* **7**, 773 (2007).

7. Nam, S., Jiang, X., Xiong, Q., Ham, D. & Lieber, C. M. *Proc. Natl. Acad. Sci. USA* **106**, 21035 (2009).

8. Wu, Y. *et al. Nano Lett.* **4**, 433 (2004).

9. Butt, H. J. & Jaschke, M. *Nanotechnology* **6**, 1 (1995).

10. Tian, B. *et al. Science* **329**, 831 (2010).

11. Yang, C., Zhong, Z. H. & Lieber, C. M. *Science* **310**, 1304 (2005).

12. Tian, B. Z., Xie, P., Kempa, T. J., Bell, D. C. & Lieber, C. M. *Nat. Nanotechnol.* **4**, 824 (2009).

13. Tian, B. *et al. Science* **329**, 831 (2010).

14. Fan, Z. *et al. Nano Lett.* **8**, 20 (2008).

15. Lu, W. & Lieber, C. M. *Nat. Mater.* **6**, 841 (2007).

16. Lieber, C. M. & Wang, Z. L. *MRS Bull.* **32**, 99 (2007).

17. Qian, F., Gradecak, S., Li, Y., Wen, Y. & Lieber, C. M. *Nano Lett.* **5**, 2287 (2005).

18. Tian, B. *et al. Nature* **449**, 885 (2007).

19. Gao, R. *et al. Nano Lett.* **12,** 3329 (2012).

20. Jiang X *et al. Proc. Natl. Acad. Sci. USA* **108**, 12212 (2011).

21. Yan, H. *et al. Nature* **470**, 240 (2011).

22. Xiang, J. *et al. Nature* **441**, 489 (2006).

23. Cui, Y., Wei, Q., Park, H. & Lieber, C. M. *Science* **293**, 1289 (2001).

24. Qin, Y., Wang, X. D, & Wang, Z. L. *Nature* **451**, 809 (2008).

25. Chan, C. K. *et al. Nat. Nanotechnol.* **3**, 31 (2008).

26. Zheng, G. F., Patolsky, F., Cui, Y., Wang, W. U. & Lieber, C. M. *Nat. Biotechnol.* **23**, 1294 (2005).

27. Leong, T. G. *et al. Proc. Natl. Acad. Sci. U.S.A.* **106**, 703 (2009)

28. Freund, L. B. *J. Mech. Phys. Solids* **48**, 1159 (2000).

29. Kim, D. H. *et al. Science* **333**, 838 (2011).

30. Landau, L. D. & Lifshitz, E. M. *Theory of Elasticity, 3rd edition, p67-73.* (Elsevier, 1986).

Chapter 3. Integration of three-dimensional macroporous nanoelectronics with materials

3.1 Introduction

Seamless integration of electronics with host materials could transfer inactive materials into active materials, which allow the communication between the materials and external environment, and implement multifunction from nanoelectronics into host materials to create a smart system[1-2]. Traditional electronics are planar and rigid, however, most materials and systems in our daily life are three-dimensional (3D) and non-planar. To overcome this issue, flexible electronics have been developed to cover on the surface of other systems to implement the functions into host materials[3-5]. However, those surface electronics are still not able to detect the property change through the whole materials in 3D and provide a full range of control. People can implant the rigid probe into those materials. However, those methods are invasive. The mechanical mismatch between those probes and materials cause further break during the implementation[6-8]. Herein, we introduce a general strategy to 3D integration of electronics described in Chapter 2 with host materials and also show how these electronic networks in the host materials can be used to map chemical and mechanical changes induced by the external environment in 3D.

3.2 Experimental

3.2.1 3D macroporous photodetectors and device localization in 3D

Confocal laser scanning microscopy (Fluoview FV1000, Olympus America Inc., PA) was used to characterize the 3D macroporous nanoelectronic network. Conventional 405 nm and 473 nm wavelength lasers, where 405 nm was used to produce photocurrents in the nanowire transistor devices, and the 473 nm was used for fluorescence imaging. The SU-8 structure was doped with Rodamine 6G for fluorescence imaging. The macroporous nanoelectronic network was immersed into dioniozed (DI) water, individual devices were biased with 100 mV, and 40X or 100X water immersion objectives were used for imaging. The photocurrent signal was amplified (SIM 918, Stanford Research System, MA) bandpass filtered, (1-6000 Hz, home-built system), and synchronized with laser scanning position using an analog signal input box (F10ANALOG, Olympus America Inc., PA). The conductance signal from the resulting images was read out by *imageJ*, and the data were analyzed and fitted by *OriginPro*.

3.2.2 3D macroporous chemical sensors

Agarose (Sigma) was dissolved into DI water and made as 0.5%, and heated up to 100 ^{o}C. The gel was drop casting onto the device and cooled down to room temperature. 4',6-diamidino-2-phenylindole (DAPI, Sigma) was used to dope the gel for the confocal 3D reconstructed imaging. A PDMS fluidic chamber with input/output tubing and Ag/AgCl electrodes was sealed with the silicon substrate and the device or device-gel hybrid using silicone elastomer glue (Kwik-Sil, World Precision Instruments, Inc). Fresh medium was delivered to the device region through both inner and outer tubing. The solution pH was stepwise varied inside the channel by flowing (20 mL/h) 1x phosphate

buffered solutions with fixed pH values from pH 6-8. The recorded device signals were filtered with a bandpass filter of 0-300 Hz.

3.2.3 3D macroporous strain sensors in elastomer

A freestanding 2D macroporous nanoelectronic network was suspended in water, and placed on a thin (200 – 500 μm) piece of cured silicone elastomer sheet (Sylgard 184, Dow Corning). The hybrid macroporous nanowire network/silicon elastomer was rolled into a cylinder, infiltrated with uncured silicone elastomer under vacuum, and cured at 70 °C for 4 hours. The resulting hybrid nanoelectronic/elastomer cylinders had volumes of ca. 300 mm^3 with volume ratio of device/elastomer of < 0.1%. The structure of the macroporous electronics/elastomer hybrid was determined using a HMXST X-ray micro-CT system with a standard horizontal imaging axis cabinet (model: HMXST225, Nikon Metrology, Inc., Brighton, MI). In a typical imaging experiment, the acceleration voltage was 60-70 kV, the electron beam current was 130-150 mA, and no filter was used. *BGStudio* MAX (ver. 2.0, Volume Graphics GMbh, Germany) was used for 3D reconstruction and analysis of the micro-CT images, which resolve the 3D metal interconnect structure and nanowire S/D contacts; the Si nanowires were not resolved in these images but were localized at the scale of the S/D contacts. The piezoelectric response to strain of the nanowire devices was calibrated using a mechanical clamp device under tensile strain, where the strain was calculated from the length change of the cylindrical hybrid structure. The bending strain field was determined in experiments where the cylindrical hybrid structure, with calibrated nanowire strain sensors, was subject to random bending deflections.

3.3 Results and discussion

The 3D macroporous nanoelectronics developed were used to seamlessly merged with host materials samples using a solution (or liquid) casting process at or near room-temperature (**Fig. 3-1**). As examples, the hybrid nanoelectronic/gel material can be prepared by casting the agarose around a rolled-up macroporous nanoelectronic network. The hybrid nanoelectronic/PDMS can be prepared by using a freestanding 2D macroporous nanoelectronic network. The macroporous nanoelectronic network was suspended in water, and placed on a thin (200 – 500 μm) piece of cured silicone elastomer sheet. The hybrid macroporous nanowire network/silicon elastomer was rolled into a cylinder, infiltrated with uncured silicone elastomer under vacuum, and cured at 70 °C. Through those methods, the macroporous nanoelectronics can be integrated into the soft materials with nanoelectronic unit distributed and patterned in 3D inner space of the hybrid materials.

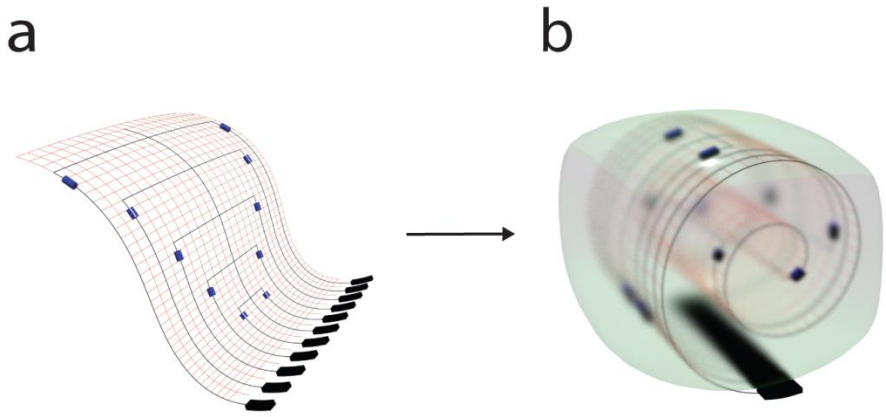

Figure 3-1 Strategy for integration of 3D macroporous nanoelectronics with host materials. **a**, Free-standing 2D macroporous nanowire nanoelectronic "precursor". Blue: nanoelectronic element, orange: passivation polymer, black: metal contact and input/output (I/O). **b**, 3D macroporous nanoelectronic networks integrated with host materials (Gray).

The semiconductor nanowire elements can display multiple sensory functionalities, including photon[9], chemical, biochemical, and potentiometric[10-11] as well as strain [12-13] detection, which make them particularly attractive for preparing hybrid active materials as described below. We have first characterized photoconductivity changes (i.e., photon detection) of nanowire elements while imaging the nanoelectronic networks with a confocal microscope by recording conductance as a function of x-y-z coordinates and overlapping with simultaneously acquired fluorescence images (see Experimental Section; **Figs. 3-2** and **3-3**). As the focused laser is scanned across a sample (**Fig. 3-2a, I**) an increase of conductance due to the photocurrent[14] in nanowire is recorded at the positions of the nanowire devices. The resolution of this approach can be assessed in two ways. Conventionally, the plot of conductance versus position (**Fig. 3-2a, II**) can be fit with a Gaussian function and its full-width at half-maximum (FWHM) reflects the diffraction limited resolution of the illuminating light spot. Second and recognizing that the nanowire diameter (30 nm) is line-like; we can use methods similar to super-resolution imaging technologies[15-16] to locate the nanowire to much higher precision by identifying the peak position from the Gaussian fit. We note that a similar concept as exploited in stochastic super-resolution imaging to resolve close points can be implemented in our photoconductivity maps because individual devices can be turned on and off as needed[15].

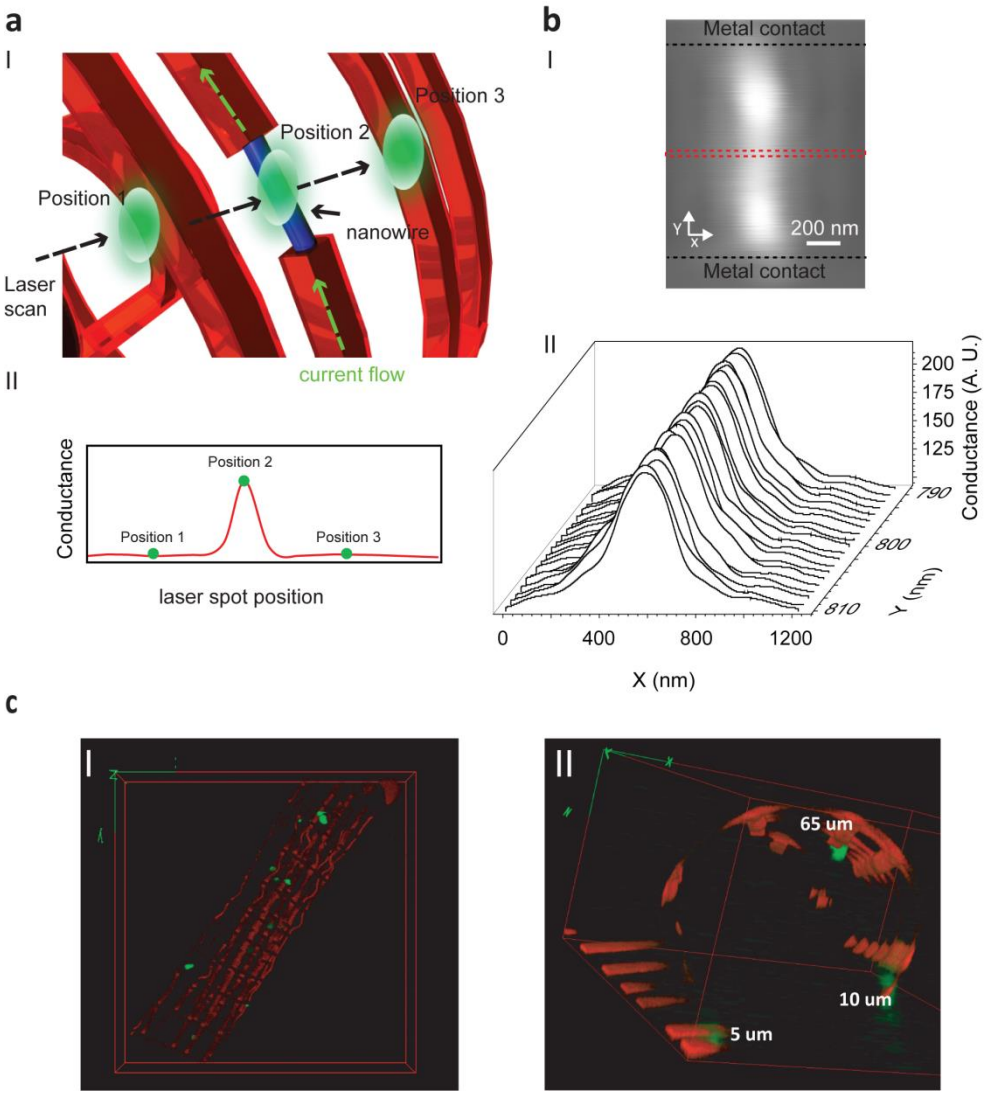

Figure 3-2 3D macroporous photodetectors and device localization. **a**, Schematics of the single 3D macroporous nanowire photodetector characterization. The green ellipse: laser spot, blue cylinder: nanowire and orange: SU-8 mesh network. The illumination of the laser spot generated from confocal microscope on the nanowire device (**I**) makes the conductance change of nanowire, which could be (**II**) correlated with laser spot position. Green spots in (**II**) correlate to the laser spot positions in (**I**). **b**, High-resolution (1 nm per pixel) photocurrent image (**I**) from single nanowire device (2 μm channel length) on substrate recorded with focused laser spot scanned in x-y plane. The black dash lines indicate the boundary of metal contact in the device.(**II**) 20 times photocurrent measurements from the central region (red dash box) of the nanowire device with high resolution (the distance for each trace in x-direction is 1 nm). **c**, 3D reconstructed photocurrent imaging overlapped with confocal microscopy imaging shows the spatial correlation between nanowire photodetectors with SU-8 framework in 3D. Green: false color of the photocurrent signal, orange (rhodamine 6G): SU-8 mesh network. Dimensions in (**I**), x: 317 μm; y: 317 μm; z: 53 μm; in (**II**), x: 127 μm; y: 127 μm; z: 65 μm. The white numbers in (**II**) indicate the heights of the nanowire photodetectors.

A typical high-resolution photoconductivity image of a single nanowire device (**Fig. 3-2b, I**) shows clearly the position of the nanowire. The conductance change versus x-position is perpendicular to the nanowire axis (**Figs. 3-2b, II** and **3-3b**) yielded a FWHM is 314 ± 32 nm (n = 20) resolution consistent with confocal microscopy imaging resolution (202 nm) in this experiment. Moreover, the nanowire position determined from the peaks of Gaussian fits (**Fig. 3-3c**) yielded a standard deviation of 14 nm (n = 20), and shows that the position of devices can be localized with a precision better than the diffraction limit. In addition, we have acquired simultaneous photoconductivity and fluorescence confocal microscopy images to map the positions of nanowire devices in 3D macroporous nanoelectronic networks. Reconstructed 3D images (**Fig. 3-3c**) show that the 12 active nanowire devices can be readily mapped with respect to x-y-z coordinated in the 'rolled-up' macroporous nanoelectronic network structure. Given the complexity possible in 3D nanoelectric/host hybrid materials, this approach provides straightforward methodology for determining at high-resolution the positions of the active nanoelectronic sensory elements with respect to structures within the host. In the future, we also note that the resolution could be even further improved by incorporating point-like transistor photoconductivity detectors[10, 17], *p*-*n* photodiodes[18] and *p*-*i*-*n* avalanche photodiodes[19] nanowire building blocks within the 3D macroporous nanoelectronic network.

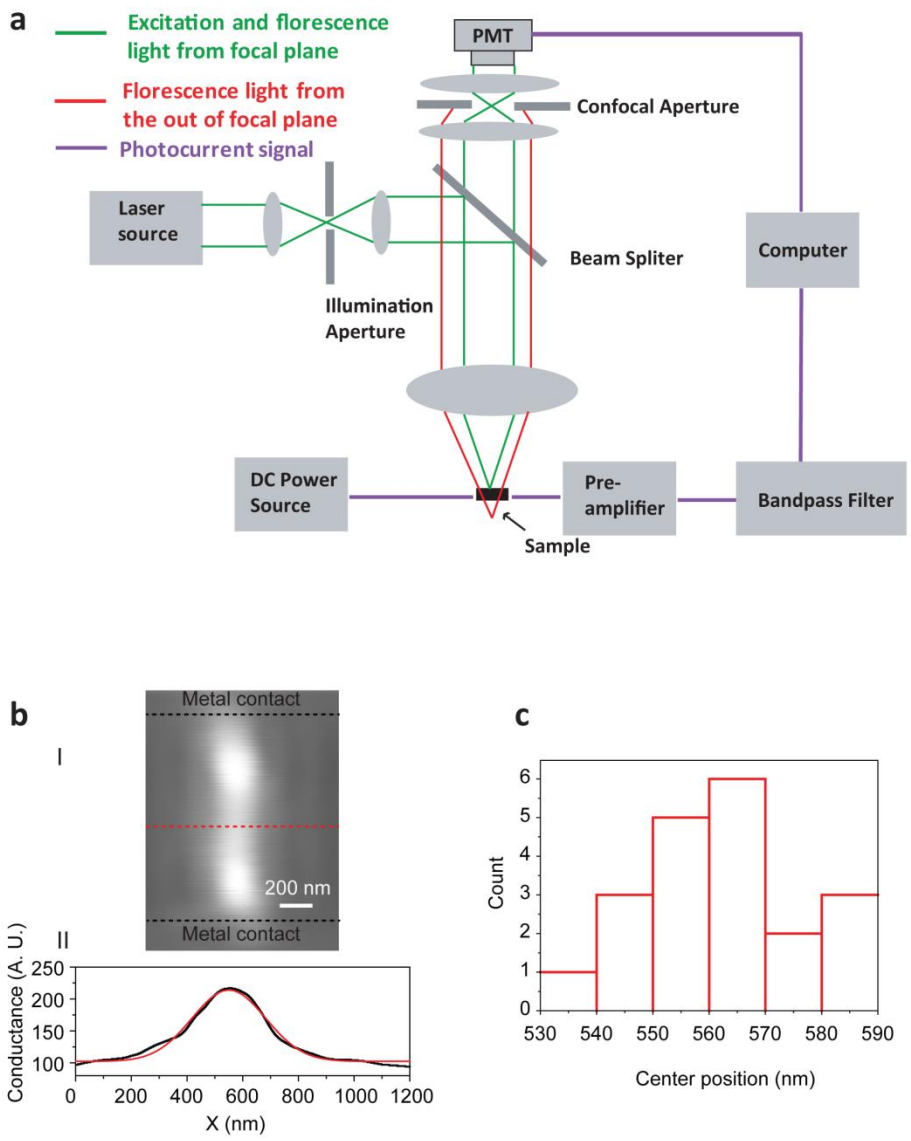

Figure 3-3 Localization of 3D macroporous nanoelectronic devices. 3D macroporous nanoelectronic FET devices exhibit photoconductivity[20] that was used to determine spatial positions using a confocal microscope equipped with an analog signal input box. **a**, Schematic of photocurrent detection and correlation with confocal microscopy laser spot scanning position. A 405 nm laser wavelength, 100X water immersion lens, and 0.1 mV source/drain device bias-voltage were used in the experiments. **b**, High-resolution (1 nm per pixel) photocurrent image (**I**) from a single nanowire device (2 μm channel length between upper/lower metal contacts) recorded scanning in x-y plane. The red dash line indicates the direction perpendicular to the nanowire axis. The black dash lines indicate the boundaries of metal contacts. (**II**) Photocurrent measured along the red dash line in (**I**). Experimental data are fit with a Gaussian distribution (red solid curve). **c**, Distribution of the center point positions determined from the 20 independent scans in region of indicated in **Figure 3-2b** and about the single scan line shown in (**b**, **I**).

Second, we have used macroporous nanowire nanoelectronic networks to map pH changes in 3D through agarose gel using a macroporous nanoelectronic/gel hybrid, and for comparison, in aqueous solution using a free-standing 3D nanoelectronic sensory network. The hybrid nanoelectronic/gel material was prepared by casting the agarose around a rolled-up macroporous nanoelectronic network, where the gel and SU-8 mesh of the nanoelectronic network were doped with 4',6-diamidino-2-phenylindole (DAPI) and Rodamine 6G, respectively (see Experimetal Section). A reconstructed 3D confocal microscopy image of the hybrid material (**Fig. 3-4a**) shows clearly the 3D device mesh fully embedded within an agarose gel block without phase separation. To carry out sensing experiments either the 3D nanoelectronic/gel hybrid material or a 3D nanoelectronic mesh was contained within a microfluidic chamber (**Fig. 3-4b**). Positions of nanowire transistor devices, which can function as very sensitive chemical/biological detectors[10, 11, 21], were determined by the photocurrent mapping method described above. For both 3D nanoelectronic mesh and nanoelectronic/gel hybrid we recorded signals simultaneously from 4 devices chosen to span positions from upper to lower boundary of mesh or gel, where representative z-coordinates of the devices positions within the hybrid sample are highlighted in **Figure 3-4c**; a similar z-range of devices for the free nanoelectronic mesh was also used.

Representative data recorded from p-type nanowire FET devices in 3D mesh network without gel (**Fig. 3-4d, I**) and in the hybrid 3D nanoelectronic mesh/agarose gel hybrid (**Fig. 3-4d, II**) highlight several important points. First, the device within the 3D macroporous network without gel showed fast stepwise conductance changes (<1 s) with solution pH changes. The typical sensitivity of these devices was ca. 40 mV/ pH, and is

consistent with values reported for similar nanowire devices[22]. Second, the device within the 3D nanoelectronic mesh/gel hybrid exhibited substantially slower transition times with corresponding changes of the solution pH; that is, signal change required on order of 2000 s to reach steady-state, and thus was 1000-fold slower than in free solution. Third, the device within the 3D nanoelectronic mesh/gel hybrid exhibited lower pH sensitivity in terms of mV/pH; that is, 20 - 40 mV/pH for device in gel compared to 40 - 50 mV/pH for device in free solution.

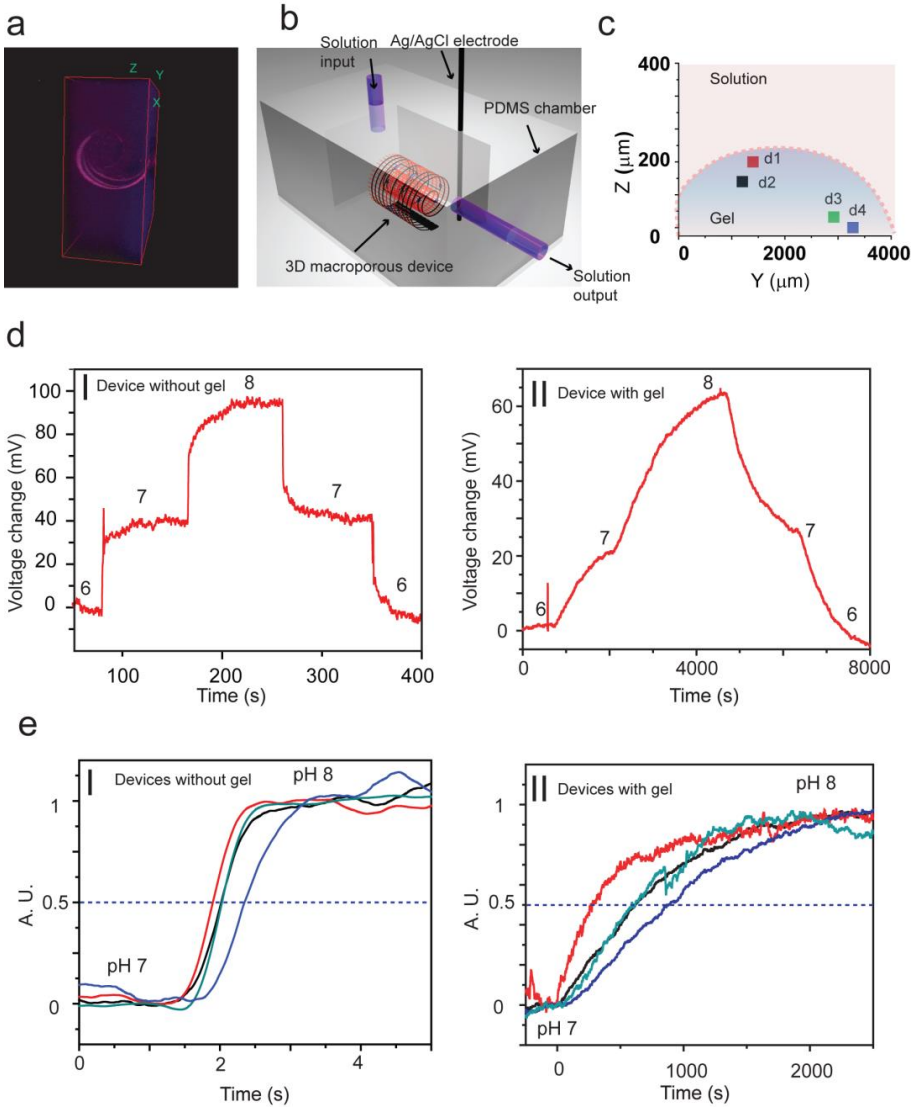

Figure 3-4 3D macroporous chemical sensors. **a**, x-z views of 3D reconstructed image of the 3D macroporous nanoelectronic network in gel. Red (rhodamine 6G): SU-8 mesh network and blue (DAPI): agrose gel. Dimensions: x = 317 μm; y = 317 μm; and z = 144 μm. **b**, Schematics of the experimental set-up. **c**, The projection of four nanowire devices in the y-z plane. Red dashed line corresponds to the approximate gel boundary, and the red and blue areas correspond to aqueous solution and agrose gel, respectively. **d**, Representative change in calibrated voltage over time with pH change for 3D macroporous nanowire chemical sensors in solution (**I**) and embedded in agrose gel (**II**). **e**, Calibrated voltage with one pH value change in solution for 4 different devices located in 3D space. (**I**) 4 devices without gel and (**II**) 4 devices embedded in agrose gel.

Direct comparison of the temporal responses of four devices at different 3D positions in the two types of samples (**Fig. 3-4e**) provides additional insight into the pH

changes. The time to achieve one-half pH unit change for the four different devices in 3D macroporous network without gel (**Fig. 3-4e, I**) is ca. 0.5 s and the difference between devices is only ca. 0.01 s. We note that the time delay in the data recorded from device d4 is consistent with the down-stream position of this device within the fluidic channel. In contrast, the time to achieve one-half for the four devices in the 3D nanoelectronic mesh/gel hybrid (**Fig. 3-4e, II**) range from ca. 280 to 890 s for devices d1 to d4, respectively, where devices positions are shown in Fig. 4*C*. The results show that the device response time within the agarose is ca. 500 – 1700 times slower than in solution and is proportional to the distance from the solution/gel boundary, although the detailed variation suggests heterogeneity in the diffusion within the agarose gel. Significantly, the ability to map the diffusion of molecular and biomolecular species in 3D hybrid systems using the macroporous nanoelectronic sensory networks offers opportunities for self-monitoring of gel, polymers and tissue systems relevant to many areas of science and technology[23, 24].

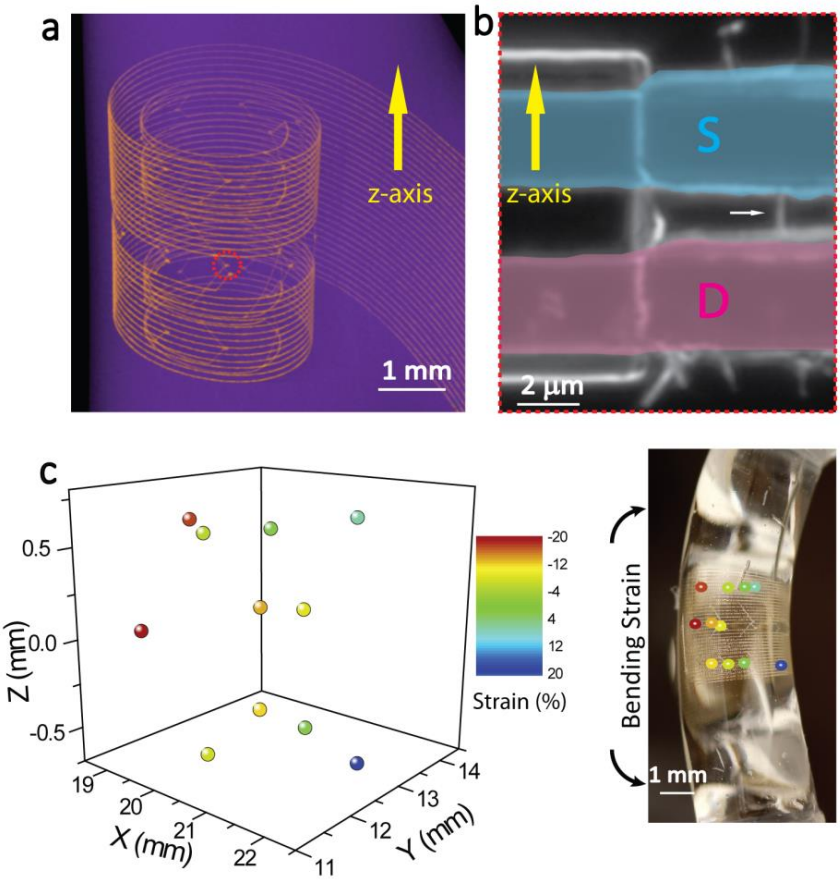

Figure 3-5 3D macroporous strain sensors embedded in elastomer. **a**, µ-CT 3D reconstruction of the macroporous strain sensor array embedded in a piece of elastomer. Pseudo-colors are applied: orange: metal, purple: elastomer. **b**, Dark field microscopy image of a typical nanowire device indicated by red dash circle in (**a**). All the functional nanowires are intentionally aligned parallel to the axial axis of the elastomer cylinder. The white arrow points a nanowire. **c**, A bending strain field was applied to the elastomer piece. The 3D strain field was mapped by the nanowire strain sensors using the sensitivity calibration of the nanowire devices. The detected strains are labeled in the cylinder image at the device positions.

Third, we have used embedded 3D macroporous nanoelectronic networks to map strain distributions in elastomeric silicone host materials. Previous studies have shown that Si nanowires have a high piezoresistance response[12], making them good candidates for strain sensors[13]. To explore the potential of Si nanowire device arrays to map strain within materials, we have prepared and characterized 3D macroporous nanoelectronic network/elastomer hybrid materials (see Experimental Section). The resulting hybrid

macroporous nanoelectronic network/elastomer cylinders had volumes of ca. 300 mm^3 with volume ratio of device/elastomer of < 0.1%. X-ray micro-computed tomography (μCT) studies of the nanoelectronic network/elastomer cylinders (**Fig. 3-5a**) were used to determine the 3D metal interconnects and locations of nanowire devices within the cylindrical hybrid structures (see Materials Experimental Section). The alignment of nanowire elements along the cylinder axis was confirmed by dark-field optical microscopy images (**Fig. 3-5b**), which show the nanowires lying along the cylinder (z) axis.

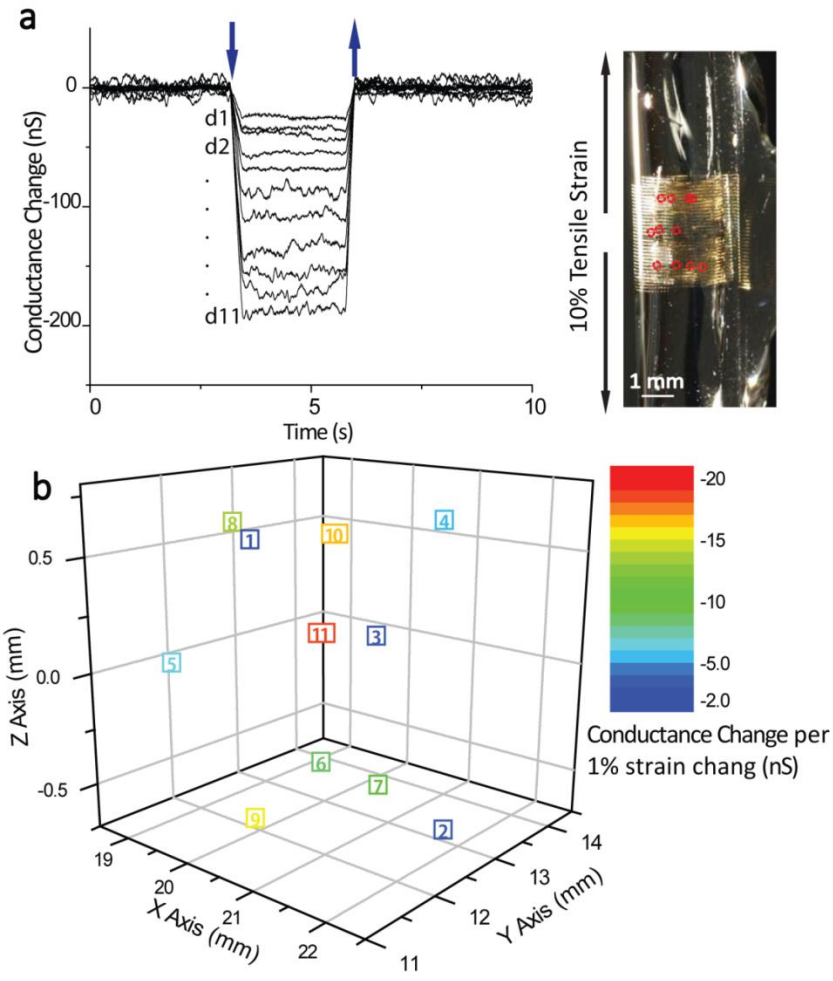

Figure 3-6 Calibration of the 3D macroporous nanoelectronic strain sensors. **a**, Conductance change versus time as a 10% tensile strain was applied to hybrid 3D macroporous nanoelectronic networks/PDMS cylindrical sample. The downward and

(Continued) upward pointing arrows denote the times when the strain was applied and released, respectively. The direction of strain on the cylindrical hybrid sample and projected position of the macroporous nanoelectronic networks are indicated in the right optical micrograph. The conductance changes of 11 measured nanowire devices (labeled arbitrarily in terms of increasing sensitivity) were recorded and used for the conductance change per strain calibration. **b**, Strain sensitivity calibration of the nanowire devices is plotted in 3D. The data points are color coded by the sensitivity of the devices (**a**).

The good axial alignment of the nanowire devices was exploited to calibrate the strain sensitivity of each of elements with the 3D hybrid structure allows straightforward calibration of the device sensitivity in pure tensile strain field. Application of a 10% tensile strain along the cylinder axis (**Fig. 3-6a**) yielded decreases in conductance up to 200 nS for the individual devices, d1 – d11. Because the conductance immediately returned to baseline when strain was released and under compressive loads the conductance change had the opposite sign, we can conclude that these changes do reflect strain transferred to the nanowire sensors. From the specific response of the devices within the hybrid structure we calculate and assign a calibrated conductance change/1% strain value for each of the eleven sensor elements (**Fig. 3-6b**), and use this for analysis of different applied strains. For example, we applied a bending strain to the cylinder and from the recorded conductance changes and calibration values were able to map readily the 3D strain field as shown in **Figure 3-5c**. We note that the one-dimensional geometry of nanowires gives these strain sensors nearly perfect directional selectivity, and thus, by developing macroporous nanoelectronic network with nanowires device aligned parallel and perpendicular to the cylinder axis enable mapping all three components of the strain field in the future.

3.4 Conclusion

The macroporous nanoelectronic networks were merged with organic gels and polymers to form hybrid materials in which the basic physical and chemical properties of the host were not substantially altered, and electrical measurements further show > 90% yield of active devices in the hybrid materials. We further demonstrated a new approach to determine the positions of the nanowire devices within 3D hybrid materials with ca. 14 nm resolution that involves simultaneous nanowire device photocurrent/confocal microscopy imaging measurements. This method also could have substantial impact on localizing device positions in macroporous nanoelectronic/biological samples, where it provides the capability of determining positions of sensory devices at the subcellular level. In addition, we explored functional properties of these hybrid materials. First, we showed that it was possible to map time-dependent pH changes throughout a nanowire network/agarose gel sample during external solution pH changes. These results suggest substantial promise of the 3D macroporous nanoelectronic networks for real-time mapping of diffusion of chemical and biological species through polymeric samples as well as biological materials such as synthetic tissue[24-25]. Second we demonstrated that Si nanowire elements can function as well-defined strain sensors, and thereby characterize the strain field in a hybrid nanoelectronic elastomer structures subject to uniaxial and bending forces. More generally, we believe our approach to fabrication of multi-functional 3D electronics and integration with host materials suggests substantial promise for (1) general fabrication of truly 3D integrated circuits based on conventional fabrication processes via assembly from a 2D "precursor", (2) seamless 3D incorporation of multi-functional nanoelectronics into living and nonliving systems leading to make "very smart" material systems and a completely new level of "cyborg" tissues.

3.5 Bibliography

1. Reuss, R. H., Hopper, D. G. & Park, J. G. *MRS Bull.* **31**, 447 (2006).

2. Thakor, N. V. *Sci. Transl. Med.* **5**, 210ps17 (2013).

3. Kim, D. H. *et al. Science* **33**, 838 (2011).

4. Lu, N. & Kim, D. H. *Soft Robotics* **1**, 53 (2013).

5. Kim, D. H. *et al. Nat. Mater.* **9**, 511 (2010).

6. G Wise, K. D. *IEEE Eng. Med. Biol. Magazine* **24**, 22 (2005).

7. Normann, R. A. *Nat. Clin. Pract. Neuro.* **3**, 444 (2007).

8. Seymour, J. P. & Kipke, *D. R. Biomaterials* **28**, 3594 (2007).

9. Fan, Z., Ho, J. C., Jacobson, Z. A., Razavi, H. & Javey, A. *Proc. Natl. Acad. Sci. USA* **105**, 11066 (2008).

10. Cui, Y., Wei, Q., Park, H. & Lieber, C. M. *Science* **293**, 1289 (2001).

11. Zheng, G. F., Patolsky, F., Cui, Y., Wang, W. U. & Lieber, C. M. *Nat. Biotechnol.* **23**, 1294 (2005).

12. He, R. & Yang, P. *Nat. Nanotechnol.* **1**, 42 (2006).

13. Lee, C. H., Kim, D. R. & Zheng, X. *Proc Natl Acad Sci USA* **107**, 9950 (2009).

14. Tsen, A. W., Donev, L. A. K., Kurt, H., Herman, L. H. & Park, J. *Nat. Nanotechnol.* **4**, 108 (2009).

15. Huang, B., Wang, W. Q., Bates, M. & Zhuang, X. W. *Science* **319**, 810 (2008).

16. Toprak. E., Balci, H., Blehm, B. H. & Selvin, P. R. *Nano Lett.* **7**, 2043 (2007).

17. Cohen-Karni T et al. *Nano Lett.* **12**, 2639 (2012).

18. Jiang, Z., Qing, Q., Xie, P., Gao, R. & Lieber, C. M. *Nano Lett.* **12**, 1711 (2012).

19. Hayden, O., Agarwal, R. & Lieber, C. M. *Nat. Mater.* **5**, 352 (2006).

20. Ahn, Y., Dunning, J. & Park, J. *Nano Lett.* **5**, 1367 (2005).

21. Patolsky, F., Timko, B. P., Zheng, G. & Lieber, C. M. *MRS Bullet.* **32**, 142 (2007).

22. Tian, B. *et al. Science* **329**, 831 (2010).

23. Griffith, L. G. & Swartz, M. A. *Nat. Rev. Mol. Cell. Biol.* **7**, 211 (2006).

24. Sanger, F. *Proc. Natl. Acad. Sci. USA* **74**, 5463 (1977).

25. Glicklis, R., Merchuk, J. C. & Cohen, S. *Biotechnol. Bioeng*. **86**, 672 (2004).

Chapter 4. Three-dimensional macroporous nanoelectronics scaffold for synthetic tissue

4.1 Introduction

The design and functionalization of porous materials has been actively pursued to enable new material properties and applications[1-3]. In particular, the development of synthetic 3D macroporous biomaterials as extracellular matrices (ECMs) represents a key area because (1) functionalized 3D biomaterials allow for studies of cell/tissue development in the presence of spatiotemporal biochemical stimulants[3-6], and (2) the understanding of pharmacological response of cells within synthetic tissues is expected to provide a more robust link to *in-vivo* disease treatment than that from 2D cell cultures[6-8]. Advancing further such biomaterials requires capabilities for monitoring cells throughout the 3D microenvironment[6]. While electrical sensors are attractive tools, it has not been possible to integrate such elements with porous 3D scaffolds for localized real-time monitoring of cellular activities and physicochemical change, although such capability could lead to new lab-on-a-chip pharmacological platforms[9,10] and hybrid 3D electronics-tissue materials for synthetic biology[11,12].

Recently, there have been several reports describing the coupling of electronics and tissues using flexible and/or stretchable planar devices[13-17] that conform to natural tissue surfaces. These planar devices have been used to probe electrical activities near surfaces of the heart[13-15], brain[16] and skin[17]. To date, seamless 3D integration of electronics with biomaterials and synthetic tissues has not been achieved. Key points that

must be addressed to achieve this goal include: (1) the electronic structures must be macroporous, not planar, to enable 3D interpenetration with biomaterials; (2) the electronic network should have nanometer to micrometer scale features comparable to biomaterial scaffolds; and (3) the electronic network must have 3D interconnectivity and mechanical properties similar to biomaterials.

Here we introduce a conceptually new approach that meets this challenge by integrating nanoelectronics throughout biomaterials and synthetic tissues in 3D using macroporous nanoelectronic scaffolds as we introduced in Chapter 2. We use silicon nanowire field effect transistor (FET)-based nanoelectronic biomaterials, given their capability for recording both extracellular and intracellular signals with subcellular resolution[18-21]. FET detectors respond to variations in potential at the surface of the transistor channel region, and they are typically called active detectors[21]. Metal-electrode[22, 23] or carbon nanotube/nanofiber[24, 25] based passive detectors are not considered in our work because impedance limitations (i.e., signal/noise and temporal resolution degrade as the area of the metal or carbon electrodes is decreased) make it difficult to reduce the size of individual electrodes to the subcellular level[21-23], a size regime necessary to achieve noninvasive 3D interface of electronics with cells in tissue.

Our approach (**Fig. 4-1**) involved stepwise incorporation of biomimetic and biological elements into nanoelectronic networks across nanometer to centimeter size scales. First, chemically synthesized kinked[18] or uniform silicon nanowires were deposited either randomly or in regular patterns for single nanowire FETs -- the nanoelectronic sensor elements of the hybrid biomaterials (**Step A, Fig. 4-1**). Second, individual nanowire FET devices were lithographically patterned and integrated into free-

standing macroporous scaffolds (**Step B, Fig. 4-1**), the nanoES. The nanoES were designed to mimic ECM structures, and specifically, to be 3D, to have nanometer to micrometer features with high (>99 %) porosity, and to be highly flexible and biocompatible. NanoES were then combined with synthetic or natural macroporous ECMs providing (1) ECMs with electrical sensory function and (2) nanoES with biochemical environments suitable for tissue culture. Finally, cells were cultured within the nanoES (**Step C, Fig. 4-1**) to yield 3D hybrid nanoelectronics-tissue constructs. The emphasis on a nanoscale and biomimetic bottom-up pathway allows minimally invasive integration of electronic devices with cells and ECM components at the subcellular level in 3D. The nanoES are distinct from conventional 2D multi-electrode arrays (MEA) [23], carbon nanotube/nanofiber arrays[24, 25], implantable microelectrodes[23] and flexible or stretchable electrodes[13-17] in that the sensors are nanoscale semiconductors, and critically, that the sensor network is flexible, macroporous and 3D. As a result, nanoES are suitable for 3D cell cultures that are known to resemble the structure, function, or physiology of living tissues.

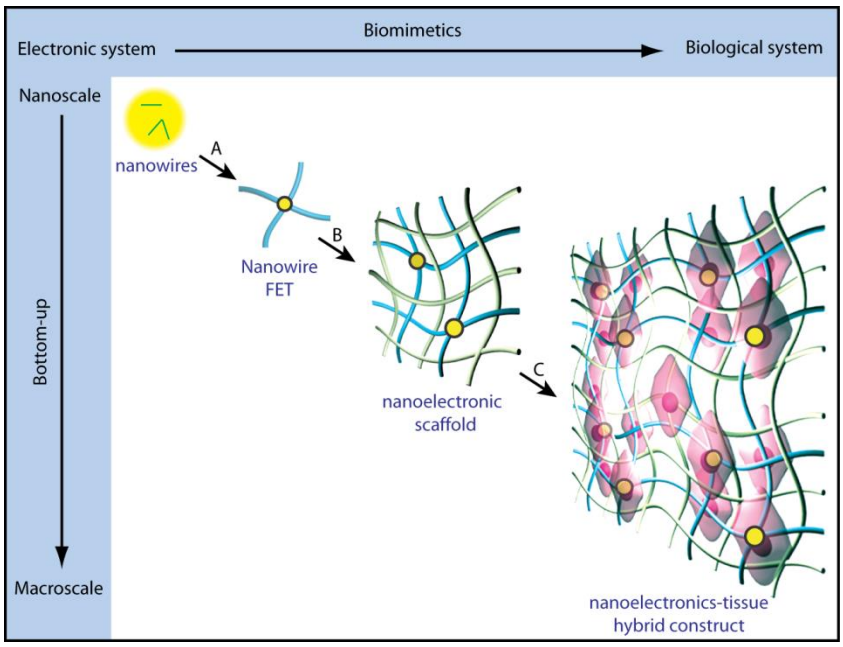

Figure 4-1 Integrating nanoelectronics with cells and tissue. Conventional bulk electronics are distinct from biological systems in composition, structural hierarchy, mechanics and function. Their electrical coupling at the tissue/organ level is usually limited to the tissue surface, where only boundary or global information can be gleaned unless invasive approaches are used. We have introduced a new concept by creating an integrated system from the discrete electronic and biological building blocks (e.g., semiconductor nanowires, molecular precursors of polymers and single cells). Three biomimetic and bottom-up steps have been designed: **a**, patterning, metallization and epoxy passivation for single nanowire FETs. **b**, forming 3D nanowire FET matrices (nanoelectric scaffolds) by self- or manual organization and hybridization with traditional extracellular matrices, and **c**, incorporation of cells and growth of synthetic tissue via biological processes. Yellow dots: nanowire components, blue ribbons: metal and epoxy interconnects, green ribbons: traditional extracellular matrices, pink: cells.

4.2 Experimental

4.2.1 Device fabrication and characterization

Nanowire synthesis and device fabrication are referred to Chapter 2. In brief, a layer of negative resist (SU-8) was coated on a nickel sacrificial layer, a solution with kinked or straight nanowires was deposited onto the SU-8 layer and allowed to evaporate, and then SU-8 was patterned by lithography to immobilize nanowires and to provide the basic framework for nanoES. Extra nanowires were washed away during the

development process of the SU-8 structure. Metal contacts were patterned by lithography and deposition. Finally, a layer of SU-8 was deposited and lithographically defined as the upper passivation layer on the interconnects.

4.2.2 NanoES/tissue scaffold

4.2.2.1 NanoES/collagen (Matrigel^{TM}) hybrid matrix

Prior to gel casting, collagen type-I (Sigma-Aldrich Corp., St. Louis, MO) was diluted (1:2 ~ 1:5) with culture media or phosphate buffered saline solution (PBS) and the pH was adjusted to ~ 7.4. Matrigel^{TM} (BD Bioscience, Bedford, MA) was used as received or diluted (1:2 ~ 1:5). Briefly, 50 ~ 2000 μL collagen or Matrigel^{TM} solution was placed using a pipette (Eppendorf Research plus) onto the edge of (reticular nanoES) or directly above (mesh nanoES) the nanoES scaffolds, and at ~ 4 ºC. The solutions were allowed to form gels around nanoES under 37 ºC, 5 % CO_2 condition for at least 20 min. For visualization of collagen fibers, fluorescein isothiocyanate labelled collagen type-I (Sigma-Aldrich Corp., St. Louis, MO) was used.

4.2.2.2 NanoES/alginate hybrid scaffold

The 3D nanoES/alginate scaffolds were prepared from pharmaceutical-grade alginate, Protanal LF5/60 (FMC Biopolymers), which has a high guluronic acid (G) content (65%). Briefly, (1) preparation of sodium alginate stock solutions at concentrations of 1% (w/v); (2) partially crosslinking the alginate solution by adding calcium gluconate; (3) drop casting partially crosslinked alginate onto loosely folded mesh nanoES, followed by additional shaping and placement of nanoES inside the alginate gel with a glass rod; (4)

freezing the nanoES/alginate gel in a homogeneous, cold (–20 ºC) environment; and (5) lyophilization to produce a sponge like scaffold (5~15 mm × 2~10 mm, d × h).

4.2.2.3 NanoES/PLGA hybrid scaffold

Poly(lactic-co-glycolic acid) (PLGA) electrospun fibers were used as a secondary scaffold in several experiments. The PLGA fibers were prepared based on reported procedures[26] as follows. PLGA (90/10 glycolide/L-lactide, inherent viscosity 1.71 dL/g in HFIP at 25ºC, Purac Biomaterials Inc.) was dissolved in 1,1,1,3,3,3-hexafluoro-2-propanol (HFIP, Sigma-Aldrich Corp., St. Louis, MO) at a 10 wt% concentration until a clear and homogenous solution was obtained. A syringe pump (Harvard Apparatus, Holliston, MA) was used to deliver the polymer solution through a stainless steel capillary at a rate of 3 mL/hr. A high voltage power supply (Gamma High Voltage Research, Ormond Beach, FL) was used to apply a 25 kV potential between the capillary tip and a grounded stainless steel plate 50 cm away. Fibers were collected for 2-5 minutes before being put aside at room temperature for 72 hours to allow residual solvent evaporate. To prepare hybrid scaffolds, a sheet of PLGA fibers with diameters of ~ 1-3 μm was deposited on both sides of the mesh nanoES. The hybrid scaffold can be folded to increase thickness.

4.2.3 Scaffold mechanical properties

4.2.3.1 Bending stiffness calculations

The effective bending stiffness per unit width of the mesh scaffold, $\overline{D}$, can be estimated by[17]

$$\overline{D} = \alpha_s D_s + \alpha_m D_m \tag{1}$$

where α_s and α_m are the area fraction of the single-layer polymer (SU-8) ribbon (without metal layer and top polymer passivation layer) and three-layer ribbon (bottom polymer layer, metal layer and top passivation layer) in the whole mesh structure. $D_s=E_sh^3/12$ is the bending stiffness per unit width of the single-layer polymer, where E_s=2 GPa and h are the modulus and thickness of the SU-8. D_m is the bending stiffness per unit width of a three-layer structure, which can be calculated by[27]

$$D_m = \frac{E_m b_m h_m^{\ 3}}{12b} + \frac{E_s}{b}\left(\frac{(b-b_m)(2h+h_m)^3}{12} + \frac{1}{6}b_m h^3 + 2b_m h\left(\frac{h}{2}+\frac{h_m}{2}\right)^2\right) \qquad (2)$$

where E_m=121 GPa and h_m are the modulus and thickness of the palladium, b is the width of the single-layer ribbon and the total width of the three-layer ribbon, b_m is the width of the palladium layer. In addition, the chromium layers are so thin (1.5 nm) that their contribution to the bending stiffness is negligible. When h_m=75 nm, h=0.5 μm, b=10 μm, b_m=5 μm, α_s=2.51% and α_m=3.57%, we can calculate $\overline{D}$=0.006 nN·m. When h_m=75 nm, h=2 μm, b=40 μm, b_m=20 μm, α_s=10.06% and α_m=13.31%, we can calculate $\overline{D}$=1.312 nN·m.

To calculate the strain in tubular constructs, we used the equation $\varepsilon=y/R$, where y is the distance from the neutral plane, and R is the radius of curvature[27]. For the symmetric mesh scaffold, since the neutral plane is the middle plane, the maximum strains of metal and SU-8 appear at $y=h_m/2$ and $y=h_m/2+h$, respectively. When h_m=75 nm, h=2 μm, R=0.75 μm^{-1}, the maximum strains of metal and SU-8 are 0.005% and 0.272%, respectively.

4.2.3.2 Scaffold structural simulation

The self-organization of the mesh structure due to residual stress was simulated by the commercial finite element software ABAQUS. Both the SU-8 ribbons and the SU-8 / metal ribbons were modeled as beam elements. The cross-sectional property of the SU-8 / metal ribbons was defined by the appropriate meshed beam cross-section, while the cross-sectional property of the SU-8 ribbons was set by defining the relevant rectangular profile. The equivalent bending moment on SU-8/metal ribbons was calculated using the residual stress measured by MET-1 FLX-2320-S thin film stress measurement system, which were 1.35 and 0.12 GPa for Cr (50 nm) and Pd (75 nm), respectively.

4.2.4 Cell culture

4.2.4.1 Neuron culture

Device chips were cleaned by oxygen plasma (50 sccm of O_2, 50 w, 0.5 Torr, 1 min), and fixed onto a temperature controlled chamber (Warner Instruments, Hamden, CT) with double-sided tape (**Fig. 4-2a**). A 1 mm thick polydimethylsiloxane (PDMS) membrane (Sylgard 184, Dow Corning, Inc., Midland, MI) with 0.25 cm^2 open area in the center was cut, autoclaved and placed over the device area, followed by wire-bonding of individual devices (**Fig. 4-2b**). An autoclaved glass ring (ALA Scientific Instruments, Farmingdale, NY) was placed over this PDMS chamber and fixed with Kwik-Sil (World Precision Instruments, Inc., Sarasota, FL) silicone elastomer (**Fig. 4-2c**). The whole chip was sterilized by UV illumination and 75% ethanol soak (20 min each). An aqueous polylysine solution (0.5-1.0 mg/mL, MW 70,000 – 150,000, Sigma-Aldrich) was then introduced into the chamber and incubated overnight at 37 ºC, the polylysine solution

was removed, and the chamber rinsed 3 times each with 1X phosphate buffered saline (PBS) solution and NeuroPure Plating Medium (Genlantis, San Diego, CA). Finally, the chamber was filled with NeuroPure Plating Medium or culture medium and conditioned in the incubator for 1 day. Hippocampal neurons (Gelantis, CA) were prepared using a standard protocol[28]. In brief, 5 mg of NeuroPapain Enzyme (Gelantis, CA) was added to 1.5 ml of NeuroPrep Medium (Gelantis, San Diego, CA). The solution was kept at 37 ºC for 15 min, and sterilized with a 0.2-μm syringe filter (Pall Corporation, MI). Day 18 embryonic Sprague/Dawley rat hippocampal tissue with shipping medium (E18 Primary Rat Hippocampal Cells, Gelantis, San Diego, CA) was spun down at 200 g for 1 min. The shipping medium was exchanged for NeuroPapain Enzyme medium. A tube containing tissue and the digestion medium was kept at 30 ºC for 30 min and manually swirled every 2 min, the cells were spun down at 200 g for 1 min, the NeuroPapain medium was removed, and 1 mL of shipping medium was added. After trituration, cells were isolated by centrifugation at 200 g for 1 min, then re-suspended in 5-10 mg/mL Matrigel™ (BD Bioscience, Bedford, MA) at 4 ºC. The cell/Matrigel™ mixture was plated on the reticular nanoES in the opening in the PDMS membrane at a density of 2 – 4 million cells /mL and a total gel thickness of ~ 0.5-1 mm. The Matrigel™ matrix was allowed to gel at 37 ºC for 20 min, then 1.5 ml of NeuroPure Plating Medium was added, and the entire assembly was placed in the incubator. After 1 day, the plating medium was changed to Neurobasal™ medium (Invitrogen, Grand Island, NY) supplemented with B27 (B27 Serum-Free Supplement, Invitrogen, Grand Island, NY), Glutamax™ (Invitrogen, Grand Island, NY) and 0.1% Gentamicin reagent solution (Invitrogen, Grand Island, NY)[29]. 3D neuron cultures were maintained at 37 °C with 5% CO_2 for 7-21 days, with medium

changed every 4-6 days. For cultures lasting longer than 7 days, gas-permeable/water-impermeable membrane covers (ALA MEA-MEM-PL, ALA Scientific Instruments, Farmingdale, NY) were used to avoid evaporation while allowing for diffusion of gases (**Fig. 4-2d**).

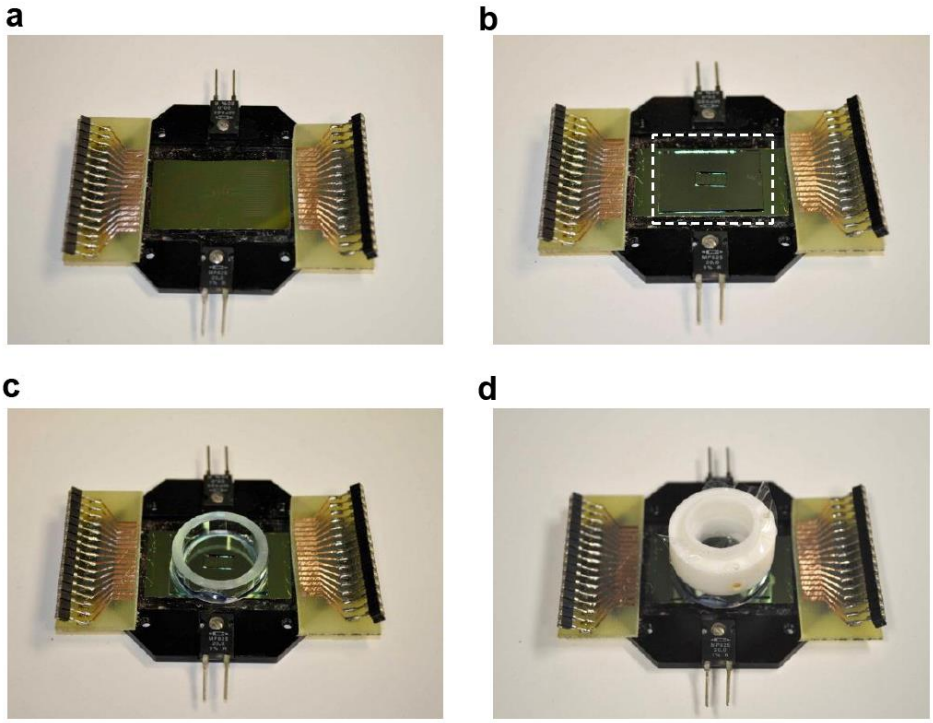

Figure 4-2 Chip assembly for neuronal 3D cultures. **a**, A nanowire FET device chip containing a reticular nanoES was cleaned by O_2 plasma, and assembled onto a temperature controlled chip carrier. **b**, A shallow PDMS chamber (dashed box) was cleaned and placed over the wire-bonded devices. **c**, A glass ring was fixed over the PDMS chamber with silicone elastomer. **d**, A gas-permeable, water-impermeable membrane cover was used for neuron cultures lasting longer than 7 days.

4.2.4.2 Cardiomyocyte culture

Hybrid scaffolds (**Fig. 4-3b**) consisting of the mesh nanoES (**Fig. 4-3a** and **Fig. 4-3g**) sandwiched between two electrospun PLGA fiber layers (1-3 μm diameter; 10-20 μm thick for individual layer) were used in all experiments. The bottom PLGA layer was

made either by inserting an existing layer underneath the mesh-like scaffold or by directly electrospinning on the nanoES. The top PLGA layer was made by direct electrospinning on the nanoES. The device chip was wire-bonded (**Fig. 4-3c** and **Fig. 4-3h**), and assembled with a modified polystyrene petri-dish (VWR Inc.) using Kwik-Sil (World Precision Instruments, Inc.) silicone elastomer glue (**Fig. 4-3d**). The device chamber was cleaned by oxygen plasma (50 sccm of O_2, 50 w, 0.5 Torr, 1 min), followed by sterilization with UV-light illumination for 1 h and soaking in 70 % ethanol solution for 0.5 h. The hybrid scaffolds were coated with fibronectin/gelatin solution overnight prior to cell seeding. The fibronectin/gelatin solution was prepared by adding 0.1 g Bacto-Gelatin (Fisher Scientific, DF0143-17-9) to 500 mL distilled water in a glass bottle and autoclaving. The gelatin dissolved during the autoclaving step to yield a final concentration of gelatin of 0.02 %. One ml Fibronectin (Sigma, F-1141) was diluted in 199 mL of 0.02 % gelatin. Cardiac cells were isolated from intact ventricles of 1 to 3-day-old neonatal Sprague/Dawley rats using 3–4 cycles (30 min each) of enzyme digestion using collagenase type II and pancreatin as described elsewhere[30]. The cells were suspended in culture medium, composed of Medium-199 (Invitrogen, Grand Island, NY) supplemented with 0.6 mM $CuSO_4 \cdot 5H_2O$, 0.5 mM $ZnSO_4 \cdot 7H_2O$, 1.5 mM vitamin B12, 500 U/mL penicillin, 100 mg/mL streptomycin and 5 vol.% fetal calf serum (FCS)[30]. The cardiac cells were finally seeded with 5-10 mg/mL Matrigel^{TM} onto fibronectin/gelatin coated PLGA/mesh nanoES at an initial cell density of $3\text{-}6\times10^7$ cm^{-2} (**Fig. 4-3e**). After 1-2 days, the cell-seeded nanoES was manually folded into a construct, and was maintained at 37 °C with 5% CO_2 for an additional 3-8 days (**Fig. 4-3f**), with medium changes every 2-3 days. All animal procedures conformed to US National

Institutes of Health guidelines and were approved by Harvard University's Animal Care and Use Committee.

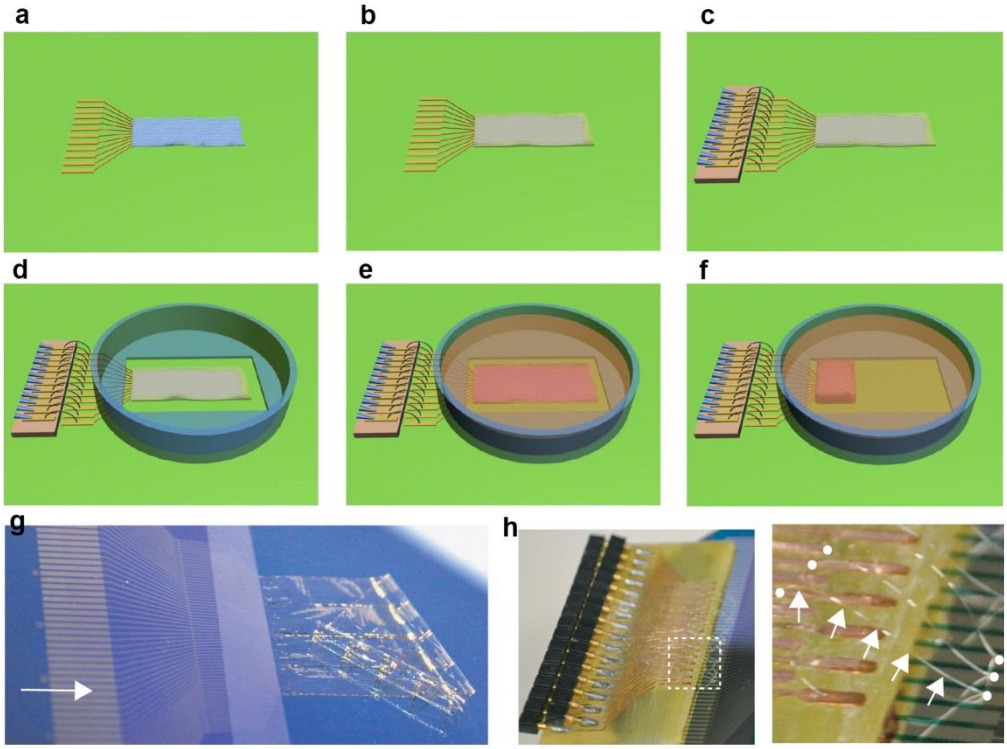

Figure 4-3 Schematic of cardiomyocyte 3D culture. a, A free-standing mesh-like nanoES. **b**, Hybrid of PLGA electrospun fibers and mesh-like nanoES. **c**, Individual devices were wire-bonded to PCB connecters. **d**, A modified petri-dish was fixed over the scaffold with silicone elastomer. **e**, The hybrid scaffold was sterilized by UV-light illumination for 1 h and soaking in 70 % ethanol solution for 0.5 h, coated with fibronectin/gelatin solution overnight and seeded with cardiomyocytes/MatrigelTM. **f**, After 1-2 days in culture, the cardiac sheet (**e**) was folded and cultivated for an additional 3-10 days. **g**, A mesh device showing the free-standing part (the right half) and the fixed part on the wafer (the left half). The arrow marks the outer-electrode pins for wire-bonding. **h**, Printed circuit board (PCB) with wire-bonding wires. The wires connected the PCB copper pads (left) and the rectangular electrodes on the supported end of the mesh-like nanoES (right). White dots highlight bonding points. Arrows highlight one wire-bonded aluminum wire.

4.2.4.3 Vascular construct

Synthetic vascular constructs were produced in a manner similar to the sheet-based tissue engineering approach described previously[31] (**Fig. 4-4**). First, the mesh

nanoES were coated with gelatin/fibronectin solution overnight (**Figs. 4-4a-c**). Second, human aortic smooth muscle cells (HASMC, Invitrogen, Grand Island, NY) were seeded at a density of 1×10^4 cm^{-2} on the gelatin/fibronectin-coated devices and cultured in Medium 231 (Invitrogen, Grand Island, NY) supplemented with smooth muscle growth supplement (SMGS, Invitrogen) (**Fig. 4-4d**). Sodium L-ascorbate (50 μg/mL, Sigma) was added to the culture medium to stimulate extracellular matrix (ECM) synthesis[31]. HASMCs were maintained at 37 ºC with 5% CO_2 until their secreted ECM proteins formed an cohesive tissue sheet (7-14 days)[31] that can be easily peeled off from the silicon substrate. The cell-coated mesh nanoES was then gently lifted from the SiO_2 substrate using fine forceps, rolled onto a polystyrene or glass tubular support 1.5 mm in diameter, then maintained in culture Medium 231 supplemented with SMGS and 50 $\mu g \cdot mL^{-1}$ sodium L-ascorbate for at least another 2 weeks for maturation of the vascular structure (**Fig. 4-4e**). 0.5-2 h prior to pH sensing experiments, the temporary tubular support was removed, and segments of polystyrene tubing were connected to the open ends of the vascular construct (**Fig. 4-4f**), and a PDMS fluidic chamber with input/output tubing and Ag/AgCl was sealed with the silicon substrate and the vascular construct using silicone elastomer glue (Kwik-Sil, World Precision Instruments, Inc.) as shown in **Fig. 4-4h**. Fresh medium was delivered to the vascular construct through both inner and outer tubing. The pH of the solution delivered through the outer tubing was varied during the experiment.

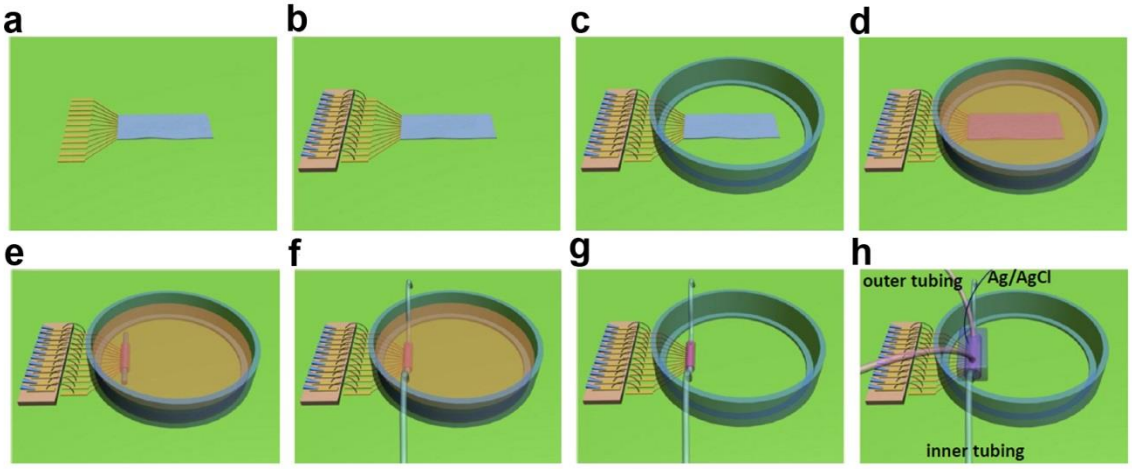

Figure 4-4 Schematic of vascular nanoES construct preparation and pH sensing. a, A free-standing mesh-like nanoES. **b**, Individual devices were wire-bonded to PCB connecters. **c**, A modified petri-dish was fixed over the scaffold with silicone elastomer. **d**, The hybrid scaffold was sterilized with UV-light illumination for 1 h and soaking in 70 % ethanol solution for 0.5 h, coated with fibronectin/gelatin solution overnight and seeded with HASMCs. **e**, After 7-14 days in culture, the HASMC-seeded nanoES (**d**) was rolled against a tubular support and cultivated for at least another 14 days. **f**, The tubular support was removed and tubing was connected to the ends of the lumen of the HASMC construct. **g**, The medium was removed while keeping the construct moist. **h**, A PDMS chamber was assembled around the construct, attached to tubing to bathe the outside of the construct and Ag/AgCl electrodes to measure pH in the bathing fluid.

4.2.5 Immunochemical staining

Cells were fixed with 4% paraformaldehyde (Electron Microscope Sciences, Hatfield, PA) in PBS for 15-30 min, followed by 2-3 washes with ice-cold PBS. Cells were pre-blocked and permeabilized (0.2-0.25% Triton X-100 and 10% feral bovine serum or 1 % bovine serum albumin (BSA) in PBS) for 1 hour at room temperature. Next, the cells were incubated with primary antibodies in 1% BSA in 1X PBS with 0.1% (v/v) Tween 20 (PBST) for 1 hr at room temperature or overnight at 4 ^{o}C. Then cells were incubated with the secondary antibodies with fluorophores. For counter-staining of cell nuclei, cells were incubated with 0.1-1 μg/mL Hoechst 34580 (Molecular Probes, Invitrogen, Grand Island, NY) for 1 min. Specific reagents used for different cell types

were as follows. *Neurons:* Neuronal class III β-Tubulin (TUJ1) mouse monoclonal antibody (1:500 dilution, Covance Inc., Princeton, NJ) and AlexaFluor-546 goat anti-mouse IgG (1:1000, Invitrogen, Grand Island, NY) were used as the primary and secondary antibodies, respectively[32]. *Cardiomyocytes:* Anti-α-actinin mouse monoclonal antibody (1:450; Clone EA-53, Sigma-Aldrich Corp., St. Louis, MO) and AlexaFluor-488 goat anti-mouse (1:200; Molecular Probes, Invitrogen, Grand Island, NY) were used as the primary and secondary antibodies, respectively[29]. Hoechst 34580 was used to counter-stain cell nuclei. *HASMC:* Anti-smooth muscle α-actin rabbit polyclonal antibody (1:500, Abcam, Cambridge, MA) and AlexaFluor-488 donkey anti-rabbit antibody (1:200; Molecular Probes, Invitrogen, Grand Island, NY) were used as the primary and secondary antibodies, respectively. Hoechst 34580 was used to counter-stain cell nuclei.

4.2.6 Fluorescent dye labeling of devices and PLGA fibers

Fluorescence images of the reticular nanoES were obtained by doping the SU-8 resist solution with rhodamine 6G (Sigma-Aldrich Corp., St. Louis, MO) at a concentration less than 1 μg/mL before deposition and patterning. PLGA electrospun fiber scaffolds were labeled by physical absorption of rhodamine 6G from an aqueous solution (0.1 mg/mL), and then rinsed copiously with water before fluorescence imaging.

4.2.7 Hematoxylin-eosin and Masson trichrome staining

The vascular constructs were cut and fixed in formalin solution (10 %, neutral buffered, Sigma-Aldrich Corp., St. Louis, MO). The fixed sample was dehydrated in a series of graded ethanol baths (70 % ethanol for 1 h, 95 % ethanol for 1 h, absolute

ethanol 3x times, 1 h each) and xylenes (2x, 1 h each), and then infiltrated with molten paraffin (*HistoStar*, Thermo Scientific, Kalamazoo, MI) at 58 ^{o}C for 2 h. The infiltrated tissues were embedded into paraffin blocks and cut into 5-6 μm sections. Immediately prior to straining, the paraffin was removed from the sections by 2 washes with xylene, 1 min each. Then the sections were rehydrated by a 5 min wash in absolute ethanol, 2 min in 95 % ethanol, 2 min in 70 % ethanol and 5 min in distilled water. Standard hematoxylin and eosin staining[33] was carried out using an automated slide stainer (Varistain Gemini ES, Thermo Scientific, Kalamazoo, MI). Collagen secretion by HASMCs was assessed on deparaffinized sections using a Masson's trichrome staining kit (Polysciences, Inc., Warrington, PA) according to a standard protocol[34].

4.2.8 Optical microscopy and image analysis

Confocal and epi-fluorescence imaging was carried out using an Olympus Fluoview FV1000 confocal laser scanning microscope. Confocal images were acquired using 405, 473 and 559 nm wavelength lasers to excite cellular components labeled with Hoechst 34580, AlexaFluor-488/Rodamine-6G, and Rodamine-6G/AlexaFluor-546 fluorescent dyes (Molecular Probes and Sigma-Aldrich Corp.), respectively. A 635 nm wavelength laser was used for imaging metal interconnects in reflective mode. Epi-fluorescence images were acquired using a mercury lamp together with standard DAPI (EX:377/50,EM:447/60), GFP (EX:473/31,EM520/35) and TRITC (EX:525/40,EM:585/40) filters. *ImageJ* (ver. 1.45i, Wayne Rasband, National Institutes of Health, USA) was used for 3D reconstruction and analysis of the confocal and epi-fluorescence images. Bright-field optical micrographs of histological samples were acquired on an Olympus FSX100 system using FSX-BSW software (ver. 02.02).

4.2.9 Micro-computed tomography

The nanoES in the synthetic vascular construct was imaged using a HMXST Micro-CT x-ray imaging system with a standard horizontal imaging axis cabinet (model: HMXST225, Nikon Metrology, Inc., Brighton, MI). Prior to imaging, samples were fixed and dried. In a typical imaging process, 60-70 kV acceleration voltage and 130-150 μA electron beam current was used. No filter was used. *VGStudio MAX* (ver. 2.0, Volume Graphics GMbh, Germany) was used for 3D reconstruction and analysis of the micro-CT images.

4.2.10 Cell viability assays

Hippocampal neuron viability was evaluated using a LIVE/DEAD® Viability/Cytotoxicity Kit (Molecular Probes, Invitrogen, Grand Island, NY). On days 7, 14 and 21 of the culture, neurons were incubated with 1 μM calcein-AM and 2 μM ethidium homodimer-1 (EthD-1) for 45 min at 37 °C to label live and dead cells, respectively[29]. Cell viability at each time point was calculated as live/(live + dead) × 100, and been normalized to the percentage of live cells on day 0 ($live_{day=n}/live_{day=0}$). Three-dimensional neuron cultures in Matrigel™ on polylysine modified glass slides (Fisher Scientific Inc., Waltham, MA) were used as controls. The cells were imaged with a confocal fluorescence microscope (Olympus Fluoview FV1000) and the 3D reconstructed images were used for live/dead cell counting. For each group, n = 6. In 3D cardiac cultures, cell viability was evaluated with an assay of a mitochondrial metabolic activity, the CellTiter 96® AQueous One Solution Cell Proliferation Assay (Promega Corp., Madison, WI) that uses a tetrazolium compound [3-(4,5-dimethyl-2-yl)-5-(3-carboxymethoxyphenyl)-2-(4-sulfophenyl)-2H-tetrazolium, inner salt; MTS] and an

electron coupling reagent (phenazine ethosulfate; PES)[35]. On days 2, 4, 6, 8, 10 and 12 of the culture, cardiac constructs were incubated with CellTiter 96® AQueous One Solution for 120 min at 37 °C. The absorbance of the culture medium at 490 nm was immediately recorded with a 96-well plate reader. The quantity of formazan product (converted from tetrazole) as measured by the absorbance at 490 nm is directly proportional to cell metabolic activity in culture. Three-dimensional cardiomyocyte cultures in Matrigel™ on gelatin coated electrospun PLGA fibers were used as controls. For each group, n = 6.

4.2.11 Electrical measurements

The nanowire FET conductance and transconductance (sensitivity) were measured in 1× PBS as described previously[18]. The slope of a linear fit to conductance versus water-gate potential (V_{gate}) data was used to determine transconductance. For nanowire FET stability tests, the reticular NWFET devices were maintained under neuron culture conditions (see *Neuron culture*) for predetermined intervals. Electrical transport measurements and recordings from 3D cardiomyocyte-seeded nanoES were obtained in Tyrode solution (pH ~ 7.3) with a 100 mV DC source voltage at 25 ^{o}C or 37 ^{o}C as described previously[18, 20]. The current was amplified with a multi-channel current/voltage preamplifier, filtered with a 3 kHz low pass filter (CyberAmp 380), and digitized at a 50 kHz sampling rate (Axon Digi1440A). In extravascular pH sensing experiments, a single polydimethylsiloxane (PDMS) microfluidic chamber was used to deliver two flows of phosphate buffer solutions: the pH delivered by the outer input tubing was varied, while that of the inner tubing was fixed at 7.4. In the pH-sensing experiments, nanoelectronic devices were modulated using a lock-in amplifier with a modulation frequency of 79 and

39 Hz, time constant of 30 ms, amplitude of 30 mV, and DC source-drain potential of zero. Ag/AgCl reference electrodes were used in all recording and sensing experiments.

4.3 Results and discussion

4.3.1 nanoES characterization

We have designed two nanoES (**Fig. 4-5**) that are free-standing, flexible and contain similar components. Reticular nanoES (**Fig. 4-5a**) were made by electron beam lithography. Self-organization (that is, folding according to the predefined layout of bending elements) created a random or regular network of 3D features that mimic the size scale and morphology of submicron ECM features, such as the fibrous meshwork of brain ECM[36]. Open mesh nanoES (**Fig. 4-5b**) were made by photolithography with a regular structure, similar to the ECM of the ventricular myocardium[37, 38]. 3D scaffolds were then realized in a straightforward manner by directed mesh manipulation. The planar design and initial fabrication of these 3D nanoES use existing capabilities developed for conventional planar nanoeletronics, and could enable integration of additional device components (for example, memories and logic gates)[39,40] and substantial increases in device number and overall scaffold size.

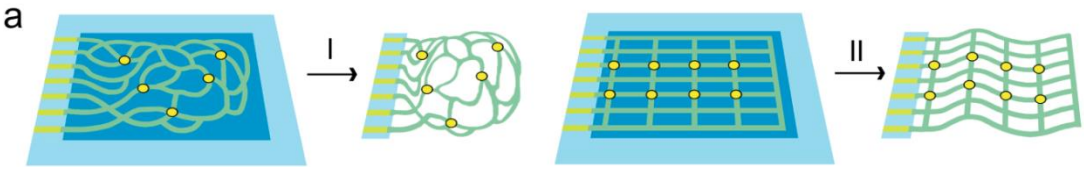

Figure 4-5 Macroporous and flexible nanowire nanoES. a, Device fabrication schematics. **I**: Reticular nanowire FET devices. **II**: mesh nanowire FET devices. Light blue: silicon oxide substrates, blue: nickel sacrificial layers, green: nanoES, yellow dots: individual nanowire FETs.

The 2D structure of the reticular scaffold was designed so that metal interconnects were stressed[18, 41]. Removal of the sacrificial layer prompted self-organization into 3D. Reconstructed 3D confocal fluorescence images of typical reticular scaffolds viewed along *y*- and *x*- axes (**Fig. 4-6a, I** and **II** respectively) showed that the framework was 3D with a highly curvilinear and interconnected structure. The porosity (calculated from the initial planar device design and the final 3D construct volume) was > 99.8 %, comparable to that of hydrogel biomaterials[6-8]. Scanning electron microscopy (SEM) of the reticular nanoES (**Fig. 4-6b**) revealed kinked nanowires (ca. 80 nm diameter), and metallic interconnects (ca. 0.7 μm width) contained within the SU-8 backbone (ca. 1 μm width). The feature sizes are comparable to those of synthetic and natural ECMs[3,8], and are several orders of magnitude smaller than those for electronic structures[23] penetrating tissue in three dimensions.

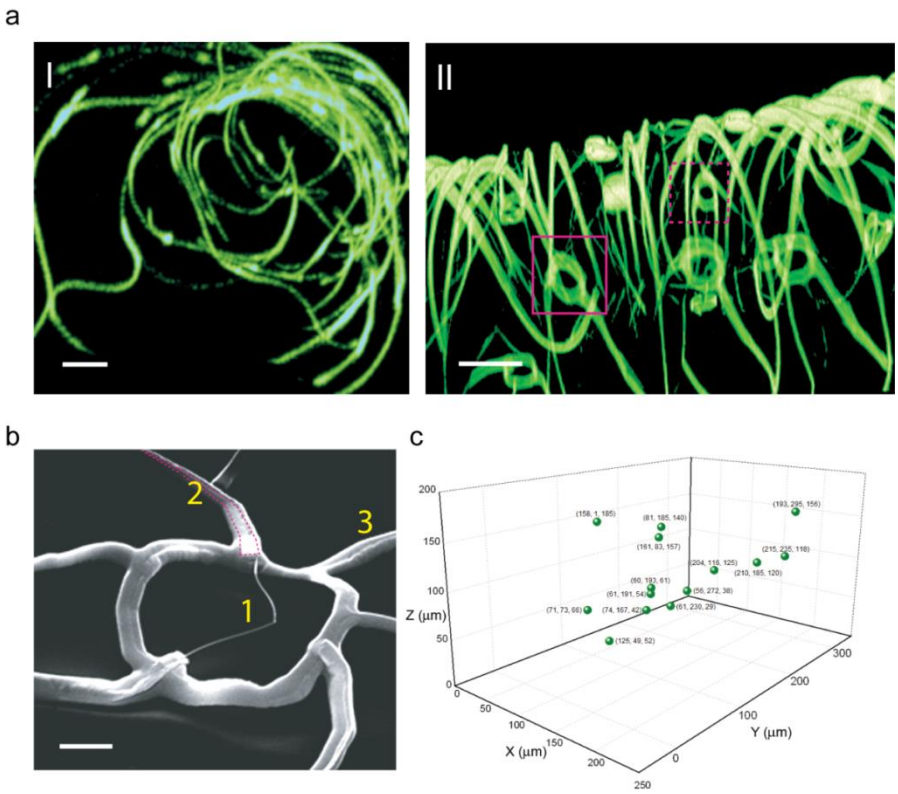

Figure 4-6 Reticular nanowire nanoES. a, 3D reconstructed confocal fluorescence images of reticular nanoES viewed along y (**I**) and x (**II**) axes. The scaffold was labeled with rhodamine 6G. The overall size of the structure, x-y-z = 300-400-200 μm. Solid and dashed open magenta boxes indicate two nanowire FET devices located on different planes along x axis. Scale bars, 20 μm. **b**, SEM image of a single kinked nanowire FET within a reticular scaffold, showing (1) kinked nanowires, (2) metallic interconnects (magenta lines) and (3) the SU-8 backbone. Scale bar, 2 μm. **c**, 14 nanowire FETs were distributed in the construct shown in a, Individual devices are shown as solid green spheres, with (x, y, z) coordinates in microns denoted for each device point. The overall size of the scaffold, x-y-z was ~ 300-400-200 μm. The nanowire FET devices within the scaffold were separated in 3D by 7.3 to 324 μm.

Nanowire FET devices (**Fig. 4-6a, II**) within the scaffold spanned separations of 7.3 to 324 μm in 3D (**Fig. 4-6c**), and the reticular scaffold heights were less than ~ 300 μm for our current fabrication conditions. Devices can be made closer together (for example, < 0.5 μm) by depositing denser nanowires on the substrate[40] to improve spatial resolution of nanoelectronic sensors; the span of device separations and scaffold heights can be increased substantially using larger field lithography (see below). The

performance of devices was evaluated through water-gate measurements for the nanowire FET elements in the 3D scaffolds in aqueous medium. The results show device yields (~80 %), conductances (1.52 ± 0.61 µS; mean ± SD) and sensitivities (8.07 ± 2.92 µS/V), comparable to measurements from planar devices using similar nanowires[18].

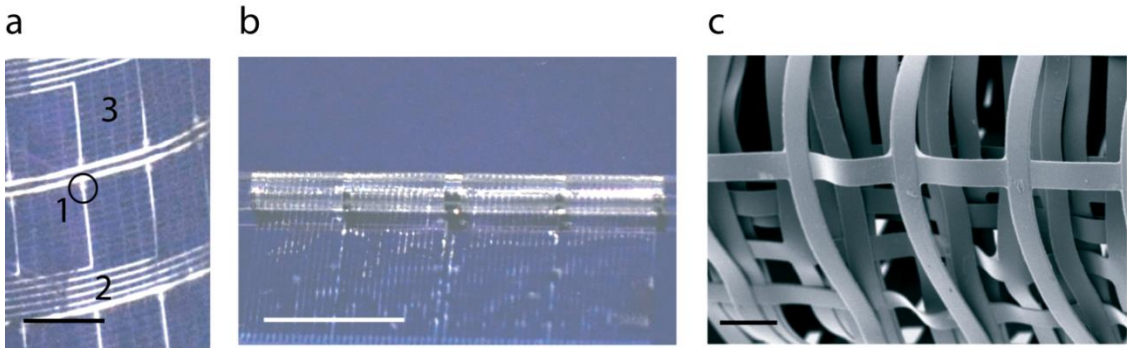

Figure 4-7 Mesh nanowire nanoES. a, Photograph of a mesh device, showing (1) nanowires, (2) metal interconnects, (3) SU-8 structural elements. The circle indicates the position of a single nanowire FET. Scale bar, 2 mm. **b**, Photograph of a partially rolled-up mesh device. Scale bar, 5 mm. **c**, SEM image of a loosely packed mesh nanoES, showing the macroporous structure. Scale bar, 100 µm.

3D mesh nanoES were realized by folding and rolling free-standing device arrays. Mesh structures (**Fig. 4-5a, II**) were fabricated such that the nanoES maintained an approximately planar configuration following relief from the substrate. A typical 3.5 cm × 1.5 cm × ~ 2 µm mesh nanoES, was approximately planar with 60 nanowire FET devices in regular array with a 2D open porosity of 75 % (**Fig. 4-7a**). This mesh porosity is comparable to that of honeycomb-like synthetic ECM engineered for cardiac tissue culture[38]. In addition, the nanowires (**Fig. 4-7a, I**), metal interconnects (**Fig. 4-7a, 2**), and SU-8 structural elements (**Fig. 4-7a, 3**) had an areal mass density of < 60 µg/cm^2, the lowest value reported so far for flexible electronics, which reflects our macroporous architecture. The mesh nanoES was flexible and can be manually rolled into tubular constructs with inner diameters at least as small as 1.5 mm (**Fig. 4-7b**), and folded.

Macroporous structures of the open mesh nanoES were formed either by loosely stacking adjacent mesh layers (**Fig. 4-7c**) or by shaping it with other biomaterials. These capabilities were consistent with the estimated ultralow effective bending stiffness, which was tuned between 0.006 – 1.3 nN·m for this mesh and is comparable to recent planar epidermal electronics[17].

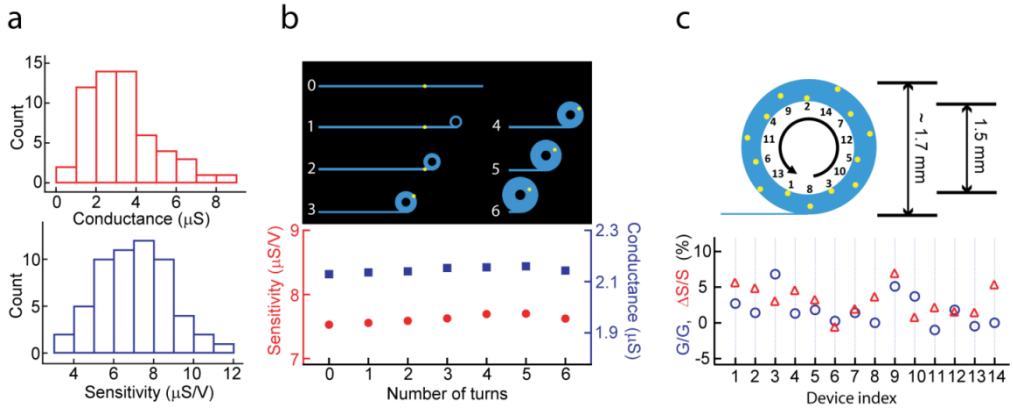

Figure 4-8 Device performance characterization. a, Histograms of nanowire FET conductance and sensitivity in one typical mesh nanoES. The conductance and sensitivity were measured in water-gate configuration without rolling. The device yield for this mesh nanoES is 95 %. **b**, Water-gate sensitivity and conductance of a nanowire FET device in a mesh device during the rolling process. Upper panel, schematic of nanowire FET position (yellow dot) during rolling process; 0-6 denote the number of turns. **c**, Relative change in conductance and sensitivity of 14 nanowire FETs evenly distributed throughout a fully rolled-up mesh device. Upper panel, schematic of nanowire FET position (yellow dots). In (**b**) and (**c**) the thicknesses of the tubular structures have been exaggerated for schematic clarity.

The electrical transport characteristics of the mesh nanoES were evaluated in phosphate buffered saline (PBS). The typical device yield is 90-97 %, with average device conductance ~ 3μS and sensitivity ~ 7 μS/V (**Fig. 4-8a**). Representative conductance (*G*) data (**Fig. 4-8b**) from single nanowire FET (**Fig. 4-8b**, yellow dots, upper panel) during the rolling process showed a <0.17 μS conductance change (ΔG) or <2.3% total change for 6 revolutions. Device sensitivity (*S*) remained stable with a

maximum change (ΔS) of 0.031 μS/V, or 1.5% variation. The stable performance during rolling can be explained by the low estimated strains of metal (<0.005%) and SU-8 (<0.27%) in this tubular construct, and showed that the properties were approximately independent of location. Furthermore, 14 devices evenly distributed on 6 layers of a rolled-up scaffold (**Fig. 4-8c**) showed maximum differences of $\Delta G = 6.8$ and $\Delta S = 6.9\%$ versus the unrolled state, demonstrating device robustness. Repetitive rolling and relaxation to the flat state did not degrade nanowire FET performance. These findings suggest potential for reliable sensing/recording of dynamic and deformable systems.

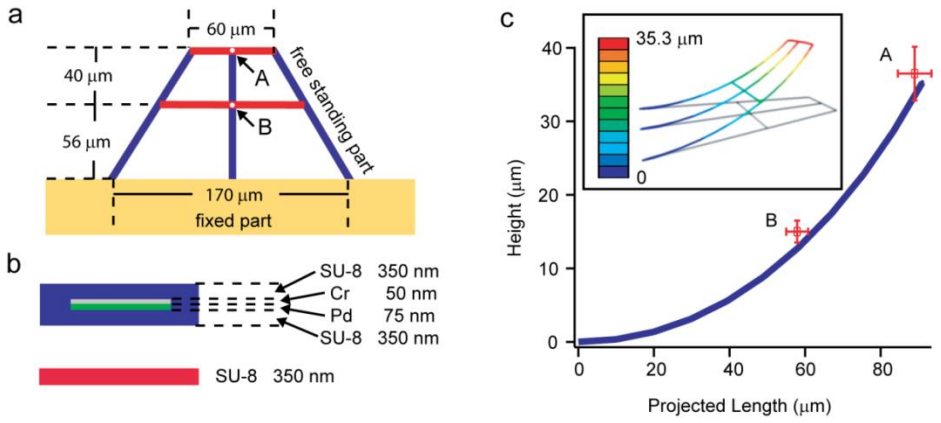

Figure 4-9 Geometry control by design in nanoES. (**a, b**), Basic design and structural subunit for simulation. **a**, Top-down view of the entire subunit. Blue ribbons are stressed metal lines with SU-8 passivation. Red lines are single SU-8 ribbons without residual stress. **b**, Cross-sectional views of those two key structural elements used for simulation. **c**, Plot of projected (on x-y plane) length versus height (in z direction) for the vertical blue ribbon in (**a**) as determined from the simulation. Open red squares with error bars are experimental data recorded in air for point A and B in (**a**). The simulation of the bending of the subunit model for the reticular structure was carried out using the commercial finite element software ABAQUS. Inset shows a 3D view of the simulated structure, and the scale bar shows different height in z direction.

4.3.2 Mechanical design

We have carried out simulations of a subunit of the self-organizing reticular structure (**Fig. 4-9a-c**). Measurements of bending for the corresponding experimental

structures (**Fig. 4-9c**, open red squares) are consistent with the simulation (**Fig. 4-9c**). Additionally, changes in structural parameters (for example, total length of subunit and thicknesses of SU-8 or metals) yield predictable changes in the bending angle of the subunit (**Fig. 4-10**). In this way, ordered 3D nanowire FET arrays can be designed and fabricated using reticular- or mesh-like structures that incorporate multi-layer metal interconnects with built-in stress to self-organize (roll-up) the scaffold (**Fig. 4-10**).

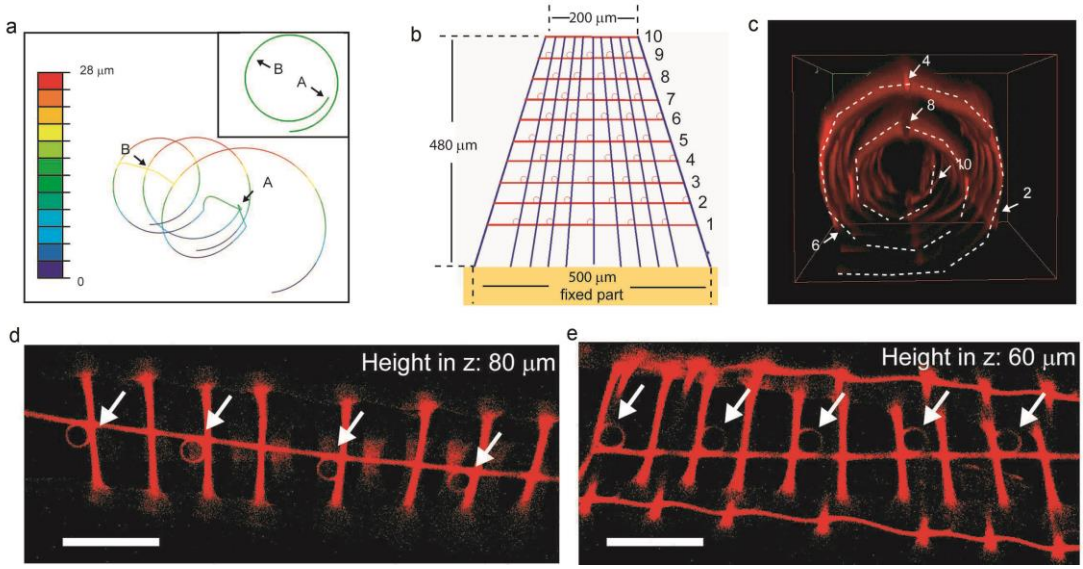

Figure 4-10 Design and fabrication of reticular nanoES. a, Simulation shows that when the equivalent bending moment is increased by 10 times, the subunit structure scrolls up on itself. Inset shows the curve of the central blue ribbon in **Figure 4-9a**, demonstrating the devices were scrolled up and different layers were separated. A and B are the two points in **Figure 4-9a**. (**b-e**), Design and fabrication of a much larger and regular matrix, the density of stressed elements increasing upward (from 1 to 10) in a manner analogous to the simulated subunit. **b**, The blue lines indicate stressed metal lines with SU-8 as passivation, red lines indicate non-stressed metal lines for interconnection with SU-8 as passivation or SU-8 ribbon as framework, and the circles mark positions for devices. **c**, 3D reconstructed confocal fluorescence image shows the side-view of the corresponding fabricated reticular construct following the design in (**b**). The dashed lines (**c**) highlight the edge of the 'scrolled-up' reticular nanoES construct. The white numbers and arrows indicate the position of 5 horizontal lines corresponding to those numbered in b. (**d, e**), Confocal fluorescence images scanned across the interior of the scaffold at different heights. The images demonstrate that the device regions (circles) are located in planes (heights of 80 and 60 μm are shown) are aligned, and thus demonstrate the regular arrangement in 3D. Scale bars in (**d**) and (**e**) are 50 μm. Overall, the results suggest that larger scale simulations could be used to predict the reticular construct geometry, and

(Continued) allow our self-assembling approach to provide regular (or irregular) device arrays distributed through 3D space by design.

Finally, we have designed reticular domains in mesh-like structures (**Fig. 4-11a**). Images of reticular domains (**Fig. 4-11b** and **Fig. 4-11c**) show that regular nanowire FET devices with distinct device positions can be realized by varying the structural parameters of individual elements. Overall, this approach yields hierarchical 3D nanoES with sub-micrometer to micrometer scale control in reticular domains and millimeter to centimeter scale in the mesh matrix by folding or rolling as shown above (**Fig. 4-7**).

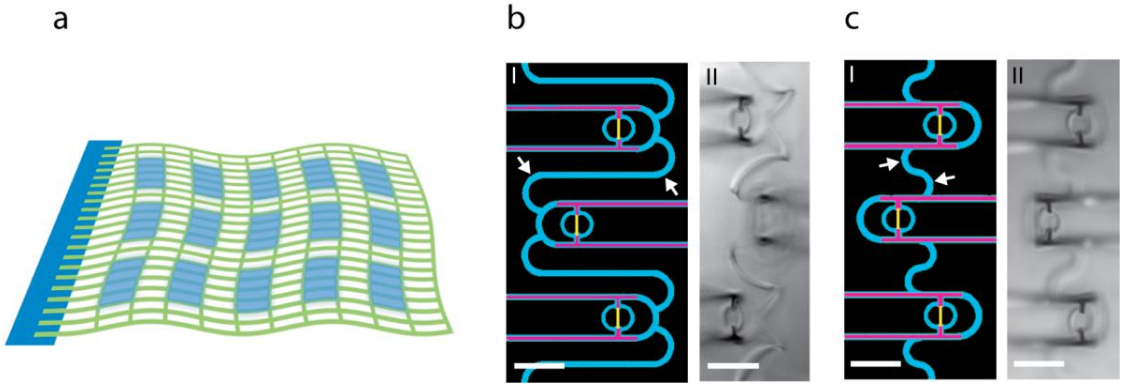

Figure 4-11 Reticular-mesh nanoES. a, Schematic showing the integration of periodic reticular-device domains (light blue) into a flexible mesh (green). In individual reticular domains, the 3D device positions relative to the global flexible mesh can be controlled by their geometry designs. (**b, c**) Design patterns (**I**) and experimental data (**II**) for two reticular units. SU8, metal and nanowires are shown in blue, pink and yellow in **b**. Changing the structure of the connecting feature (white arrows) between adjacent device units during pattern design (**I**) yields controlled variations in 3D positioning of the nanowire FETs, which can be further tuned by the stress in the metal connections. In these experiments, the device positions are 40 μm (**b, II**) and 23 μm (**c, II**) above the mesh plane. Scale bars in **b** and **c**, 20 μm.

4.3.3 Characterization of nanoES/tissue scaffold hybrids

The reticular and mesh nanoES also were merged with conventional macroporous biomaterials. Specifically, gel casting, lyophilization and electrospinning were used to deposit and construct macroporous collagen (**Fig. 4-12a**), alginate (**Fig. 4-12b**), and

poly(lactic-co-glycolic acid) (PLGA) (**Fig. 4-12c**), respectively, around nanoES. A confocal fluorescence microscopy image of a hybrid reticular nanoES/collagen

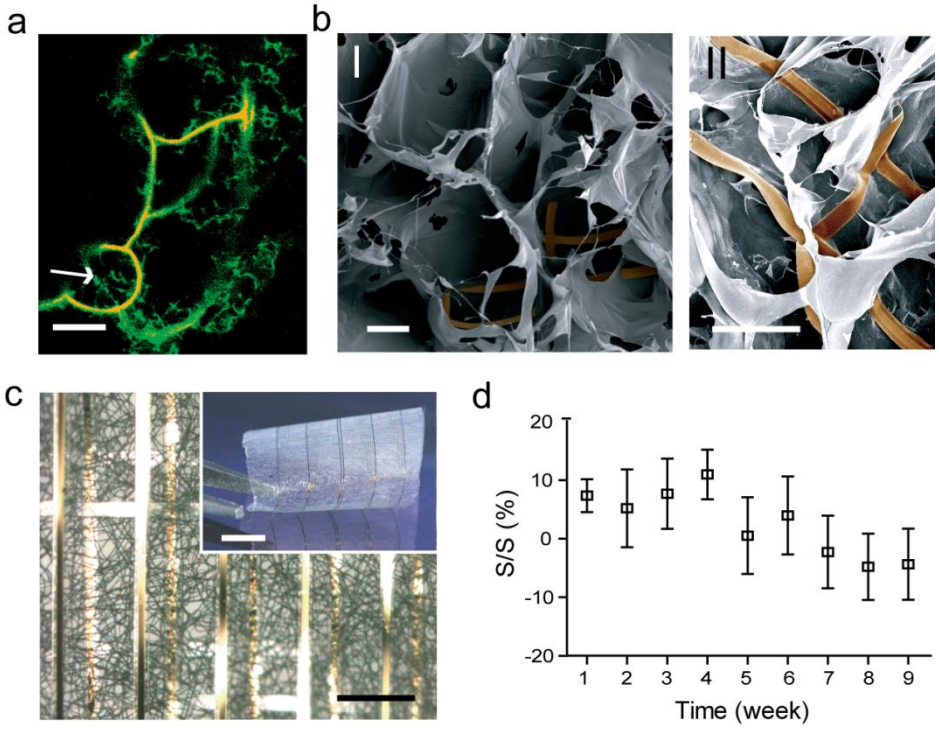

Figure 4-12 Hybrid macroporous nanoelectronic scaffolds. **a**, Confocal fluorescence micrograph of a hybrid reticular nanoES/collagen matrix. Green (Fluorescein isothiocyanate): collagen type-I, organge (rhodamine 6G): epoxy ribbons. White arrow marks the position of nanowire. Scale bar, 10 μm. **b**, SEM images of mesh nanoES/alginate scaffold, top (**I**) and side (**II**) views. The epoxy ribbons from nanoES are false-colored in brown for clarity. Scale bars, 200 μm (**I**) and 100 μm (**II**). **c**, A bright-field optical micrograph of the folded scaffold, showing multilayered structures of PLGA and nanoelectronic interconnects. Inset shows the photograph of the hybrid sheet before folding. A sheet of PLGA fibers with diameters of ~ 1-3 μm was deposited on both sides of the device. No damage or reduction of device yield was observed following this deposition. Scale bars, 200 μm and 5 mm (inset). **d**, Relative changes in nanowire FET sensitivity over time in culture (37 ºC; 5 % CO_2, supplemented Neurobasal^{TM} medium). n = 5; data are means ± SD.

scaffold (**Fig. 4-12a**) shows clearly that the collagen nanofibers (green) are fully entangled with the nanoES, with no evidence of phase separation. Scanning electron microscopy (SEM) images of the open mesh nanoES/alginate hybrid scaffold produced by lyophilization (**Fig. 4-12b**) show that the flexible nanoES mesh is intimately anchored

to the alginate framework, which has a similar pore structure as the pure alginate scaffold prepared under similar conditions. Finally, optical microscopy images of a multilayered mesh nanoES/PLGA scaffold (**Fig. 4-12c**), which was prepared by electrospinning PLGA fibers on both sides of the nanoES and subsequent folding of the hybrid structure, highlights the intimate contact between nanoES mesh and PLGA fibers. The hybrid nanoES/biomaterial 3D scaffolds retain the original nanowire FET device characteristics. For example, measurements in 1×PBS solution showed that $\Delta G/G$ and $\Delta S/S$ were less than ± 9 % for mesh nanoES/PLGA composite versus bare nanoES. Hybrid nanoES were stable under cell culture conditions. For example, nanowire FET devices in the hybrid reticular nanoES/Matrigel^{TM} scaffold in neuron culture media (**Fig. 4-12d**) had $\Delta S/S < \pm$ 11% over a 9 week period, suggesting a capability for long-term culture and monitoring with the nanoES. These results show that nanoES can be combined with conventional biomaterials to produce hybrid scaffolds that now provide nanoscale electrical sensory components distributed in 3D.

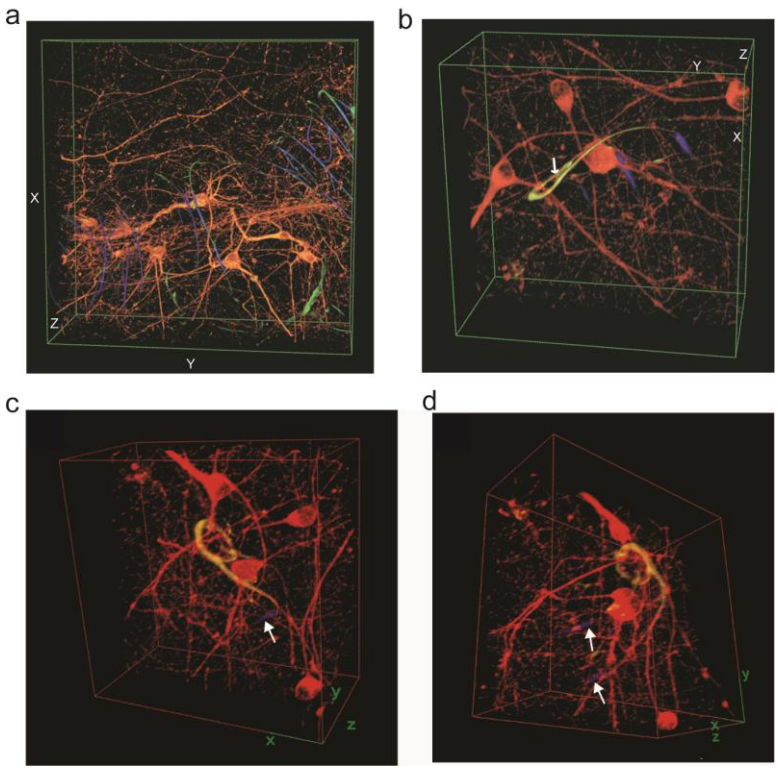

Figure 4-13 3D reconstructed confocal fluorescence image of rat hippocampal neurons within a reticular nanoES. (**a, b**), 3D reconstructed confocal images of rat hippocampal neurons after 2 week culture in Matrigel™ on reticular nanoES. Red (Alexa Fluor® 546): neuronal β-tubulin, yellow (rhodamine 6G): epoxy ribbons. The metal interconnects are false-colored in blue, and are imaged in reflected light mode. White arrow highlights a neurite passing through a ring-like structure supporting a nanowire FET. Dimensions in (**a**), x: 317 μm; y: 317 μm; z: 100 μm; in (**b**), x: 127 μm; y: 127 μm; z: 68 μm. (**c, d**), The images were rotated from the view shown in (**b**) approximately as follows: (left image) 90º about z-axis, -10º about y-axis; (right image) 90º about z-axis, 100º about y-axis, 40º about x-axis. Together, these images show unambiguously that neurites pass through the ring-like structures supporting individual nanowire FETs.

4.3.4 Characterization of nanoES/tissue interface

The hybrid nanoES were evaluated in 3D culture[29, 30] for several cell types. Embryonic rat hippocampal neurons were cultured in the reticular nanoES/Matrigel™ for 7-21 days (**Fig. 4-2**). Reconstructed 3D confocal microscopy images from a 2-week culture (**Fig. 4-13**) showed neurons with a high density of spatially interconnected neurites that penetrated the reticular nanoES (**Fig. 4-13a**), often passing through the ring

structures supporting individual nanowire FETs (**Fig. 4-13b-d**). Notably, the widths of the scaffold elements (passivated metal interconnects and structural ribbons) were similar to those of the neurite projections, demonstrating the combination of electronics with biological systems at an unprecedented similarity in scale.

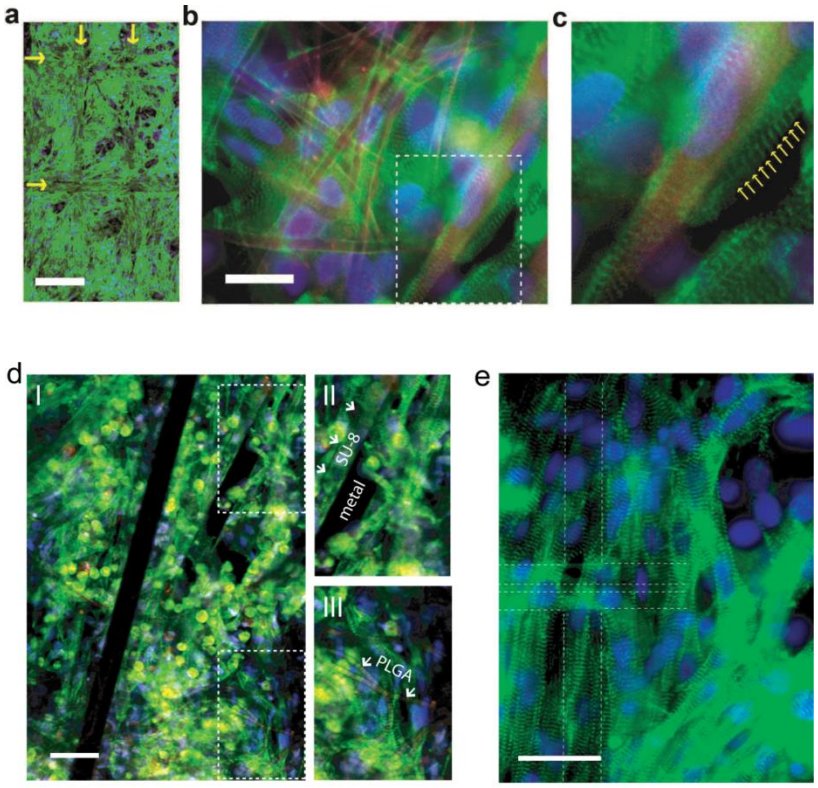

Figure 4-14 Fluorescence images of cardiac cell-seeded nanoES. Images showing α-actinin of cardiomyocytes (green in **a-e**, Alexa Fluor® 488), cell nuclei (blue in a-e, Hoechst 34580) and PLGA fibers (red in b-d, rhodamine 6G). Dense cardiomyocyte growth was supported by both nanoES (marked by yellow arrows in (**a**) and electrospun PLGA fibers in hybrid PLGA/nanoES in (**b**). **c**, is a zoomed view of the rectangular box in (**b**), showing (yellow arrows) striated patterns of α-actinin (green). **d**, Confocal fluorescence images of synthetic cardiac patch. II and III, zoomed-in view of the upper and lower dashed regions in I, showing metal interconnects, SU-8 scaffold (arrows in II), electrospun PLGA fibers (arrows in III). **e**, Epi-fluorescence image of the surface of the cardiac patch. Green (Alexa Fluor® 488): α-actinin, blue (Hoechst 34580): cell nuclei. The position of the source-drain electrodes is outlined with dashed lines. Scale bar, 200 μm (**a**), 20 μm (**b**), 40 μm (**d**) and 40 μm(**e**).

3D nanoelectronic cardiac culture was achieved from hybrid mesh nanoES/PLGA scaffolds (**Fig. 4-13**). Confocal fluorescence microscopy of a cardiac 3D culture (**Fig. 4-13b-d**) revealed a high density of cardiomyocytes in close contact with nanoES components. Epi-fluorescence images of cardiac cells on the surface of the nanoES cardiac patch showed striations characteristic of cardiac tissue[30, 38] (**Fig. 4-13e**). In addition, the *in vitro* cytotoxicity of nanoES in 3D neural and cardiac culture was evaluated (**Fig. 4-15**). Differences between hippocampal neurons in reticular nanoES/Matrigel™ versus Matrigel™ over 21 days, assessed with a standard live/dead cell assay[29] (**Fig. 4-15a**), and between cardiac cells in hybrid mesh nanoES/Matrigel™/PLGA and Matrigel™/PLGA from 2 to 12 days, measured with a metabolic activity assay (**Fig. 4-15b**) were minimal. These studies show that on 2-3 week time scale, the nanoES component of the scaffolds has little effect on cell viability, and thus could be exploited for a number of *in vitro* studies, including drug screening assays with these synthetic neural and cardiac tissues. Extended studies will be needed to evaluate the nanoES for longer-term implants, although the major component of nanoES, SU-8, has demonstrated long-term chronic biocompatibility suitable for *in vivo* recording[42, 43].

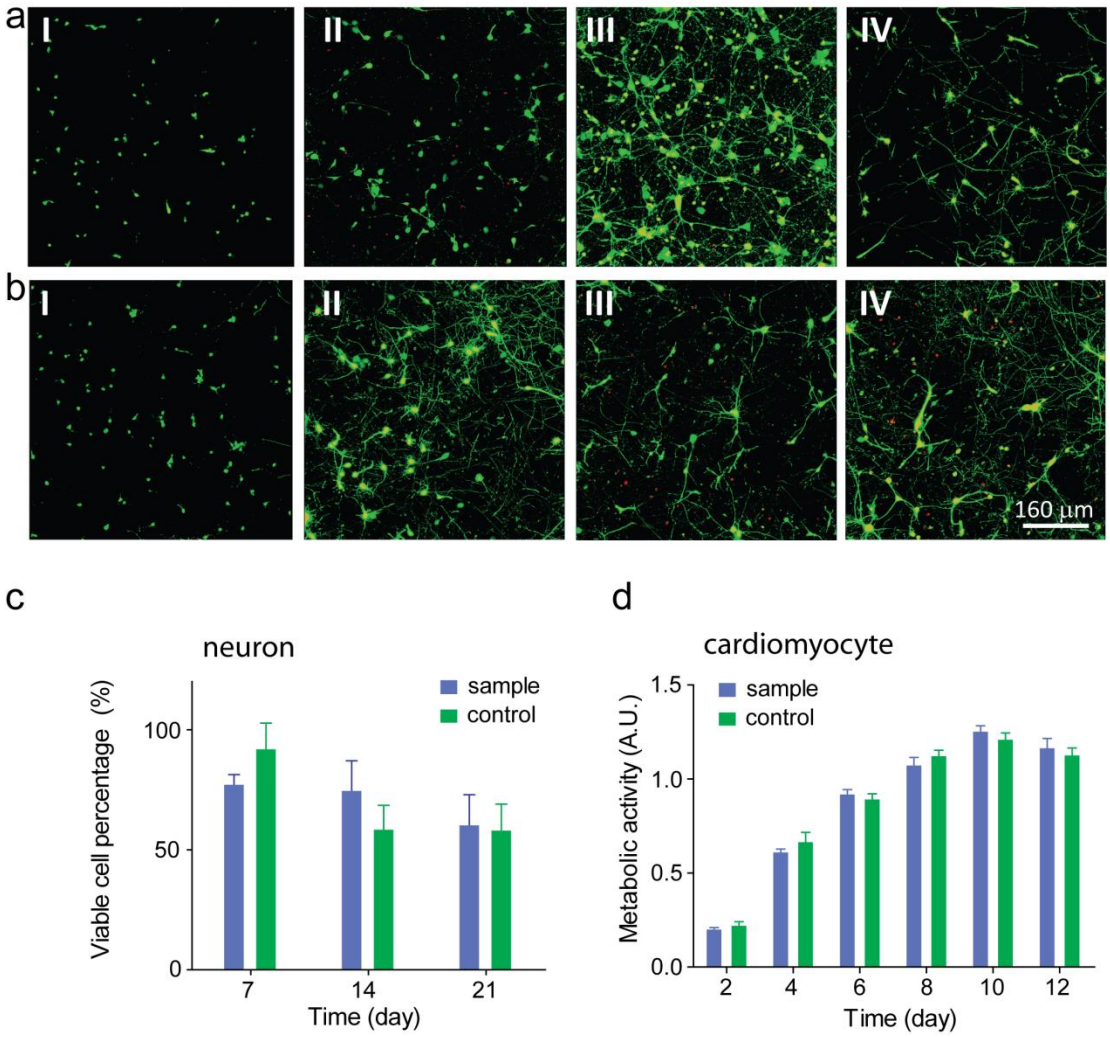

Figure 4-15 Biocompatibility test. 50-um projection confocal fluorescence images of neuron culture in MatrigelTM (**a**) vs nanoES/MatrigelTM (**b**). Neurons were labeled by LIVE/DEAD cytotoxicity assay after 0 days (**I**), 7 days (**II**), 14 days (**III**) and 21 days (**IV**) culture. **c**, Percentage of viable hippocampal neurons cultured in nanoES/Matrigel^{TM} *vs* Matrigel^{TM}. Cell viability was evaluated with LIVE/DEAD cytotoxicity assay from (**a, b**). Cells were counted from 3D reconstructed confocal fluorescence photomicrographs. n = 6; data are means ± SD. Differences between groups were very small although statistically significant ($p < 0.05$). **d**, MTS cytotoxicity assay of cardiomyocytes evaluated using the MTS assay. n = 6; data are means ± SD. Differences between groups were very small although statistically significant ($p < 0.05$).

4.3.5 Monitoring of cellular activity and microenvironment and its change due to external stimulations

The monitoring capabilities of the nanoES were first demonstrated in a 3D cardiomyocyte mesh construct (**Fig. 4-16a**). Output recorded from a single nanowire FET ~ 200 μm below the construct surface showed regularly spaced spikes with a frequency of ~1 Hz, a calibrated potential change of ~2 to 3 mV, a S/N ratio ≥ 3, and ~ 2 ms width. The peak amplitude, shape, and width are consistent with extracellular recordings from cardiomyocytes[20]. The potential of the nanoES based 3D cardiac culture to monitor appropriate pharmacological response was investigated by dosing the 3D cardiomyocyte mesh construct with norepinephrine, a drug that stimulates cardiac contraction via β_1-adrenergic receptors[44]. Measurements from the same nanowire FET device showed a twofold increase in contraction frequency following drug application. Interestingly, recording from two nanowire FETs from the cardiac patch upon norepinephrine application showed sub-millisecond and millisecond level, heterogeneous cellular responses to the drug (**Fig. 4-16a-c**). Additionally, simultaneous recordings from 4 nanowire FETs with separations up to 6.8 mm in a nanoES/cardiac construct (**Fig. 4-16d**) demonstrated multiplexed sensing of a coherently beating cardiac patch, with sub-millisecond time resolution. Our current device design yields relatively sparse device distribution with 60 devices over a ca. 3.5 × 1.5 cm^2 area. Increases in nanowire FET density, the use of cross-bar circuits and implementing multiplexing/demultiplexing for addressing[40], could allow the nanoES scaffolds to map cardiac and other synthetic tissue electrical activities over the entire constructs at high-density in 3D.

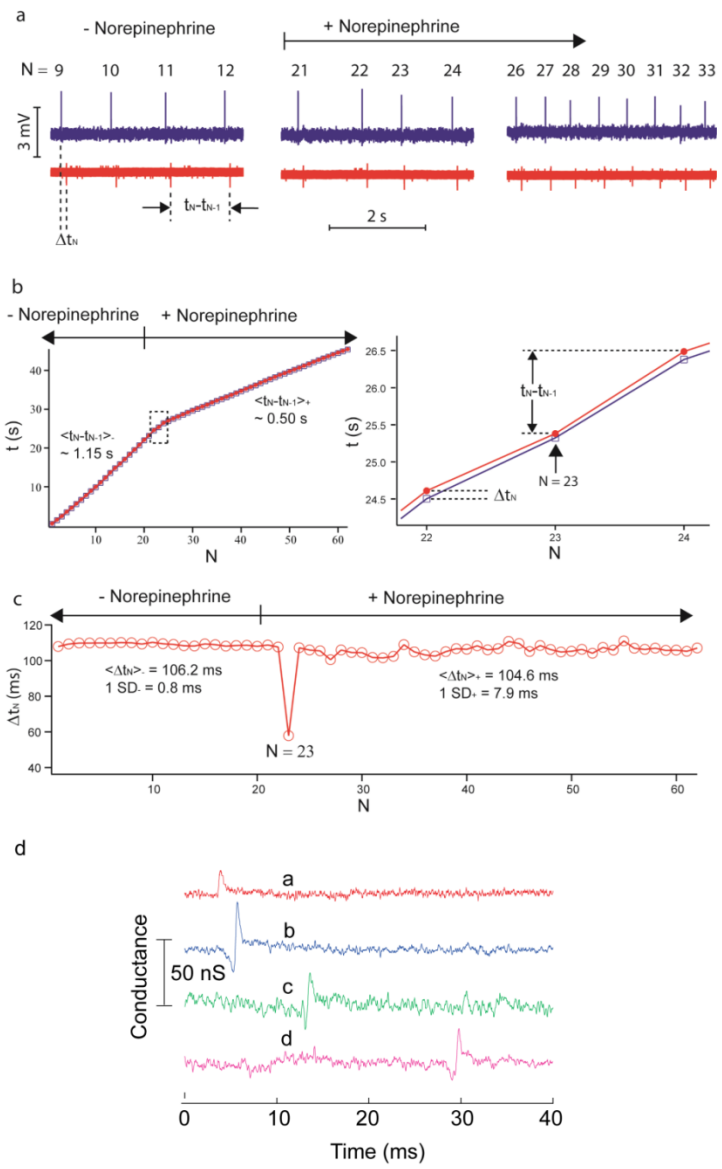

Figure 4-16 Multiplexed electrical recording can show cellular heterogeneity in drug response. a, Electrical recording traces from two devices in a cardiac patch, before (left), during (middle) and after (right) Norepinephrine application. Δt_N is the temporal difference between a pair of spikes from two devices. t_N-t_{N-1} is the interval between consecutive spikes from a single device. N is the spike index. **b**, The time (t) versus spike index (N) plot, showing a change in slope after norepinephrine application. The slopes correspond to the $< t_N$-$t_{N-1} >$, and are 1.15 s and 0.50 s before and after drug application, respectively. The color coding for devices is the same as in (**a**). The data show that the cells exhibit overall coherent beating and response to the drug. The right panel is the zoom-in view of the transition, where the middle point (N=23) shows a decreased Δt_N compared to earlier and later spikes. **c**, The Δt_N versus N plot. $< \Delta t_N >$ and 1 SD (standard deviation) before (-) and after (+) norepinephrine application show that although the drug has minimum effect on $< \Delta t_N >$, the sub-millisecond and millisecond

(Continued) fluctuations of Δt_N (1 SD) increase by ~ 10 fold following drug addition. Such stochastic variation suggests millisecond-level, heterogeneous cellular responses to the drug. **d**, Multiplex electrical recording of extracellular field potentials from 4 nanowire FETs (**a-d**) in a mesh nanoES.

Last, multiplexing measurements made with a reticular nanoES/neural construct (Fig. 4-17) showed that the 3D response of glutamate activation could be monitored. Together these experiments suggest nanoES constructs can monitor *in-vitro* the response to drugs from 3D tissue models, and thus have potential as a platform for *in-vitro* pharmacological studies[9,10].

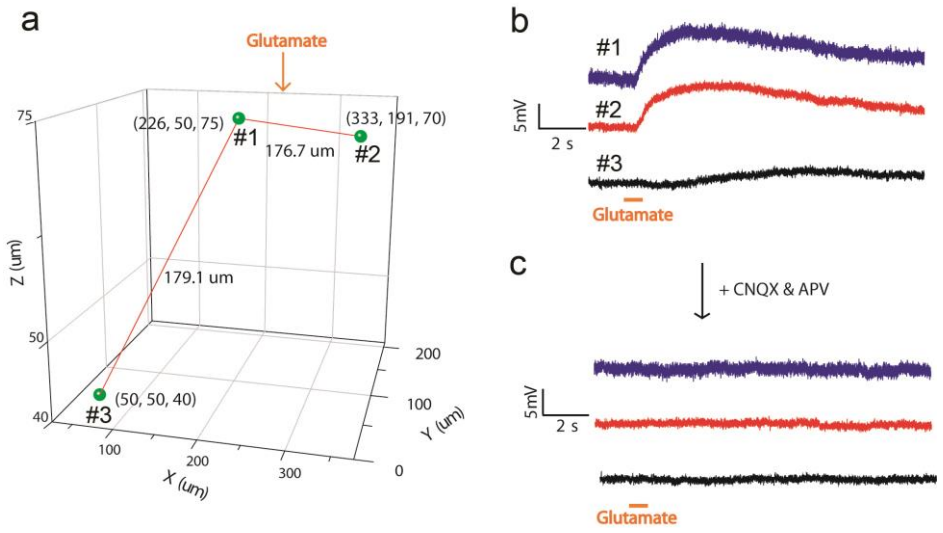

Figure 4-17 Multiplexed 3D recording from hybrid reticular nanoES/neural constructs. The hybrid nanoES/neural 3D construct was prepared by culturing neurons with a 3D reticular device array for 14 days in vitro with a density of > 4 million neurons/mL in Matrigel™. During recording, the nanoES/neural hybrid was perfused with an oxygenated artificial CSF (aCSF) containing (in mM) 119 NaCl, 2.5 KCl, 2.5 $CaCl_2$, 1.3 $MgSO_4$, 1 NaH_2PO_4, 26.2 $NaHCO_3$, 22 glucose and equilibrated with 95% O_2/5% CO_2. Three nanowire FETs (labeled 1, 2 and 3) were distributed in the construct with x-y-z positions shown in (**a**). The total sample thickness was ~ 100 µm. The red lines indicate the distances between two devices in 3D. Sodium Glutamate (Sigma) was dissolved in saline solution and further diluted to 20 mM in aCSF solution. Glutamate solution was injected (Micro-injector, Harvard Apparatus) in the middle above device 1 and 2 (orange arrow). The injection pulse duration is 0.5 s. **b**, The local field potential changes recorded from three devices in the 3D neuron construct showed distinct position-dependent temporal responses following glutamate solution injection. **c**, Perfusing 6-cyano-7-nitroquinoxaline-2,3-dione (CNQX) and D(-)-2-Amino-5-phosphonopentanoic acid (APV) blockers prior to glutamate addition eliminate any observed response, and thus show that the observed response in (**b**) can be attributed to postsynaptic signal propagation. The orange segments mark the timing when glutamate solution was injected

(Continued) (**b, c**).The observed responses are consistent with the effects of glutamate, CNQX and APV.

We have also extended our approach towards development of artificial tissue with embedded nanoelectronic sensory capabilities. Specifically, vascular nanoES constructs were prepared by processes analogous to those used for tissue engineered autologous blood vessels[31, 45] except the addition of the nanoES (**Fig. 4-18a**). Human aortic smooth muscle cells (HASMCs) were cultured on 2D mesh nanoES with sodium ascorbate to promote deposition of natural ECM. The hybrid nanoES/HASMC sheets (**Fig. 4-18b**) were rolled into multi-layer 3D tubular structures and matured without macroscopic delamination or desquamation (**Fig. 4-18c**), and analyses showed that the cells expressed smooth muscle α-actin (**Fig. 4-18d**), the key contractile protein in smooth muscle[31].

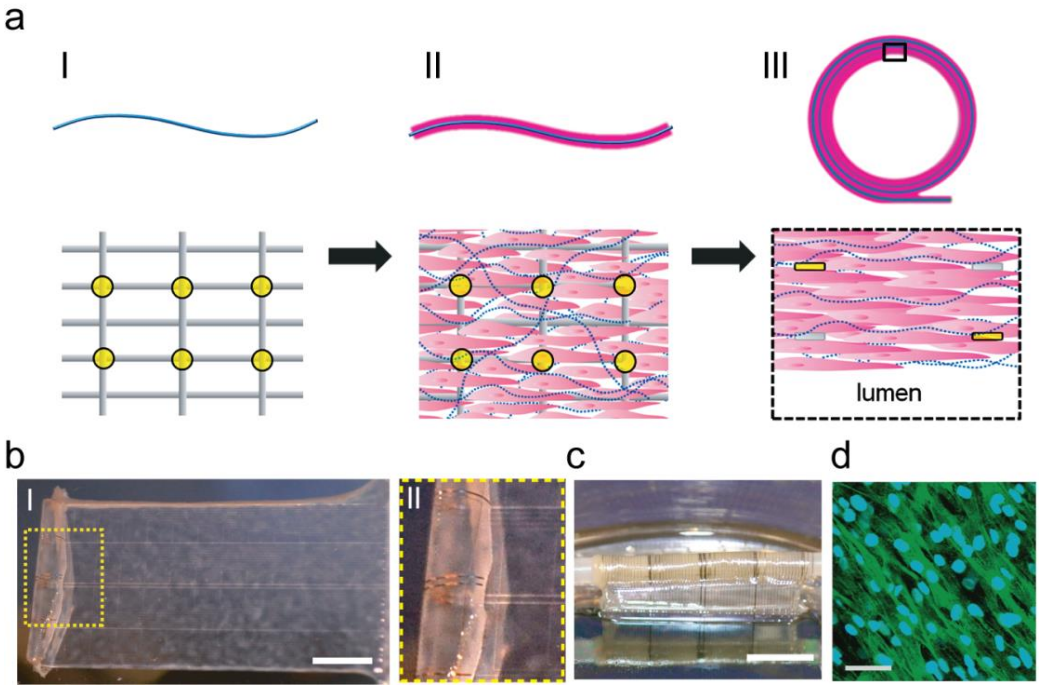

Figure 4-18 Synthetic vascular construct by mesh nanoES. a, Schematic of the synthesis of smooth muscle nanoES. The upper panels are side views, while the lower ones are either top views (**I** and **II**) or zoom-in view (**III**). Grey: mesh nanoES, blue fibers: collagenous matrix secreted by HASMC, yellow dots: nanowire FETs, pink: HASMC. **b**, **I**. Photograph of a single HASMC sheet cultured with sodium L-ascorbate

(Continued) on a nanoES. **II**. Zoomed-in view of the dashed area in (**I**), showing metallic interconnects macroscopically integrated with cellular sheet. **c**, Photograph of the vascular construct after rolling into a tube and maturation in a culture chamber for 3 weeks. **d**, Confocal fluorescence microscopy image from the surface of the HASMC/mesh-like nanoelectronics biomaterial shows α-actin (green, Alexa Fluor® 488) and cell nuclei (blue, Hoechst 34580) in smooth muscle cells. Local alignment of HASMCs is revealed by anisotropy in α-actin fibers running from upper left to lower right of image. Scale bars, 40 μm.

The distribution of nanoES in the tubular construct was visualized by micro-computed tomography (μCT). A projection of the reconstructed 3D μCT data (**Fig. 4-19a**) revealed regularly spaced metal interconnects with at least four revolutions (arrows, **Fig. 4-19a, II**), consistent with the nanowire FET mesh and tissue rolling. Analyses of hematoxylin-eosin-stained sections (**Fig. 4-19b**) revealed smooth muscle tissue ~ 200 μm thick, with elongated cells and collagenous nanofibers, and embedded SU-8 ribbons from the nanoES (**Fig. 4-19b**). These findings confirm 3D integration of nanowire FET nanoelectronics with healthy smooth muscle.

The potential of this vascular construct to function as a biomedical device was demonstrated by 3D pH sensing (**Fig. 4-19c,** inset). As the extravascular pH was varied stepwise with luminal pH fixed, simultaneous recordings from nanowire FETs in the outermost layer showed stepwise conductance decreases with a sensitivity of ~32 mV/pH. Nanowire FETs in the innermost layer (closest to luminal) showed minor baseline fluctuations. This ability to resolve extravascular pH changes makes possible detection of inflammation, ischemia, tumor microenvironments or other forms of metabolic acidosis due to overproduction of organic acids or impaired renal acidification[46, 47], although we stress that implantation of these nanoES based vascular and other nanoES-embedded constructs for *in-vivo* studies will require substantial future work.

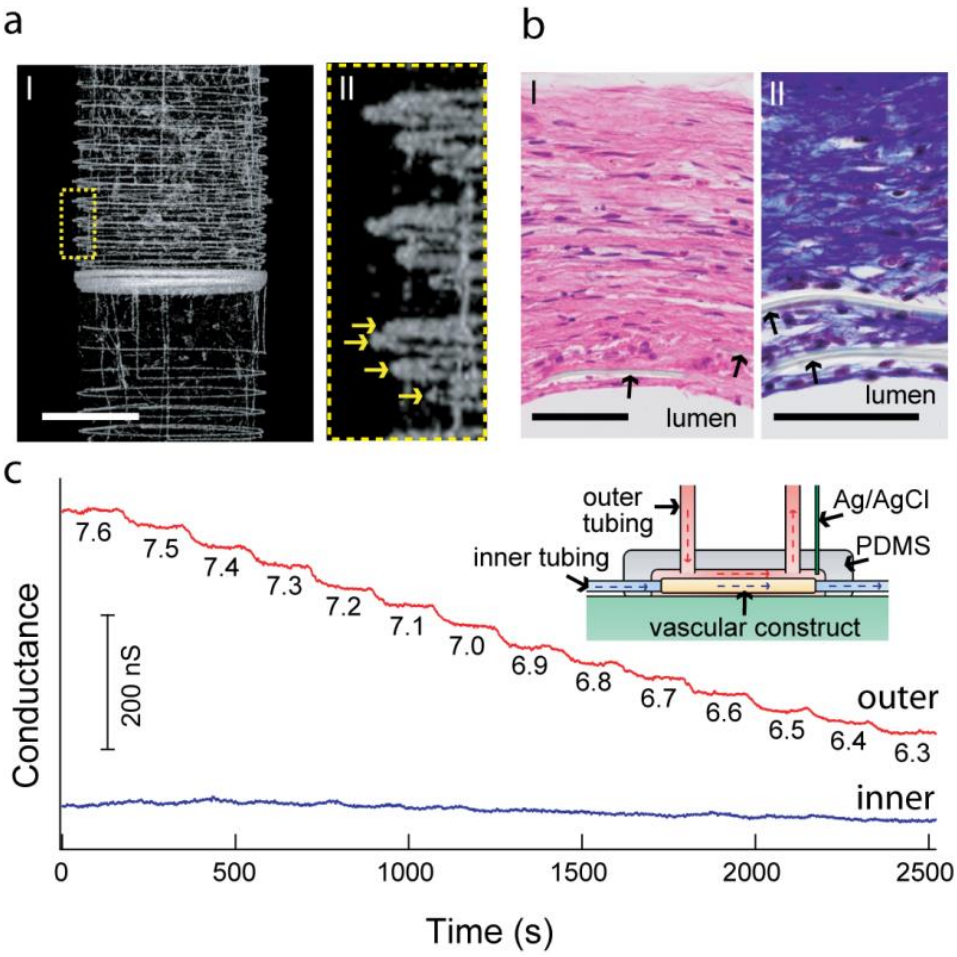

Figure 4-19 Synthetic vascular construct enabled for sensing. a, **I**. Micro-computed tomograph of a tubular construct segment. **II**. Zoomed-in view of (**I**). Arrows mark the individual nanowire FET-containing layers of the rolled construct. Scale bar, 1 mm. **b**, Hematoxylin & eosin (**I**) and Masson Trichrome (**II**; collagen is blue) stained sections (~ 6 μm thick) cut perpendicular to the tube axis; lumen regions are labeled. Arrows mark the positions of SU-8 ribbons of the nanoES. Scale bars, 50 μm. **c**, Changes in conductance over time for two nanowire FET devices located in the outermost (red) and innermost (blue) layers. Inset: schematic of the experimental set-up. Outer tubing delivered bathing solutions with varying pH (red dashed lines and arrows); inner tubing delivered solutions fixed pH (blue dashed lines and arrows).

4.4 Conclusion

The nanoES concept and implementations described here represent a new direction in merging nanoelectronics with biological systems since we have demonstrated 3D macroporous material/device platform that is distinct from either engineered tissue[6, 48]

or flexible electronics[13-17, 49-51]. Looking forward, there are several areas to develop. Cell interactions with nanoES could be tuned by modification of the nanoES with growth determinants[6, 30]. In addition, the elements in the nanoES could be expanded to incorporate nanoscale stimulators and stretchable designs to provide electrical and mechanical stimulation to enhance cell culture.

4.5 Bibliography

1. Na, K. *et al. Science* **333**, 328-332 (2011).

2. Schaedler, T. A. *et al. Science* **334**, 962-965 (2011).

3. Place, E. S., George, J. H., Williams, C. K. & Stevens, M. M. *Chem. Soc. Rev.* **38**, 1139 (2009).

4. Wylie, R. G., Ahsan, S., Aizawa, Y., Maxwell, K. L., Morshead, C. M. & Shoichet, M. S. *Nat. Mater.* **10**, 799 (2011).

5. Kloxin, A. M., Kasko, A. M., Salinas, C. N. & Anseth, K. S. *Science* **324**, 59 (2009).

6. Dvir, T., Timko, B. P., Kohane, D. S. & Langer, R. *Nat. Nanotechnol.* **6**, 13 (2011).

7. Kraehenbuehl, T. P., Langer, R. & Ferreira, L. *Nat. Meth.* **8**, 731 (2011).

8. Hutmacher, D. W. *Nat. Mater.* **9**, 90 (2010).

9. Huh, D. *et al. Science* **328**, 1662 (2010).

10. Baker, M. *Nature* **471**, 661 (2011).

11. Schwille, P. *Science* **333**, 1252 (2011).

12. Ruder, W. C., Lu, T. & Collins, J. J. *Science* **333**, 1248 (2011).

13. Timko, B. P. *et al. Nano Lett.* **9**, 914 (2009).

14. Viventi, J. *et al. Transl. Med.* **2**, 24ra22 (2010).

15. Kim, D. H. *et al. Nature Mater.* **10**, 316 (2011).

16. Viventi, J. *et al. Nature Neurosci.* **14**, 1599 (2011).

17. Kim, D. H. *et al.* Epidermal electronics. *Science* **333**, 838 (2011).

18. Tian, B., Cohen-Karni, T., Qing, Q., Duan, X., Xie, P. & Lieber C. M. *Science* **329**, 831 (2010).

19. Qing, Q. *et al. Proc. Natl. Acad. Sci. USA* **107**, 1882 (2010).

20. Cohen-Karni, T., Timko, B. P., Weiss, L. E. & Lieber, C. M. *Proc. Natl. Acad. Sci. USA* **106**, 7309 (2009).

21. Timko, B. P., Cohen-Karni, T., Qing, Q., Tian, B. & Lieber, C. M. *IEEE Trans. Nanotechnol.* **9**, 269 (2010).

22. Prohaska, O. J., Olcaytug, F., Pfundner, P. & Dragaun, H. *IEEE T Bio-Med Eng, BME* **33**, 223 (1986).

23. Methods for Neural Ensemble Recordings. 2nd edition. Editor, Nicolelis, M. A. L. Boca Raton (FL), CRC Press, 2008.

24. McKnight, T. E. *et al. J. Phys. Chem. B* **110**, 15317 (2006).

25. Yu, Z. *et al. Nano Lett.* **7**, 2188 (2007).

26. Aviss, K. J., Gough, J. E. & Downes, S. *Euro. Cells Mater*. **19**, 193 (2010).

27. S. Timoshenko, S. Woinowsky-Krieger, Theory of Plates and Shells, 2nd edition, P4-6, McGraw-Hill Inc., 1959.

28. *http://www.genlantis.com/objects/catalog/product/extras/1285_N100200_NeuroPure_E18_Hippocampal_Cells_MV25April2007.pdfS8.*

29. Xu, T., Molnar, P., Gregory, C., Das, M., Boland, T. & Hickman, J. J. *Biomaterials* **30**, 4377 (2009).

30. Sapir, Y., Kryukov, O. & Cohen, S. *Biomaterials* **32**, 1838 (2011).

31. L'Heureux, N., Pâquet, S., Labbé, R., Germain, L. & Auger, F. A. *FASEB J.* **12**, 47 (1998).

32. Pautot, S., Wyart, C. & Isacoff, E. Y. *Nat. Meth.* **5**, 735 (2008).

33. Kiernan, J. A. Histological and histochemical methods: theory and practice, 4th edition, Scion publishing Ltd, 2008.

34. *http://www.polysciences.com/SiteData/docs/872/4dfaddd3f92e8e02f9ac9638745201f1/ 872.pdf.*

35. Prabhakaran, M. P., Kai, D., Ghasemi-Mobarakeh, L. & Ramakrishna, S. *Biomed. Mater.* **6**, 055001 (2011).

36. Dequach, J. A., Yuan, S. H., Goldstein, L. S. & Christman, K. L. *Tissue Eng. Part A* **17**, 2583 (2011).

37. Hanley, P. J., Young, A. A., LeGrice, I. J. Edgar, S. G. & Loiselle, D. S. *J. Physiol.* **517**, 831 (1999).

38. Engelmayr, G. C. Jr *et al. Nat. Mater.* **7**, 1003 (2008).

39. Lu, W. & Lieber, C. M. *Nat. Mater.* **6**, 841 (2007).

40. Yan, H. *et al. Nature* **470**, 240 (2011).

41. Wang, M. F., Maleki, T. & Ziaie, B. *IEEE/ASME J. Microelectromech. Systems* **17**, 882 (2008).

42. Cho, S. H. *et al. IEEE Sensors J.* **8**, 1830 (2008).

43. Voskerician, G. *et al. Biomaterials* **24**, 1959 (2003).

44. Zipes, D. P. & Jalife, J. Cardiac electrophysiology: from cell to bedside, 5th edition (Saunders, Philadelphia, PA, 2009).

45. L'Heureux N. *et al. Nat. Med.* **12**, 361 (2006).

46. Neri, D. & Supuran, C. T. *Nat. Rev. Drug Discov.* **10**, 767 (2011).

47. Kraut J. A. & Madias, N. E. *Nat. Rev. Nephrol.*, **6**, 274 (2010).

48. Dvir, T. *et al. Nat. Nanotechnol.* **6**, 720 (2011).

49. Sekitani, T. *et al. Science* **321**, 1468 (2008).

50. Mannsfeld, S. C. B. *et al. Nat. Mater.* **9**, 859 (2010).

51. Takei, K. *et al. Nat. Mater.* **9**, 821 (2010).

Chapter 5. Syringe Injectable Electronics

5.1 Introduction

With recent advancement in electronics fabrication[1-2], we have been able to fabricate electronics on flexible, stretchable and 3D substrates so that electronics can cover on soft or non-planar surfaces for monitoring and control, and making smart and portable systems[3-12]. New requirements have risen for implementing electronics into objects with minimal invasiveness, 3D distributing nano- and micro-scale sensor units with microscale spatio-resolution in a large volume and maintaining mechanically ultra-flexibility[13-14]. Some examples have shown that constructing 3D networks of the electronics with subsequently building a new object within these networks, however, these methods are not applicable to existing objects[8]. Also, one can use a substrate to deliver electronics into other samples with releasing electronics from that substrate; however, these methods still introduce large pieces of solid materials for delivering, which preclude the integration of sensing units into a large volume with minimal invasiveness[13], which leads to, normally, when introducing electronic units into a large volume, same size damage is necessary. On the contrary, the development of soft materials (gel, fibers, etc.)[15-16] and freestanding nano- or bio-materials (microbeads, viral vectors, etc)[17-18] brings many examples in which materials can be syringe-injected/delivered with vanishingly little invasiveness into a much larger target system followed by fully integration into the target system.

Here we introduce a new strategy for electronics design to meet those requirements. This strategy involves encapsulating electronics units into a mesh polymeric network that mimics the structure of soft materials and freestanding nanomaterials, delivering these electronics into target system via syringe-injection and making injected electronics self-restoring their geometric configuration. In this study, silicon nanowires[19-20] were used as semiconductor components and metal electrodes[21] were used as electrical sensing units given their nano- and micro-scale structure, multifunctionalities and electrical and chemical recording capability.

5.2 Experimental

5.2.1 Nanowire synthesis

Single-crystalline nanowires were synthesized using the Au nanocluster-catalyzed vapor-liquid-solid growth mechanism in a home-built CVD system described previously[22]. Au nanoclusters (Ted Pella Inc. Redding, CA) with 30 nm diameters were dispersed on the oxide surface of silicon/SiO_2 substrates (600 nm oxides, n-type 0.005V.cm, Nova Electronic Materials, Flower Mound, TX) and placed in the central region of a quartz tube CVD reactor system. Uniform 30-nm p-type silicon nanowires were synthesized using reported methods[22]. In a typical synthesis, the total pressure was 40 torr, and the flow rates of SiH_4, diborane (B_2H_6, 100 ppm in H_2), and hydrogen (H_2, semiconductor grade) were 2, 2.5, and 60 SCCM, respectively. The silicon-boron feed-in ratio was 4,000:1, and the total nanowire growth time was 30 - 60 min.

5.2.2 Freestanding syringe injectable electronics fabrication

Key steps used in the fabrication of the syringe injectable electronics were as follows[14]: (1) Thermal deposition were used to deposit a 100-nm nickel metal layer over the whole silicon wafer (600-nm SiO_2 or 100-nm SiO_2/200-nm Si_3N_4, n-type 0.005V.cm, Nova Electronic Materials, Flower Mound, TX), where the nickel served as the final relief layer for freestanding electronics. (2) A 300- to 400-nm layer of SU-8 photoresist (2000.5; MicroChem Corp., Newton, MA) was spin cast (3000 rmp) over the entire chip followed by prebaking at 65 °C and 95 °C for 2 and 4 min, respectively. (3) Photolithography was used to pattern the bottom SU-8 layer for passivating and supporting the whole device structure. After postbaking (65 °C and 95 °C for 2 and 4 min, respectively), SU-8 developer (MicroChem Corp., Newton, MA) was used to develop the SU-8 pattern. Those areas exposed to UV light became indissoluble to SU-8 developer, and other areas were dissolved by SU-8 developer. The SU-8 patterns were cured at 180 °C for 20 min. (4) A 300- to 400-nm layer of SU-8 photoresist was spin cast (3000 rmp) over the entire chip, followed by prebaking at 65 °C and 95 °C for 2 and 4 min, respectively, then (5) the synthesized nanowires were directly printed from growth wafer over the SU-8 layer by the contact printing. Photolithography was used to define regular patterns on the SU-8. After postbaking (65 °C and 95 °C for 2 and 4 min, respectively), SU-8 developer (MicroChem Corp., Newton, MA) was used to develop the SU-8 pattern. Those nanowires on the non-exposed area were removed by further washing away in isopropanol solution 30 s for twice leaving those selected nanowires patterned on the regular patterns of SU-8 structure. The SU-8 patterns were cured at 180 °C for 20 min. (6) To fabricate metal electrode electrophysiological sensor, photolithography and electron beam deposition were used to define and deposit 20 x 20

μm^2 Pt pad. (7) Photolithography and thermal deposition were used to define and deposit the metal contact to address each nanowire device and form interconnections to the input/output pads for the array. For the general metal contact region, in which the metal is nonstressed, symmetrical Cr/Au/Cr (1.5/50–80/1.5 nm) metal was sequentially deposited followed by metal liftoff in acetone. For device region in which the metal is nonstressed, symmetrical Cr/Pd/Cr (1.5/50–80/1.5 nm) metal was sequentially deposited followed by metal liftoff in acetone. For device region in which metal is stressed for organizing into 3D structure, nonsymmetrical Cr/Pd/Cr (1.5/50-80/50-80 nm) metal was sequentially deposited followed by metal liftoff in acetone. (8) A 300- to 400-nm layer of SU-8 photoresist was spin cast (3000 rmp) over the entire chip, followed by prebaking at 65 °C and 95 °C for 2 and 4 min, respectively. Then lithography was used to pattern the top SU-8 layer for passivating the whole device structure. The structure was post-baked, developed, and cured by the same procedure as described above. (9) A 300- and 500-nm thick layers of LOR 3A and S1805 (MicroChem Corp., Newton, MA) photoresist can be deposited by spin-coating and defined by photolithography to further protect the device region if necessary[23]. (10) The 2D syringe injectable electronics were released from the substrate by etching of the nickel layer (Nickel Etchant TFB, Transene Company Inc.) for 3 - 4 hours at 25 °C. (11) If the device region was protected by photoresist protection layer, electronics need to be transferred into deionized (DI) water for rinsing and then dried on substrate, exposed in ultraviolet light (430 nm, 120 s) to sensitize the photoresist protection with subsequently immersed in developer solution (MF-CD-26, MicroChem Corp., Newton, MA) to dissolve the protection on device region. The structure of the mesh electronics is in **Figure 5-1**.

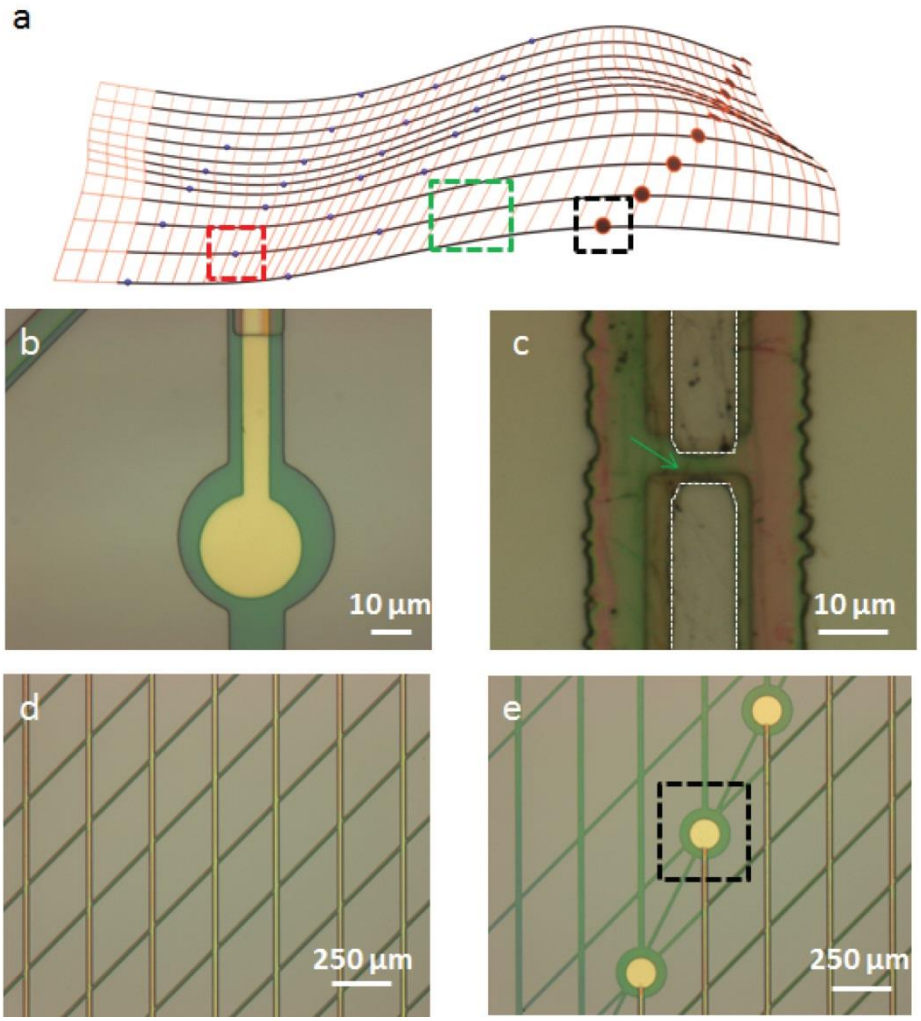

Figure 5-1 Optical images of electronics structure. a, Schematics of injectable electronics. Black, metal contact and I/O pads; orange, supporting polymer and blue, device. **b**, optical image of passive metal electrode. **c**, optical image of nanowire FET (indicated by green arrow) device. Source-drain electrodes are highlighted by white dashed lines. **d**. Optical image of mesh region on the mesh corresponds to green dashed box in (**a**). **d** and **e**, Optical image of I/O pads corresponds to black dashed box in (**a**).

5.2.3 Structure characterization

Scanning electron microscopy (SEM, Zeiss Ultra55/Supra55VP field-emission SEMs) was used to characterize the structure of electronics. Bright-field and dark-field optical micrographs of samples were acquired on an Olympus FV1000 system using FSX-BSW software (ver. 02.02). Fluorescence images were obtained by doping the SU-8

resist solution with Rhodamine 6G (Sigma-Aldrich Corp., St. Louis, MO) at a concentration less than 1 μg/mL before deposition and patterning by Olympus FSX100 confocal microscopy system. *ImageJ* (ver. 1.45i, Wayne Rasband, National Institutes of Health, USA) was used for 3D reconstruction and analysis of the confocal and epi-fluorescence images.

5.2.4 Surface modification of electronics for syringe injectable

The freestanding electronics was transferred into DI water by glass pipette to remove nickel etchant or developer solution. Then the electronics was transferred and soaked into poly-D-lysine (PDL, 0.5-1.0 mg/mL, MW 70,000 – 150,000, Sigma-Aldrich Corp., St. Louis, MO) aqueous solution for 2 - 12 hours at 25 °C for surface modification. After surface modification, electronics was transferred into PBS (HyClone™ Phosphate Buffered Saline, Thermo Fisher Scientific Inc., Pittsburgh, PA) buffer solution for future use.

5.2.5 Mesh structure design

5.2.5.1 General tilted mesh electronics

Design of mesh structure is illustrated in **Figure 5-2**. We call the ribbon along the injection direction as the longitudinal ribbon and call the ribbon perpendicular to the injection direction as the transverse ribbon. Transverse ribbons are tilted 45° counterclockwise to transverse direction on the mesh plane forming 45° angle to longitudinal ribbons. Metal contacts are mainly encapsulated in longitudinal ribbons. For active electronics, some transverse ribbons also contain metal contacts to form the S/D electrodes of FET. For passive metal electrode electronics, only longitudinal ribbons

contain metal contacts. Silicon nanowire devices and passive metal electrodes are patterned either on the longitudinal ribbons in the center of unit cells or patterned separately in a beam in the longitudinal direction on the transverse ribbons in the center of unit cells to reduce strains for device during injection. For the ribbons containing metal contact lines, 100-nm thick metal lines are encapsulated in the middle of two 350-nm thick SU-8 layers. For the ribbons without metal contact lines, the total SU-8 thickness is 700-nm. Transverse ribbons and longitudinal ribbons together form mesh with periodic unit cells. The dimensions of all unit cells are identical across the whole mesh. Design #1 is used for injection by needle with inner diameter larger than 200 μm. The width of mesh is 5 – 15 mm. The length of unit cell is 333 μm and width of unit cell is 250 μm. All the SU-8 layers are 20 μm in width and all the metal layers are 10 μm in width. Design #2 is used for injection by needle with inner diameter smaller than 200 μm. The width of mesh is 2 – 5 mm. The length of unit cell is 333 μm and width of unit cell is 250 μm. SU-8 layers in longitudinal ribbons are 20 μm in width and SU-8 layers in transverse ribbons are 5 – 10 μm in width. Metal layers in longitudinal ribbons are 10 μm in width and metal layers in transverse ribbons are 2 – 5 μm in width.

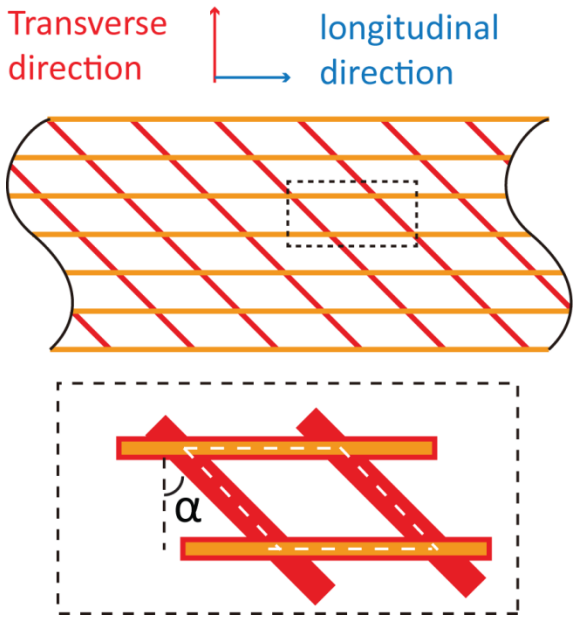

Figure 5-2 Schematics of mesh design. Schematics show the structures of 2 different mesh designs. Black dashed boxes highlight the unit cell structure. Red, supporting and passivation polymer and yellow, metal lines.

5.2.5.2 Control orthogonal mesh electronics sample

The transverse ribbons are perpendicular to the longitudinal ribbons to form an orthogonal mesh with the same periodic unit cell structure. All metal line patterns, thickness and width of ribbons are the same as design #1 of tilted transverse ribbons electronics. The width of electronics is 5 – 15 mm for testing.

5.2.5.3 Control thin film electronics sample

The thickness of SU-8 is 700 nm. All the metal line patterns are the same as design #1 of tilted mesh electronics. The width of electronics is 0.1 – 5 mm.

5.2.6 Glass needle and fluidic channel preparation

Glass needle was prepared by using a conventional pipette puller (Model P-97, Sutter Instrument, CA) and glass tube (30-0057, Harvard Apparatus) following the parameters: Heat: Ramp + 25, Pull: 0, Velocity: 140, Time: 100 and Pressure: 200. For a

clean-cut needle with inner diameter from 20 – 200 μm, a ceramic tiles (#CTS, Sutter Instrument, CA) was used to score the glass tip checked by optical microscope with subsequent mechanical break.

For the channels used for imaging, the pulling is halted and suspended in the middle to not completely break the glass tube (VWR International, LLC, Radnor, PA). The channel size is characterized by confocal fluorescence imaging. Rodamine-6G (Sigma-Aldrich Corp., St. Louis, MO) solution is filled into the channel for imaging. For a channel inner diameter smaller than 300 μm, epoxy glue is used to increase stability of channel preventing channel broken during imaging.

5.2.7 Surface-to-volume-ratio calculation

The surface-to-volume-ratio of a ribbon or a film (length, l; width, w; height, h) is calculated as $2(lw+lh+wh)/lwh=2(1/h+1/w+1/l)$. For a typical thin film of 10um height, with much larger length and width, the surface-to-volume-ratio is ca. $2/h=0.2$ um^{-1}. For a typical ribbon (large length l) in our mesh structure with 5 um and 0.7 um in width and height respectively, the surface-to-volume-ratio is $\sim 2/h+2/w=3.25$ um^{-1}.

5.2.8 Injection by metal gauge needles

After surface modification, electronics was transferred into syringe (Pressure Control Glass Syringes, Cadence, Inc., Cranston, RI) with metal gauge needle (Veterinary Needles, Cadence, Inc., Cranston, RI) by glass pipette (Disposable Pasteur Pipets, Lime Glass, VWR International, LLC, Radnor, PA). It is very important to keep the orientation and unfolded structure of the electronics in the syringe to prevent any buckles. Press the syringe and allow the tip part of the electronics be loaded into the needle.

5.2.9 Injection by glass needle

After surface modification, electronics was transferred into syringe with metal gauge needle by glass pipette. It is very important to keep the orientation and unfolded structure of the electronics in the syringe to prevent any buckles. Syringe was connected to glass needle by plastic tubing. Press the syringe and allow the tip part of the electronics be loaded into the glass needle. To better control injection process, the microinjector (NPIPDES, ALA Scientific instruments Inc., Farmingdale, NY) and patch-clamp set-up (Axonpatch 200B, Molecular Devices, LLC, Sunnyvale, CA) were used for control the injection process. Electronics was directly loaded into the glass needle illustrated by **Figure 5-3** as following: (1) A plastic tube was connected to the tip end of glass needle and connected to a syringe. (2) Electronics was drawn in into the rear part of glass needle. It is very important to load the electronics from its sharp tip to facilitate the folding of electronics in the glass tube and keep an extended structure to prevent buckles. (3) The plastic tube was removed from glass needle and the needle was mounted onto patch-clamp set-up and connected to micro-injector or syringe for injection.

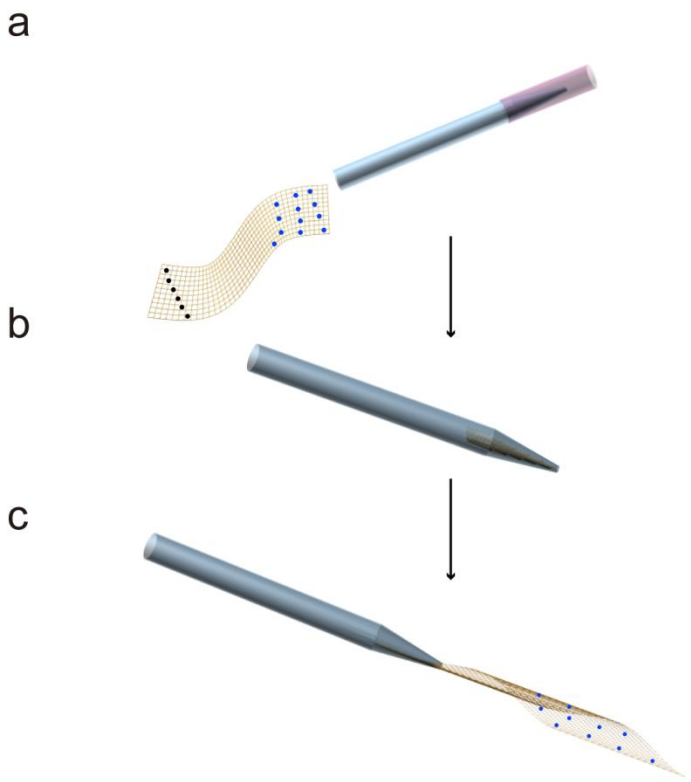

Figure 5-3 Loading in needle. Schematics show how the mesh electronics was stepwise loaded into glass needle. Blue, glass needle; pink, plastic tube; yellow, injectable electronics; black, I/O pads and blue, nanowire devices. **a**, the tip of glass needle was connected to syringe by plastic tube. Injectable electronics was sucked in from the end of glass needle. **b**, electronics was loaded into glass needle. **c**, glass needle was mounted to patch-clamp setup for injection.

5.2.10 Yield of injection

To obtain the yield of electronics after injection, conductance of nanowire devices before and after injection through needles was compared as following procedure: (1) As-made 2D electronics was partially immersed in etchant solution (Nickel Etchant TFB, Transene Company Inc., Danvers, MA) for 3 - 4 hours at 25 ºC to firstly release nickel layer under I/O region of electronics. Then, electronics was transferred to DI water and dried in ethanol, while the released I/O region was unfolded on the substrate. (2) After

electronics dried completely, the left nickel layer was etched in etchant solution for 1 - 2 hours at 25 °C, after which electronics would be transferred to DI water and dried in ethanol to allow active device region to be unfolded on the substrate. Because the I/O pads covering larger region than electronics, these two-step etching process reduce the etching time for active device region. (3) After completely dried, electronics adhered weakly on the wafer, which can be easily removed from the substrate afterwards. Conductance (G_0) for each device was measured by a probe station (Desert Cryogenics, Model 4156C) with back plane grounded. Current-voltage (*I*-*V*) data were recorded using an Agilent semiconductor parameter analyzer (Model 4156C) with contacts to device through probe station. Device with conductance above 100 nS were accounted as initial devices with total number N_0 in this stage. (4) After conductance measurement, electronics on substrate was immersed in DI water for 4 - 6 hours until it released from the substrate and fully suspended in the solution. (5) The electronics was transferred through glass pipette to PDL aqueous solution for surface modification as described above. (6) Electronics was loaded by glass pipette into syringe with gauge metal needle and injected through needle with different inner diameters (from 100 um to 600um) into a chamber with I/O part unfolded near the chamber on a substrate. (7) Ethanol was used to rinse and dry the I/O part. (8) Conductance (G_1) for each device was measured again with the same probe station under same condition, and the total number of survived devices with G_1 above 100 nS was N_1. Yield and conductance change were calculated as (N_1/N_0) and (G_1-G_0)/G_0, respectively.

5.2.11 ACF bonding process

After fabrication, electronics was injected through syringe into solution, soft matters, biomaterials or tissues, with I/O part injected outside the target materials. DI water and other solvents (PBS, culture medium, hexane, etc.) were introduced to facilitate unfolding the I/O region, after which the I/O region was rinsed and dried with ethanol (ethanol, 190 proof (95%), VWR International, LLC, Radnor, PA) (**Fig. 5-4**). For the connection to measurement setup, the unfolded and dried I/O region of injectable electronics was bonded to the flexible cable (FFC / FPC Jumper Cables PREMO-FLEX, Molex, Lisle, IL) through an anisotropic conductive film (ACF, AC-4351Y, Hitachi Chemical Co. America, Ltd., Westborough, MA). ACF was 1.2mm wide with conductive particles ~3 um in diameter. Firstly, an ACF with protective layer was positioned on the I/O region, and presealed after being heated to 90 º and a pressure of 1 MPa for 1 min with a homemade hot bar or commercial bonding system (Fineplacer Lambda Manual Sub-Micron Flip-Chip Bonder, Finetech, Inc., Manchester, NH) to tack it on I/O part with protective layer removed. Then the flexible cable was placed on the ACF and aligned. At last, the endsealing was made with a temperature of 190 – 210 ºC in ACF and a pressure of 4 MPa on the top for 5 min applied by homemade hot bar or commercial bonding system. In order to demonstrate the adhesion strength of the interface between I/O pads and flexible cable, the structure was peeled from the substrate and examined by optical microscopy.

The connection resistance of ACF was measured to investigate the influence of bonding on electrical properties of devices (**Fig. 5-4c** and **d**). The conductance of each device was measured by probe station as R_0 and R_1 before and after ACF bonding, respectively. The connection resistance for each I/O pad (100 um diameter) was

calculated as $(R_1\text{-}R_0)/2$, illustrated in **Figure 5-4c**. The calculated connection resistance after ACF bonding with commercial bonder and homemade bonding is ca. 21.2Ω and ca. 33.7Ω respectively (**Fig. 5-4d**), below 0.05% of typical nanowire resistance and 0.03% of MEA device. The insulation resistance between I/O pads without circuits was over 10^{10} Ω. These measurements and calculation results demonstrated that ACF bonding had little influence on electrical properties of injectable electronics, which ensured reliable measurement of injectable electronics in many kinds of applications afterwards.

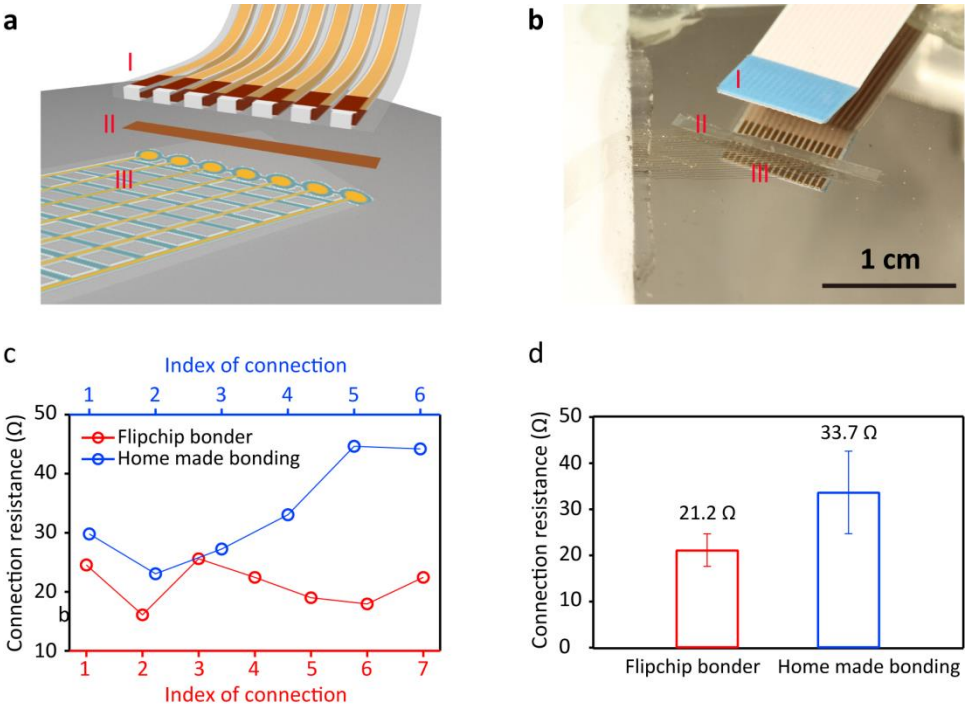

Figure 5-4 Bonding process. Schematics (**a**) and corresponding optical image (**b**) of bonding. (**I**) flexible cable, (**II**) ACF film and (**III**) unfolded I/O region of device on substrate. **c**. Connection resistance of ACF film bonded by flipchip bonder (red) and home-made bonding system (blue). **d**, Statistic results of connection resistance data in (**c**), showing the average value and standard deviation.

5.2.12 Imaging of electronics in glass channel

Electronics with different width, and mesh structure were injected into the glass channels following the same injection process described above. However, electronics was only partially injected through the needle. Confocal fluorescence microscope was used to

image the 3D structure of the electronics in the glass needle. *ImageJ* was used to re-slice the 3D reconstructed images of device in the longitudinal direction by the step of 1 μm.

5.2.13 Mechanical simulations

5.2.13.1 Bending stiffness simulation

We estimate the bending stiffness of the devices with different structures by finite element software ABAQUS. A unit cell is used for the simulation, and the tilt angle α is defined in **Figure 5-1**. The devices are modeled with shell elements. The longitudinal ribbons are partitioned into a one-layer part and a three-layer part. A homogeneous section with 700-μm thick SU-8 is assigned to the transverse ribbons, while a composite section with three layers of 300-nm thick SU8, 100-nm thick gold and another 300-nm thick SU-8 is assigned to the three-layer part of the longitudinal ribbons. Both SU-8 and gold are modeled as linear elastic material, with Young's modulus 2 Gpa and 79 Gpa respectively[12]. To calculate the longitudinal and transverse bending stiffness, a fixed boundary condition is set at one of the ends parallel with the bending direction, and a small vertical displacement, *d*, is added at the other end. The external work, *W*, to bend the device is calculated. We define the effective bending stiffness of the device as the stiffness required of a homogenous beam to achieve the same external work *W* under the displacement *d*. Therefore, the effective bending stiffness per width of the device can be estimated as

$$D = \frac{2Wl^3}{3d^2b}, \tag{1}$$

with *b* the width of the unit cell parallel with the bending direction, and *l* the length of the unit cell perpendicular to the bending direction.

5.2.13.2 Injection simulation

We further simulate a unit cell with the tilted angle α =45° going through a needle (**Fig. 5-5a**). The unit cell is bent by a rigid shell with radius of curvature *R* (**Fig. 5-5b**). A fixed boundary condition is set on one of the end of the device parallel with the bending direction. The distribution of the maximal principal strain ε_m is shown in the inset of Fig. 3c. When the radius of the needle *R* is 300 μm, the highest maximal principal strain is as small as 0.167%; when the radius of the needle *R* is 100 μm, ε_m reaches around 0.531%. The dependence of the highest maximal principal strain ε_m of the unit cell on the curvature 1/*R* is linear as shown in **Figure 5-5b**. The two colors correspond to two different sizes of the mesh structures. The two corresponding fitting relations are ε_m = 0.499/*R* and ε_m =0.473/*R* respectively.

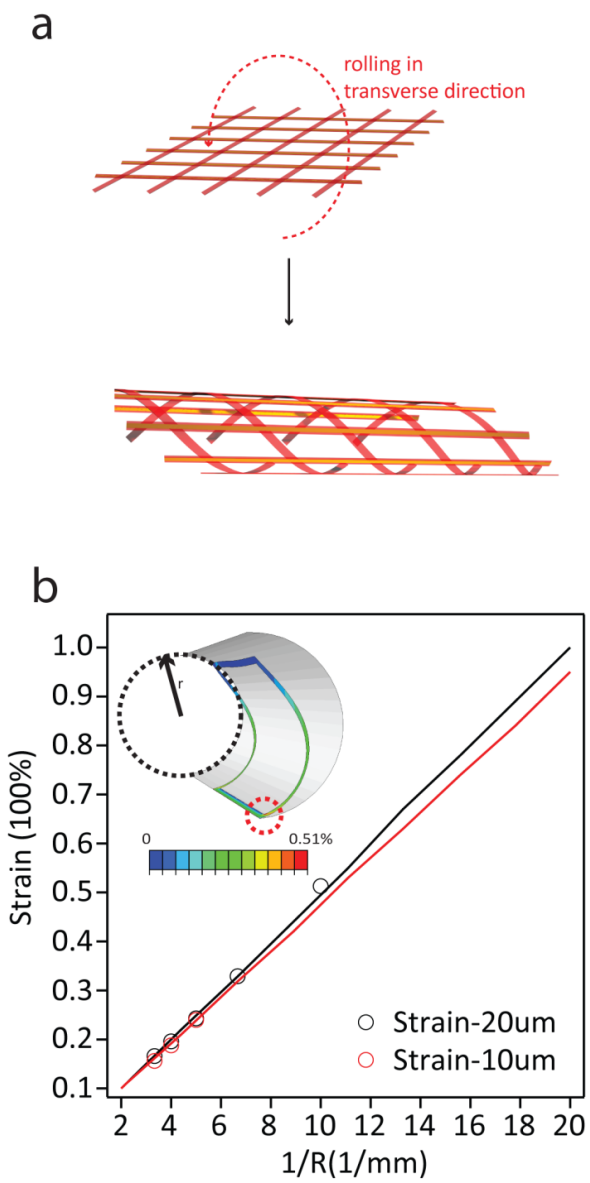

Figure 5-5 Mechanics of mesh during rolling. a, Schematics show that mesh roll up in transverse direction in needle. **b**, Simulated highest strain value as functions of 1 over needle radius. Inset is a representative simulation shows the strain distribution of unit cell in 200-um inner diameter needle. Red dashed circle highlights the point with highest strain. Black dashed circle and black arrow show the inner boundary and diameter of the needle.

5.2.13.3 Dimensional analysis of integration of the device with cells

When the electronics is injected into tissues, the flexibility of the electronics has been proved to be important for the survival of cells and interface between devices and

cells, especially in long-term chronic implantation[24]. When the electronics is too rigid to be bent, chronic damage will be induced by mechanical mismatch. Here we define a dimensionless number $D/\gamma L^2$, where D is the bending stiffness per width of the ribbons of electronics, γ is the membrane tension of cells and L is the length of the electronics. Since the bending curvature of the device scales as ~1/L, the bending energy scales[25] as ~Dw/L, with w is the width of the device. The surface membrane energy due to the insertion of the electronics scales as ~$n\gamma wd$, with n is the number of cells on the electronics and d is the size of cells. Considering in the long-term implantation, the electronics will fully contact with tissue, then nd scales as ~L. Therefore, the ratio of the bending energy and the surface energy gives the dimensionless number $D/\gamma L^2$, which describes the flexibility of the device compared to the membrane tension of cells. Our electronics have the properties of D ~ 0.36 nN·m[14] and L~ 300-500 μm, and typical cells have γ~1 mN/m[26] and neuron cells measured by AFM have γ~0.01-0.4 mN/m[27]. We can calculate $D/\gamma tL$~ 3.5-140. Given the elastic modulus of Si, carbon fiber, gold and SU-8 are 130 GPa[24], 234 GPa[28], 79 GPa and 2 GPa[8], respectively, we can calculate the bending stiffness of previous reported Silicon microelectronic probe, carbon fiber probe and thin film electronics is ca. 4.6×10^{-5}, 9.2×10^{-5} and 1.3×10^{-6} N·m. The ratio of the bending energy and the surface energy calculated for injectable electronics is orders magnitude smaller than conventional silicon microelectronics (1.15×10^{5}-4.6×10^{6})[24], carbon fiber probes (2.3×10^{5}-9.2×10^{6})[28] and reported thin film electronics (3.3×10^{3}-1.3×10^{5})[10]. Therefore the design of injectable electronics exhibits more mechanical flexibility to integrate with cells and tissues, especially in chronic implantation.

5.2.14 Inject electronics in soft matters

PDMS pre-polymer components were prepared in a 10:1 (base:cure agent; Sylgard 184, Dow Corning Corporation, Midland, MI) weight ratio at first, and diluted by hexane (n-hexane 95% optima, Fisher Scientific Inc., Pittsburgh, PA) in a 1:3 (PDMS:hexane) volume ratio. The cavity for injection was formed by two pieces of cured PDMS (cured at 65 ºC for 2 hours; Sylgard 184, Dow Corning Corporation, Midland, MI). Electronics was transferred from water to ethanol after etching, dissolved in PDMS/hexane solution and then loaded into glass syringe with 18 gauge metal needle. Device region was injected into the cavity, with I/O region injected outside the cavity on a silicon wafer or a glass side (VistaVision Microscope Slides, Plain and Frosted, VWR International, LLC, Radnor, PA). Hexane was used to wash away PDMS residues on the I/O region, after which the I/O region were unfolded with alcohol. The transition part of electronics from PDMS to substrate was fixed by Kwik-Sil (World Precision Instruments, Inc., Sarasota, FL) silicone elastomer to avoid damage to the device during the drying process. Finally, the hybrid structure of PDMS and electronics was cured at room temperature for 48 hours.

The I/O pads were bonded to flexible cable through ACF just as the process described above. The piezoelectric response to strain of the nanowire devices was calibrated using homemade clamp device with linear translocation stages under tensile or compressive strain in x direction, where the strain was calculated from the relative length change ($\triangle L/L$=0.5mm/54mm=0.9%). The strain field caused by point load in z direction was determined in experiments where the hybrid structure with calibrated nanowire strain sensors was subject to non-uniform deformations.

5.2.15 Inject electronics in Matrigel™ with and without neurons

Poly-D-lysine modified electronics was transferred into PBS solution and then into Neurobasal™ medium (Invitrogen, Grand Island, NY). Electronics was loaded into metal syringe needle as described above. Matrigel™ (BD Bioscience, Bedford, MA) was diluted into 30% (v/v) with neuron culture medium and polymerized at 37 ºC. Electronics was injected into polymerized Matrigel. The hybrid structure was incubated in 37 ºC to investigate the unfolding of electronics in Matrigel™.

5.2.16 Inject electronics in Matrigel™ with neurons

Hippocampal neurons (Gelantis, San Diego, CA) were prepared using a standard protocol described previously[4]. In brief, 5 mg of NeuroPapain Enzyme (Gelantis, San Diego, CA) was added to 1.5 ml of NeuroPrep Medium (Gelantis, San Diego, CA). The solution was kept at 37 ºC for 15 min, and sterilized with a 0.2-μm syringe filter (Pall Corporation, MI). Day 18 embryonic Sprague/Dawley rat hippocampal tissue with shipping medium (E18 Primary Rat Hippocampal Cells, Gelantis, San Diego, CA) was spun down at 200 g for 1 min. The shipping medium was exchanged for NeuroPapain Enzyme medium. A tube containing tissue and the digestion medium was kept at 30 ºC for 30 min and manually swirled every 2 min, the cells were spun down at 200 g for 1 min, the NeuroPapain medium was removed, and 1 ml of shipping medium was added. After trituration, cells were isolated by centrifugation at 200 g for 1 min and then resuspended in 5-10 mg/ml Matrigel™ at 4 ºC. Matrigel™ with neurons were mixed with electronics at 4 ºC and then loaded into syringe with metal gauge needle. The electronics and neurons were co-injected into 30% (v/v) polymerized Matrigel™ in culture plate and

then placed in incubator to allow Matrigel™ to gel at 37 ºC for 20 min. Then 1.5 mL of NeuroPure plating medium was added. After 1 day, the plating medium was changed to Neurobasal™ medium (Invitrogen, Grand Island, NY) supplemented with B27 (B27 Serum-Free Supplement, Invitrogen, Grand Island, NY), Glutamax™ (Invitrogen, Grand Island, NY) and 0.1% Gentamicin reagent solution (Invitrogen, Grand Island, NY). The *in-vitro* co-cultures were maintained at 37 °C with 5% CO_2 for 14 days, with medium changed every 4-6 days.

5.2.17 Immunostaining and imaging of neurons and electronics

Cells were fixed with 4% paraformaldehyde (Electron Microscope Sciences, Hatfield, PA) in PBS for 15-30 min, followed by 2-3 washes with ice-cold PBS. Cells were pre-blocked and permeabilized (0.2-0.25% Triton X-100 and 10% feral bovine serum (F2442, Sigma-Aldrich Corp. St. Louis, MO) for 1 hour at room temperature. Next, the cells were incubated with primary antibodies Anti-neuron specific β-tubulin (in 1% FBS in 1% (v/v)) for 1 hour at room temperature or overnight at 4 ºC. Then cells were incubated with the secondary antibodies AlexaFluor-546 goat anti-mouse IgG (1:1000, Invitrogen, Grand Island, NY). For counter-staining of cell nuclei, cells were incubated with 0.1-1 µg/mL Hoechst 34580 (Molecular Probes, Invitrogen, Grand Island, NY) for 1 min.

5.2.18 Mouse Surgery

5.2.18.1 Animal preparation

Adult (25-35 g) male C57BL/6J mice (Jackson lab) were group-housed, giving access to food pellets and water *ad libitum* and maintained on a 12 h: 12 h light: dark cycle. All animals were held in a facility beside lab 1 week prior to surgery, post-surgery and throughout the duration of the behavioral assays to minimize stress from transportation and disruption from foot traffic. All procedures were approved by the Animal Care and Use Committee of Harvard University and conformed to US National Institutes of Health guidelines.

5.2.18.2 Stereotaxic surgery

After animals were acclimatized to the holding facility for more than 1 week, they were anesthetized with a mixture of 60 mg/kg of ketamine and 0.5 mg/kg medetomidine (Patterson Veterinary Supply Inc., Chicago, IL) administered intraperitoneal injection, with 0.03 mL update injections of ketamine to maintain anesthesia during surgery. A heating pad (at 37°C) was placed underneath the body to provide warmth during surgery. Depth of anesthesia was monitored by pinching the animal's feet periodically. Animal was placed in a sterotaxic frame (Lab Standard Stereotaxic Instrument, Stoelting Co., Wood Dale, IL) and 1-mm longitudinal incision was made, and skin was resected from the center axis of the skull, exposing a 2 mm by 2mm portion of the skull. The dura was incised and resected from the surface of the skull. Next, a 0.5-mm diameter hole was drilled into the frontal and parietal skull plates using a dental drill (Micromotor with On/Off Pedal 110/220, Grobet USA, Carlstadt, NJ).

Sterile saline was swabbed on the brain surface to keep it moist throughout the throughout the surgery. Sterotaxic arm was used to clamp needle containing the injectable electronics. Electronic was loaded into the needle by first connecting the glass needle to a syringe via a plastic tube and drawn into the end of the glass needle. The glass needle was then detached from the syringe and then mounted to a patch-clamp setup for injection. The glass needle had a diameter of 100 – 200 μm. The needle was lowered into the exposed brain surface and the syringe or microinjector was used to inject the electronics into the brain. The needle was lowered approximately 1 mm into the skull (Interaural: 6.16 mm, Bregma: -3.84 mm), to test the effects of deep brain and superficial layer injections. After injection, needle is drawn out of the brain tissue and the I/O region is injected on the surface of the skull.

After injection, the skin that was retracted from the center axis was replaced and the incision was sealed with C&B-METABOND (Cement System). Anti-inflammatory and anti-bacterial ointment was swabbed onto the skin after surgery. A 0.3 mL intraperitoneal injection of Buprenex (Patterson Veterinary Supply Inc. Chicago, IL, diluted with 0.5 ml of PBS) for 0.1 mg/kg was administered to reduce post-operative pain. Animals were observed for four hours after surgery and hydrogel was provided for food, and heating pad was on at 37°C for the remainder of post-operative care. All procedures complied with the United States Department of Agriculture guidelines for the care and use of laboratory animals and were approved by the Harvard University Office for Animal Welfare.

5.2.18.3 Incubation and behavioral analysis

Animal was cared for every day for 3 days after the surgery and every other day after first 3 days. Animal was administered with 0.3 mL of Buprenex (0.1 mg/kg, diluted with 0.5 mL PBS) every 12 hours for 3 days. Animal was also observed every other day for behavioral changes. Animals, which were surgically operated on, were housed individually in cage with food and water *ad libitum*. The room was maintained at constant temperature on a 12-12 h light-dark cycle.

5.2.18.4 Brain tissue preparation for chronic immunostaining

(1) Mice underwent transcardial perfusion (40 mL PBS) and were fixed with 4% formaldehyde (Sigma, 40 mL) 4-5 weeks after the surgery[29]. (2) Mice were decapitated and brains were removed from the skull and set in 4% formaldehyde for 24 hours as post fixation and then PBS for 24 hours to remove extra formaldehyde. Electronics was kept inside the brain throughout fixing process. (3) Brains were blocked, separated into the two hemispheres and mounted on the stage of vibratome (Vibrating Blade Microtome Leica VT1000 S, Leica Microsystems Inc. Buffalo Grove, IL). 50-100 μm vibratome tissue slices (horizontal and coronal orientations) were prepared for samples with staining for microglia, astrocytes and nuclei. 30-50 μm vibratome tissue slices (horizontal and coronal orientations) were prepared for samples with staining for neurons. For samples with electronics injected in lateral ventricle, brains were blocked and then fixed in 1% (w/v) agarose type I-B (Sigma-Aldrich Corp., St. Louis, MO) to fix the position of electronics in the lateral ventricle cavity and then mounted on the stage of vibratome. 100 μm vibratome tissue horizontal slices were prepared. Coronal slices allowed for cuts in a

direction along the long axis of the injected electronics and horizontal slices allowed for cuts in a direction perpendicular to the long axis of the injected device.

5.2.18.5 Chronic Immunohistochemistry: Microglia, Astrocytes and Nuclei

(1) Sections were then cleared with 5 mg/mL sodium borohydride in HEPES-buffered Hanks saline (HBHS, Invitrogen) for 30 minutes, with 3 following washes with HBHS in 5-10 minute intervals. Sodium azide (4%) was diluted 100x in HBHS in all steps using HBHS. (2) Slices were incubated with 0.5% (v/v) Triton X-100 in HBHS for 30 min at room temperature. (3) Slices were blocked with 5% (w/v) FBS and incubated overnight at room temperature. (4) Slices were washed four times in 30 min intervals with HBHS to clear any remaining serum in the tissue. Slices were then incubated overnight at room temperature with the GFAP primary antibody (targeting astrocytes, 1:1000, Invitrogen #13-0300, lot #686276A) and rabbit anti-Iba-1 primary antibody (targeting microglia, 1:800, Wako #019-19741, lot #STN0674) containing 0.2% triton and 3% serum. (5) After incubation period, slices were again washed four times for 30 minutes with HBHS, slices were incubated with secondary antibody (1:200; Alexa Flour 546 goat anti-rat, 1:200; Alexa Fluor 488 goat anti-rabbit secondary antibody, Invitrogen, Carlsbad, CA), Hoechst 33342 (nuclein stain 1:150, Invitrogen #h-1399, lot #46C3-4) 0.2% Triton and 3% serum overnight. (6) After the final washes (four for 30 min each HBHS), Slices were mounted on glass slides with coverslips using Prolong Gold (Invitrogen) mounting media. The slides remained covered (protected from light) at room temperature, allowing for 12 hours of clearance before imaging.

5.2.18.6 Chronic Immunohistochemistry: Neuron

Slices were cleared with 5 mg/mL sodium borohydride in HBHS for 30 minutes, with 3 following washes with HBHS in 5-10 minute intervals. Then, slices were incubated with 0.5% (v/v) Triton X-100 in HBHS for 30 min at room temperature. Next, sections were blocked with 5% (w/v) serum and incubated overnight at room temperature. Next, slices were washed four times in 30-minute intervals with HBHS to clear any remaining serum in the tissue. Slices were then incubated with primary antibody (NeuN, 1:200, AbCam #ab77315) in 0.3% Triton-X100 and 3% serum in PBS overnight at room temperature. After 24 hours, sections were washed four times for 30 minutes in PBS and then counterstained with Hoechst 33342 (1:5000, Invitrogen #H35770). Prolong gold coverslips were used again to protect from light and allowed for 12 hrs of clearance before imaging. When the antibody solutions were first prepared, they included 0.3 Triton X-100 and 5% normal goat serum.

5.2.18.7 Immunostaining for electronics in the cavity of lateral ventricle

Slices were cleared with 5 mg/mL sodium borohydride in HBHS for 30 minutes, with 3 following washes with HBHS in 5-10 minute intervals. Then, slices were incubated with 0.5% (v/v) Triton X-100 in HBHS for 30 min at room temperature. Next, sections were blocked with 5% (w/v) serum and incubated overnight at room temperature. Next, slices were washed four times in 30-minute intervals with HBHS to clear any remaining serum in the tissue. Slices were then incubated with primary antibody (NeuN, 1:200, AbCam #ab77315) in 0.3% Triton-X100 and 3% serum in PBS overnight at room temperature. After 24 hours, sections were washed four times for 30 minutes in PBS and then counterstained with Hoechst 33342 (1:5000, Invitrogen

#H35770). Prolong gold coverslips were used again to protect from light and allowed for 12 hrs of clearance before imaging. When the antibody solutions were first prepared, they included 0.3 Triton X-100 and 5% serum.

5.3 Results and discussion

5.3.1 Syringe injectable electronics

Figure 5-6 shows the schematics of the basic idea. Electronics are in a mesh network encapsulated in a photodefinable epoxy (SU-8), which are fabricated on a nickel sacrificial layer as reported previously[14], and then completely removed from the substrate with electronic sensor units, metal connections and input/output (I/O) pads all distributed on this freestanding network (**Fig. 5-1**). We can load electronics into syringe and then delivered/injected through the needle (**Fig. 5-6a**) with its subsequent geometrical restoration (**Fig. 5-6b** and **c**). Through the control of injection process, the I/O can be injected on the outside of injected system for electric connections.

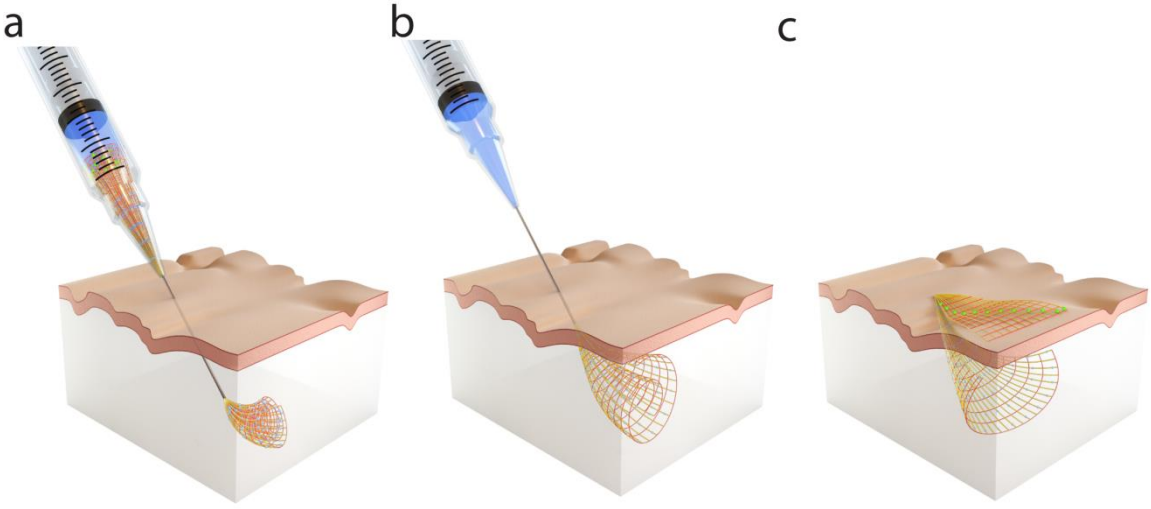

Figure 5-6 Concept for injectable electronics. a, mesh electronics is loaded into syringe and injected into targeted system. **b**, mesh electronics is injected into targeted system and gradually unfold. **c**, mesh electronics has been injected into targeted system and totally unfold with I/O region injected outside for bonding. Blue and green dots: nanodevice and

(Continued) I/O pads; yellow: metal line encapsulated in polymer; red: supporting polymer; blue: solution.

In our design, the width of ribbons in the network is typically 5 – 40 μm, the total thickness is less than 800 nm and the size of unit cells is several hundred micrometers (**Fig. 5-1**). **Figure 5-7a** shows a 3D reconstructed confocal fluorescence image of a representative injection. 2-mm-wide syringe injectable electronics was injected through a glass needle with 95-μm inner diameters into aqueous phosphate buffer saline (PBS). This electronics has ribbons with feature size of 5 μm and thickness of 700 – 800 nm. The surface of electronics has been modified by poly-D-lysine (0.5-1.0 mg/mL, MW 70,000 – 150,000) to make the surface of the electronics hydrophilic, allowing the electronics to be suspended in PBS solution. The stepwise process of this injection into free solution is shown in **Figure 5-7b**. Electronics was loaded into a glass tube (with 95 um tip) by first connecting glass needle to a syringe via a plastic tube and drawn into the end of glass needle. Glass needle was then detached from the syringe and then mounted onto a commercially available patch-clamp system. Microinjector (ALA Scientific Instruments) or manually controlled syringe is connected to the glass needle to apply sufficient pressure (1 bar, 1-10 ms) for injection.

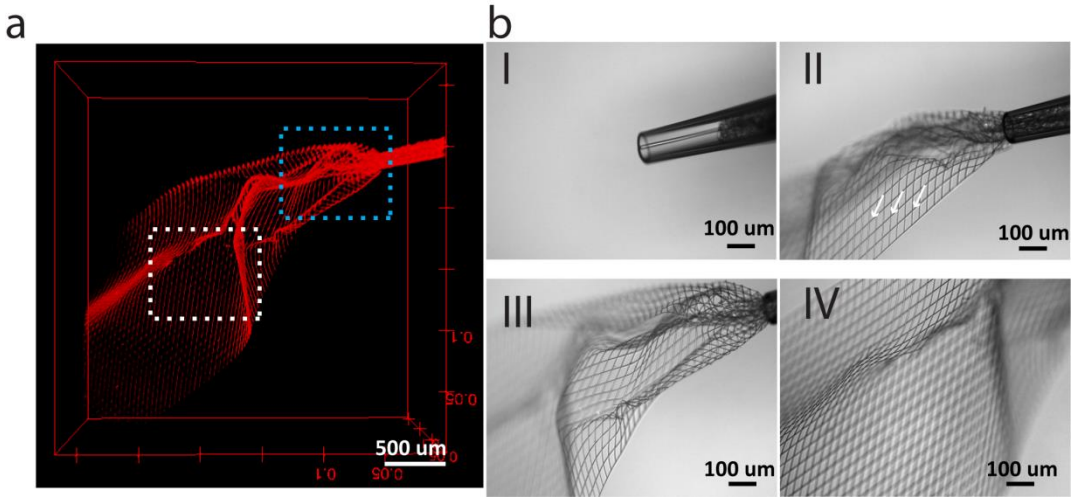

Figure 5-7 Stepwise injection. a, 3D reconstructed fluorescence image shows the electronics are injected out from needle (blue dashed box) and subsequently self-unfolded in the solution. **b**, Images show that electronics are stepwise injected into solution by glass needle with diameter of 90 um. Electronics was pushed to the tip of needle (**I**), electronics was partially injected out (**II**), 50% area of whole electronics was injected out, with partially unfolded mesh structure near needle region (**III**) corresponding to the region highlighted by blue dashed box in (**c**), and completely unfolded mesh structure (**IV**) corresponding to the region highlighted by white dashed box in (**a**).

Using the microinjector, we are able to inject electronics out gradually from needle with the electronics being displaced from the needle by 5 – 10 μm per injection, with less than 100 nL solution in each injection (**Fig. 5-8**). The injected region of electronics gradually unfolds in solution to reduce the surface energy and internal strain. We are able to control the injection process such that only the region of electronics containing the nanodevices is injected into the target system whereas the metal contact and I/O region is injected outside for external control. Anisotropic conductive film (ACF) was used in our study to bond the I/O pads of electronics with external set-ups (**Fig. 5-4**).

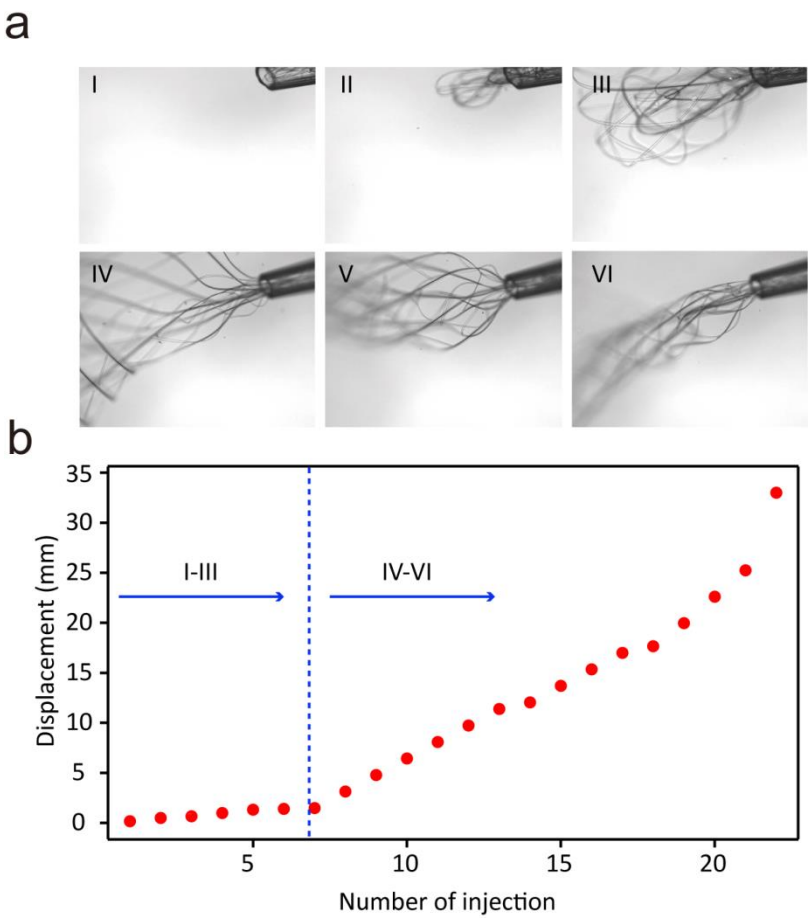

Figure 5-8 Control of injection process. a, Optical images of a typical device during injection process. (**I-VI**) The device is gradually injected into free solution by micro-injector with 1 bar pressure, 10 ms pulse (before blue dashed line in b) and 50 ms pulse (after blue dashed line in (**b**)) injection time for each step. **b**, The injected length of device vs. number of injection. Blue arrow (**I-III**) corresponding to images (**I-III**) in a. Blue arrow (**IV-VI**) corresponding to images (**IV-VI**) in (**a**).

The relationship between the yield of injection and the electrical performance of electronics to the inner diameter of needle was evaluated by injection through conventional metal gauge needle in PBS solution (**Fig. 5-9**). The average yield of injection for nanowire electronics ranges from 98% with needle diameter larger than 600 um to 83% with needle diameter of 100 um. Less than 12% conductance change in average has been observed after injection. The average yield of injection for metal electrode ranges from 90% to 98%. Less than 10% conductance change in average has

been observed after injection. Altogether, these results demonstrate the success of the injection of mesh electronics without hindering the integrity and performance of the electronics. Several design factors are very important to the success of injection: (1) the nanometer-thickness and mesh design increase the surface-to-volume ratio of electronics from 0.2 μm^{-1} for typical 10-μm-thick thin film electronics to 3.25 μm^{-1} for 5-μm-wide ribbon mesh electronics so that (a) with polyelectrolyte surface charge modifications, it can reduce the effective density of electronics (due to the forming of electric double layers) making electronics suspended in solution, and (b) it can also increase the drag force of solution motion to electronics making electronics be readily displaced by solution motion to enable injection. (2) the nanometer-thickness and mesh layout together (a) reduce the effective bending stiffness of electronics from 0.0602 nN·m for a thin-film electronics with the same thickness, to 0.0025 nN·m for the mesh electronics so that it can be readily bent and injected into needles, (b) reduce the strain in the device during injection, and (c) reduce the total volume of electronics to allow electronics to go through a small diameter needle.

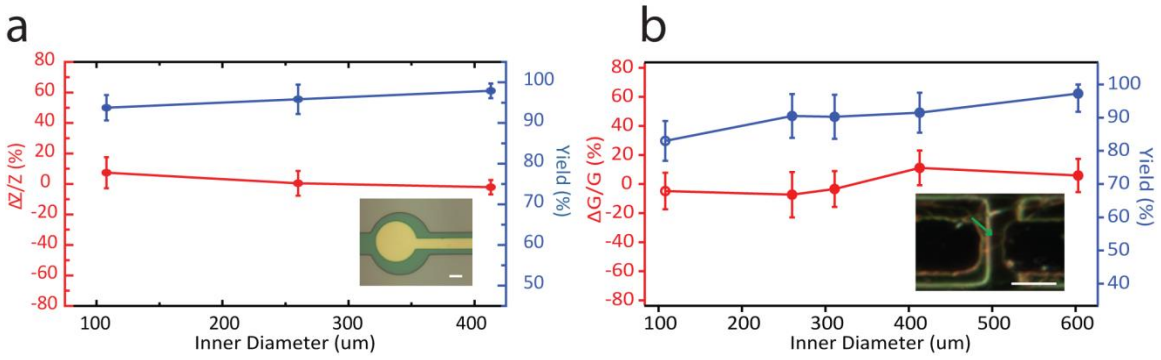

Figure 5-9 Yield of injection. a, Yield (blue) and impedance change (red) of electronics containing metal electrode injected through different gauge needles inset: bright field image of metal electrode on mesh electronics. **b**, Yield (blue) and conductance change (red) of electronics containing nanowire field-effect transistor injected through different gauge needles. Solid spot: 5 mm wide mesh, hollow spot: 2 mm wide mesh. Inset: bright

(Continued) field image of nanowire FET (highlighted by green arrows) on mesh electronics. Scale bar: 10 um.

5.3.2 Parameters for syringe injectable electronics

To further understand the structure design parameters for injection, we carried out imaging experiments using confocal fluorescence imaging to 3D reconstruct the structure of injectable electronics inside the glass needle. A glass tube was pulled into a fluidic channel (**Fig. 5-10a**), with the same geometry and inner diameter as the metal and glass needle used for applications, which allows the electronics to be injected through for imaging. The channel inner diameter is 200 – 600 μm measured by confocal fluorescence imaging and the length is 0.1 – 0.5 mm. Electronics with different structure was injected through the tube region into channel by syringe. SU-8 of electronics was doped by Rodamine-6Gfor imaging and 3D reconstruction for analysis.

We call the ribbons along the injection direction as longitudinal ribbons and the ribbons perpendicular to the injection direction as transverse ribbons. Longitudinal and transverse ribbons together form mesh with a periodic unit cells structure. All the unit cells are identical in our design. Metal connections and nanodevices are mainly encapsulated in longitudinal ribbons (**Fig. 5-10b**). The ribbons in our design for imaging experiments are 20-μm-wide and 700-nm-thick for SU-8 and 10-μm-wide and 100-nm-thick for metal. Different width of mesh was used for investigating the limitation because wider electronics allow sensing units to cover a larger area. All the mesh have a sharp tip of 45º, which guarantees that they can be loaded into needles at the same tip point (**Fig. 5-10b**). Two different meshes with different unit cell geometries have been used here to investigate the injection. In design #1, the transverse ribbons are tilted 45° counterclockwise in transverse direction on the mesh plane forming 45° angle to

longitudinal ribbons. In design #2, the transverse ribbons are perpendicular to the longitudinal ribbons to form an orthogonal mesh (α=0º). **Figure 5-10 c-e** show optical micrographs, 3D-reconstructed and cross-section images of assembled structures for each mesh in the glass channel. Firstly, 5-mm-wide mesh with #1 design structure can be smoothly injected through a channel with ca. 500-μm-inner-diameter (**Fig. 5-10c, I**). The 3D-reconstructed image shows that mesh has been rolling into a tubular structure inside the channel, which keeps the longitudinal ribbons straight and makes the transverse ribbon bended (**Fig. 5-10d, I**). The cross-section image of 3D reconstruction further confirms the tubular structure, illustrating that all of the ribbons are closely and uniformly packed close to the inner surface of glass channel. The other half of mesh in the bottom part of the needle is blocked from imaging by the dense ribbons on the top part of channel. Secondly, reducing channel's inner diameter does not affect the assembled structure of mesh in the needle. The same mesh can be injected smoothly in through 200-μm-inner-diameter channel (**Fig. 5-10c, II**). The 3D-reconstructed and cross-section images further demonstrate the tubular structure of mesh in the needle and closed packed ribbons to the inner wall of channel (**Fig. 5-10d, II** and **5-10e, II**). Thirdly, increasing the width of mesh can also allow the mesh to be smoothly injected through channels. As a representative example, 15-mm-wide mesh can be injected through the channel with an inner diameter of ca. 500 μm (**Fig. 5-10c, III**). The width-to-inner-diameter ratio is ca. 30. The 3D-reconstructed and cross-section images (**Fig. 5-10d, III** and **5-10e, III**) again show the tubular structure of mesh in the channel and closed packed ribbons to the inner wall of channel. Importantly, although the density of ribbon has been greatly increased, the longitudinal ribbons still remain straight during injection. Fourthly, as control sample,

we found that the mesh with #2 design could not be injected through the channel with 500-μm inner diameter. Different with the regularly tubular structure formed by design #1, a 10-mm-wide mesh forms a jammed structure caused by ribbons entanglement blocking the channel (**Fig. 5-10c, IV**). 3D-reconstructed and cross-section imaging further shows the ribbons entangled together buckles (**Fig. 5-10d, IV** and **5-10e, IV**), which fulfills the whole channel. It is very important to keep the longitudinal ribbons straight during injection to avoid (1) the high-strain deformation to the electronics damaging device and (2) buckling of the longitudinal ribbons. Buckling of the longitudinal ribbons can dramatically decrease the stiffness of the structure in the longitudinal direction[30], and therefore, collapsing of the longitudinal ribbons rather than bending of the transverse ribbons becomes preferential, causing large strain and damages of the device and even blocking the needle for further injection.

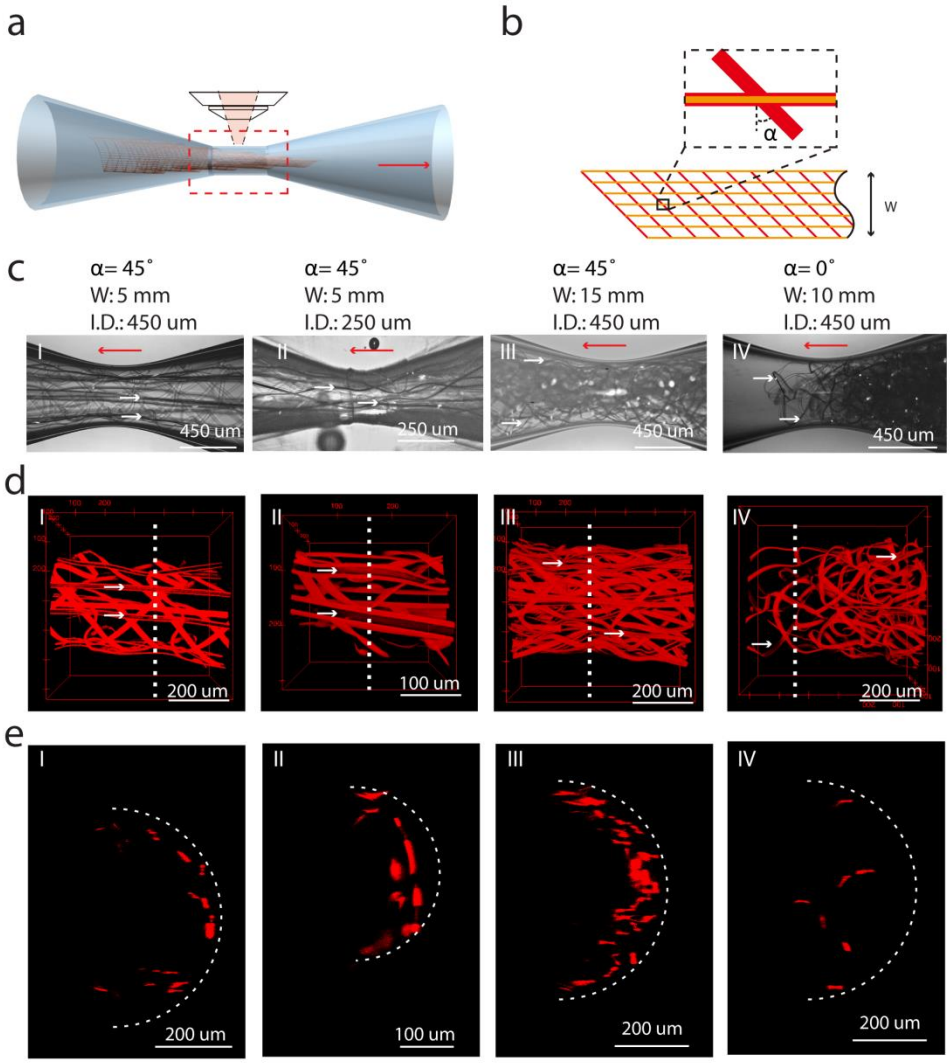

Figure 5-10 Parameters for injection. a, Schematic shows the structure of the pulled glass tube for testing and imaging the structure of different electronics design in the needle. Red arrow indicates the direction of injection. **b**, Schematics of design for injection. The dashed black circles highlight the detailed structure where red represents supporting and passivation polymer and yellow represents metal lines. **c**, Optical images of different electronics design injected through glass needle. (**I-II**) 5 mm wide meshes as design in (**b, I**) were injected through 450 um and 250 um ID glass needle; (**III**) 15 mm wide mesh as design in (**b, I**) was injected through 450 um ID needle. (**V**) 10 mm mesh as design in (**b, II**) was injected through 450 um ID needle. **d**, Top view of 3D reconstructed confocal images corresponding to (**c**). White arrows in c and d highlight metal contacts in the mesh. **e**, Images at cross-sections as indicated by white dashed lines in (**c**). White dashed curves in e highlight the cross-section of needle boundary.

We believe that the different assemble structure of these two meshes in the channel and needle can be explained by the following. We define the bending stiffness

for mesh bent in longitudinal direction and transverse direction of injection as D_L and D_T respectively. Firstly, the orthogonal-transverse-ribbon design (design #2) leads to a non-uniform distribution of effective bending stiffness D_L. Considering the effective bending stiffness D_L of different cross-sections, when the cross-section goes through the transverse ribbons, the bending stiffness is high (0.0602 nN·m), while when the cross-section does not go through the transverse ribbons, the bending stiffness is very low (0.0025 nN·m). This dramatic bending stiffness change facilitates stress localization leading to the buckling of longitudinal ribbons. On the contrary, tilted-transverse-ribbon design (design #1) creates a uniform distribution of effective bending stiffness D_L, therefore, the electronics can bend more homogeneously. Secondly, this tilted-transverse-ribbon design decreases D_T and increase D_L so that the mesh is more readily to bend and roll-up into tubular structure going through the needle and less readily buckle in the longitudinal direction.

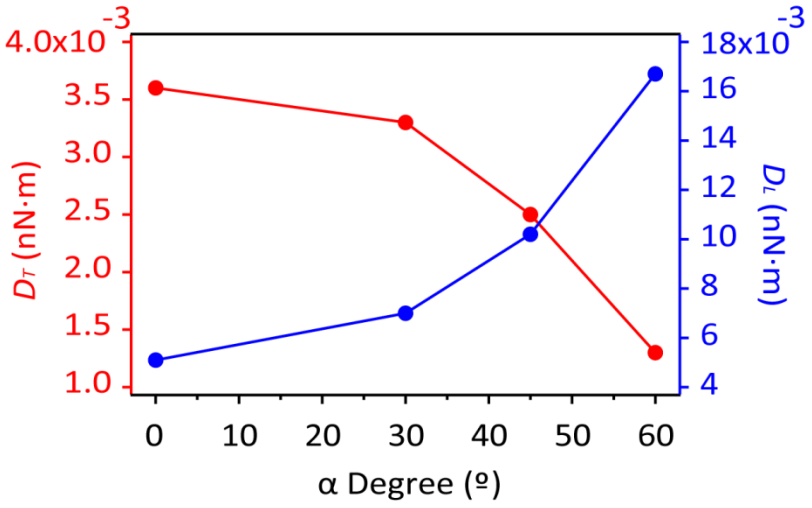

Figure 5-11 Mechanical analysis for injection process. Bending stiffness in longitudinal and transverse direction of the mesh with change of ribbons angle in **Figure 5-1**.

To further prove this idea, we conducted finite element modeling (FEM) analysis to simulate the bending stiffness for mesh bending in two directions. Notably, reducing the D_T and increases D_L is benefit to the injection process. **Figure 5-1** is the schematic showing how to select unit cells from the periodic mesh structure for simulation. The relation of angle α that is between transverse ribbon and longitudinal ribbon to bending stiffness was investigated. The white dashed lines indicate the boundary for unit cells from mesh for simulation. We define effective bending stiffness of mesh as the stiffness required a homogenous beam to achieve the same bending under the same moment. Therefore, every unit cell has the same bending stiffness and we use a unit cell to calculate the effective bending stiffness of the structure from the simulations. The results (**Fig. 5-11**) show that increasing α from 0 to 60 º, D_T decreases from 0.0036 to 0.0013 nN·m and D_L increases from 0.0051 to 0.0167 nN·m. The bending stiffness ratio between bending in transverse and longitudinal direction increases for 8.7 times (1.46 to 12.8). Altogether, those results show that increasing the tilted angle can significantly facilitate the rolling of electronics in the needle in transverse direction to form a tubular structure and prevent bending in the longitudinal direction that could lead to buckling and compression on same injection condition.

We further do simulations to estimate the strain distribution in the electronics during injections in needles with different sizes. Since every unit cell behaves similarly, we only simulate the bending of a unit cell to the curvature of the needle. The inset of **figure 5-5b** shows one typical unit cell bending structure inside 200-μm diameter needle and color mode shows the contour plot of the maximal principle strain. The maximal value is reached on the junction between the transverse and longitudinal ribbons.

Simulation results (**Fig. 5-5b**) show the dependence of the maximal principal strain of the unit cell on the curvature of the needles 1/*r*, and a linear relation can fit the dependence. The two colors correspond to two different sizes of the mesh structures used for needle inner diameter larger or smaller than 200 μm. the two corresponding fitting relation are 0.499/*r* and 0.473/*r*. For the needle diameter around 100 μm, the maximal principle strain can be extrapolated as 0.998% and 0.946% respectively, which are both smaller than the critical breaking strain of SU-8 for bulk materials. The stress intensity factor *K* for a thin film under pure bending has the following scaling relation[31] $K \sim E\varepsilon\sqrt{h}$, where *E* is the Young's modulus of the material, and *h* is the thickness of ribbon. The ribbon breaks when *K* reaches the toughness of the material K_c. K_c is usually on the order of 100 $KPa\sqrt{m}$,[32] and E for SU-8 is around 1 GPa. Therefore, for a device with thickness several hundred nanometers, the fracture strain ε_c is on the order of several percent. In fact, with our current structure, experiment demonstrates that SU-8 ribbon can sustain the bending with curvature larger than 0.1 μm^{-1} that corresponds to the curvature of 20-μm-diameter needle.

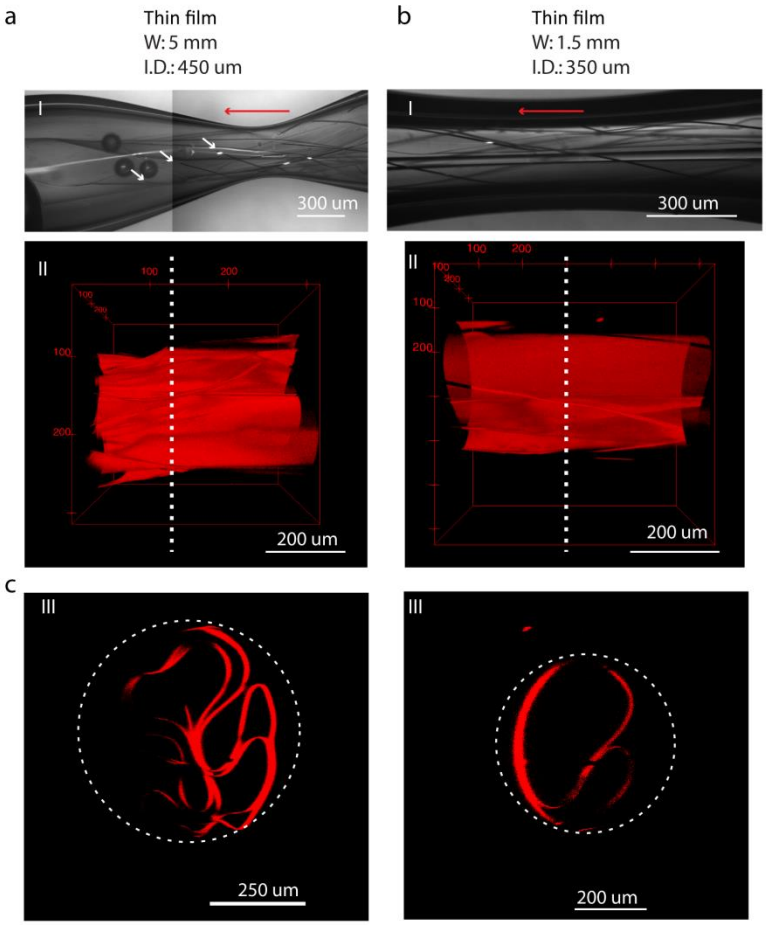

Figure 5-12 Control experiments of thin film electronics in needle. a (**I, II**), Optical image shows 5-mm-wide thin film electronics was injected through 400-um inner diameter glass needle (**I**), and 1.5-mm-wide thin film electronics was injected through 350-um inner diameter glass needle (**II**). Red arrow indicates the direction of injection. White arrows in (**I**) indicate the end of metal line to show the thin film cannot totally go through the needle. **b** (**I, II**), Top view of 3D reconstructed confocal images correspond to dashed box in (**a**). **c** (**I, II**), Images at cross-section as indicated by white dashed line in b. White dashed circle in (**c**) highlights the needle boundary.

Last, we tested the injection by using thin film electronics with same thickness. Important, the thin film electronics cannot have a tubular structure inside needle (**Fig. 5-12a**). Moreover, for ca. 400-μm inner diameter needle, only 1.5 mm thin film electronics can go through (**Fig. 5-12b**). These results further demonstrate the unique design of the mesh electronics for injection.

5.3.3 Inject electronic into soft matters

To demonstrate that syringe injectable electronics can be injected with various mediums and materials into a cavity through a small injection site with subsequent geometrical restoration allowing the electronic sensor unit to cover a much larger area within the cavity (**Fig. 5-6c**). 15-mm-wide electronics containing nanowire strain sensors was mixed with pre-cured poly-dimethylsiloxane (PDMS) (Down corp. Midland, USA) diluted in hexane and then injected through a 20-gauge (603 μm) needle into a cavity constituted by two pieces of cured PDMS (**Fig. 5-13a**) with the connections injected outside for bonding. The electronics within the cavity gradually unfolded, with the nanowire nanodevices fully separating from each other and covering the 15 mm x 20 mm area (**Fig. 5-13 b and c**). In addition, due to the flexibility of the injected electronics, it can unfold and cover the three-dimensional geometry in the cavity. **Figure c, II** shows Micro-CT three-dimensional reconstructed imaging of electronics unfolded and covered the step-like structure inside the PDMS cavity. 11 nanowire devices from the injected electronics were used as strain sensor. Their conductance change can be recorded from a point load in z-direction introducing a non-uniform strain distribution in PDMS (**Fig. 5-13d**), which is consistent with our previous report[14]. This result proves that injected electronics can be used to measure strain distribution inside PDMS to the external mechanical deformation and demonstrate the injectable electronics can be used in materials and tissue interrogation with little damage to the target system.

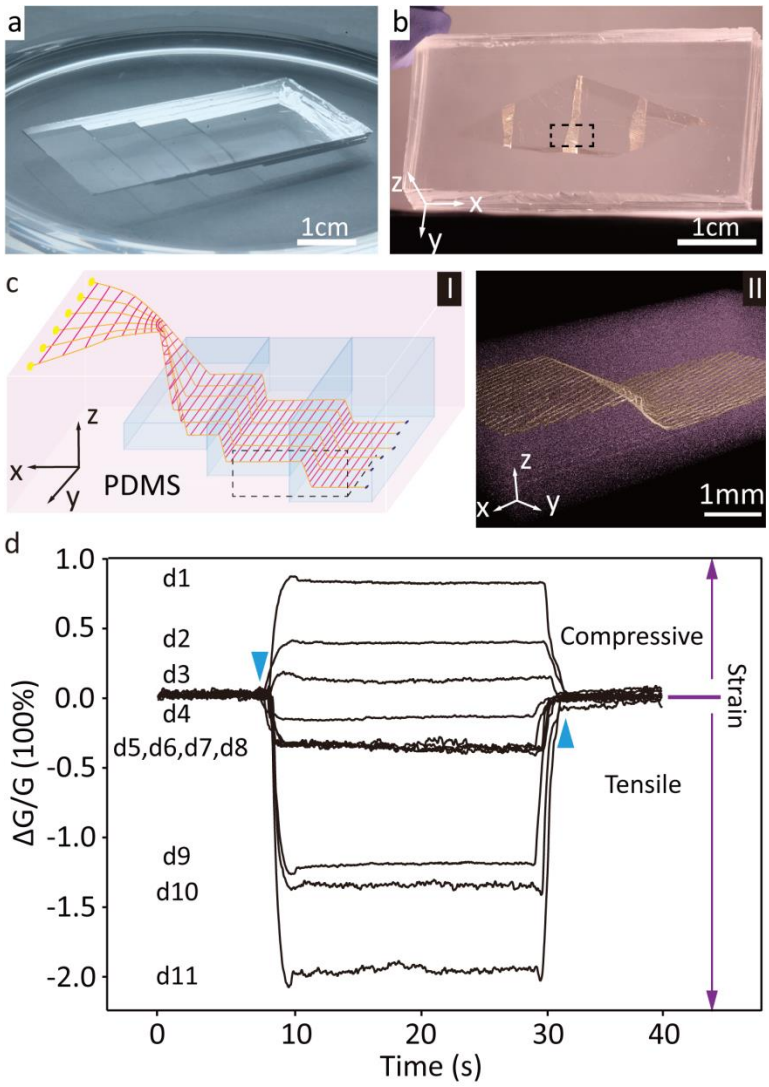

Figure 5-13 Injectable electronics in PDMS. **a** and **b**, Optical images of PDMS cavity before injection (**a**) and the hybrid structure of injectable devices embedded in PDMS after injection (**b**). **c**, Schematic of electronics injected and cured in cavity of PDMS with I/O pads unfolded outside the cavity (**I**). Red, SU8; Yellow, metal/SU8; Blue, nanodevices. Micro-CT image (**II**) shows the zoomed-in structure highlighted by the black dashed box in (**b**) and (**c, I**). Pseudocolors are applied: Yellow, metal; Purple, PDMS. **d**, 11 nanowire devices response to point loading on the PDMS. The downward and upward pointing triangles denote the times when the strain was applied and released, respectively. The upward and downward arrows show the compressive and tensile strains, corresponding to the plus and minus change of conductance respectively.

We have further extended this co-injection concept by demonstrating the injection of electronics in continuous biomaterials together with embryonic neural cells. (**Fig. 5-14**). Embryonic rat hippocampal neurons were mixed with electronics and uncured

Matrigel™ and subsequently injected into polymerized Matrigel™ (**Fig. 5-14a**). 3D-reconstructed confocal micrographs from two-week culture showed that neurons with high-density outgrowth neurites interpenetrating in the mesh structure of electronics, proving the biocompatibility of the electronics. It is noticeable that the width of ribbons was similar to the neurite projections, exhibiting seamless integration between them **(Fig. 5-14b**).

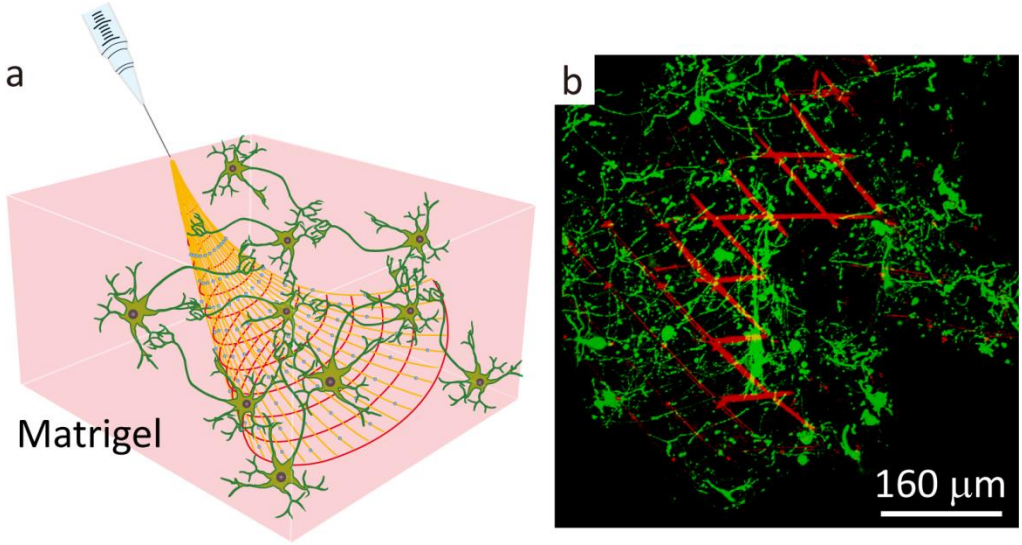

Figure 5-14 Inject electronics into gel. a, schematic of injection of electronics with neuron cells into Matrigel. Red, SU8; Yellow, metal/SU8; Blue, nanodevices; Green, neuron cells. **b**, Confocal fluorescence images of 100 um projection show the interpenetration between neurons and ribbons of injectable electronics after co-injected into matrigel for 14 days. Red: reflective image of mesh and green: beta-tubulin staining for neurons.

5.3.4 Inject electronics into *in-vivo* system

Based on our simulation, the D_L of this injectable electronics is ca. 0.01 nNm, which is similar to the bending stiffness of tissue and its bending energy matches the surface membrane energy[26] and significantly less than the stiffness of the conventional silicon probe and carbon fibers[24, 28]. In addition, our previous studies[8] have demonstrated that the design of these macroporous structures has allowed for the growth of tissue

within the interior space. Together, injectable electronics is a great candidate for *in-vivo* chronic implants.

We conducted the *in-vivo* chronic implantation experiments by stereotactically injecting electronics into rodent brain tissue with a 0.5 mm diameter drilled hole from craniotomy. The injection follows steps illustrated in **Figure 5-15a** and **b**. Specifically, 2-mm-wide electronics was injected into the tissue-dense hippocampus region of the mice (**Fig. 5-15c, I**) through a ca. 200-um inner diameter glass needle controlled by microinjector, which allowed trace amount of solution (<1 uL) to be injected with electronics in each injection. Fluorescence imaging of coronally sliced brain tissue showed that the electronics unfolded after 5 weeks and settled into the hippocampus region with little interruption to the layered structure of neurons (**Fig. 5-15d** and **e**). Immunostaining imaging shows little proliferation of astrocytes around the electronics and the neurons appear to form tight junction with the outer surface of the injected electronics (**Fig. 5-15f**).

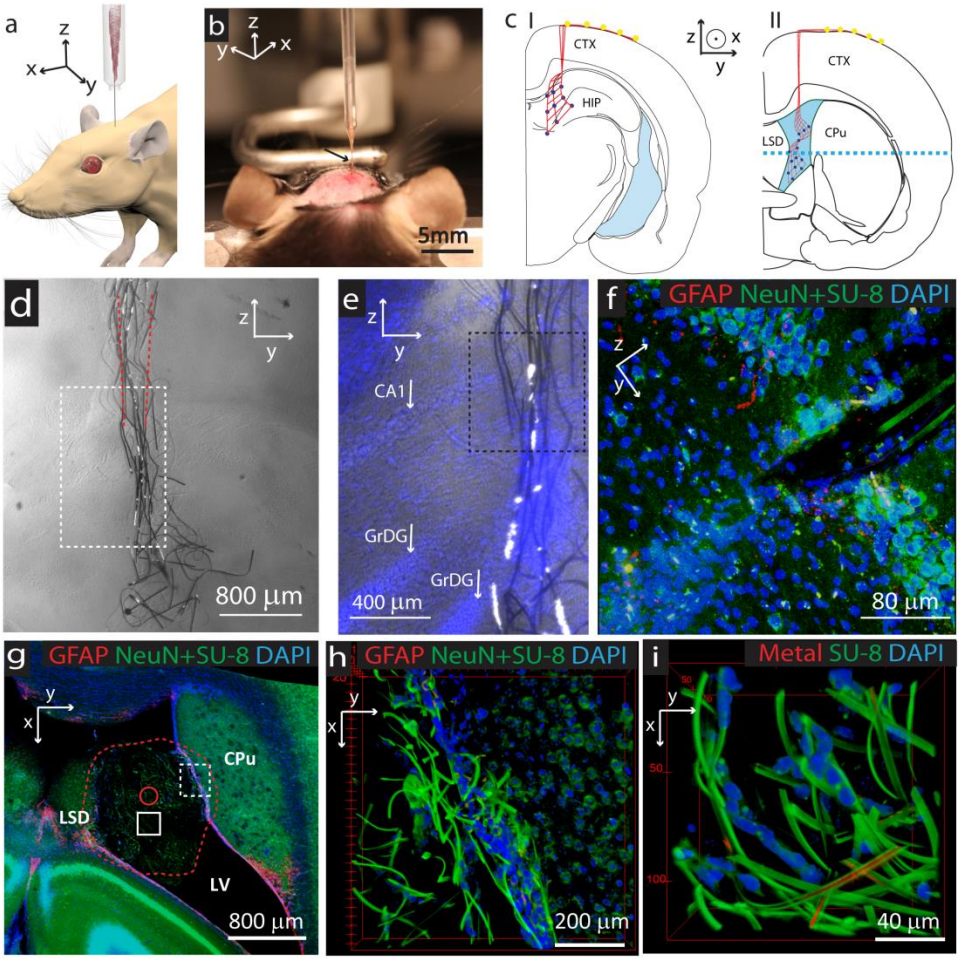

Figure 5-15 Injectable electronics in biological system. **a**, Schematic shows stereotactic injection of injectable electronics into *in-vivo* system. **b**, Optical image shows the stereotactic injection of injectable electronics into mice brain tissue. **c**, Schematics of coronal slices show that injectable electronics are injected into cerebral cortex (CTX) and hippocampus (HIP) region of brain (**I**), and the cavity of Lateral Ventricle (LV) beside caudoputamen region (CPu) and lateral septal nucleus (LSD) with unfolding (**II**). Red: mesh structure of injectable electronics, blue: nanodevices or metal electrodes on injectable electronics and yellow: I/O pads for electrical connections. Blue dashed lines indicate direction of horizontal slicing for imaging. **d**, Bright-field image of coronal slice in (**c, I**) shows the electronics was injected into the cortex and hippocampus region. Red dashed lines indicate the boundary of glass needle. **e**, Overlaid bright field and epi-fluorescence image of white dashed box highlighted region in d. Blue: DAPI. White arrows indicate the different layers of cells in hippocampus. GrDG: granular layer dentate gyrus and CA3: field CA3 of hippocampus. **f**, Projection of 30 um thick volume from the zoomed-in region by black dashed box in e shows neural cells interface with electronics. **g**, Projection of 100 um thick volume for the electronics injected into LV inside brain at the position indicated by blue dashed line in (**c, II**). Red dashed line highlights the boundary of unfolded mesh inside LV. Red circle indicates the size of the needle for injection. **h**, 3D render of the zoomed-in region highlighted by white dashed box in (**g**)

(Continued) shows the interface between nanoelectronics and subventricular zone. **i**, 3D render of the zoomed-in region highlighted by white box in (**g**).

To further demonstrate the potential of the geometrical restoration of the injectable electronics in cavity as well as its uniqueness for potential applications in cell therapy, we injected electronics into the cavity of the lateral ventricle to target the subventricular zone region because cells in this region have been proved to have capability of regeneration and long-distance migration[33], and potential for neuronal replacement therapy[34-35]. The same electronics as above was stereotaxically injected into the lateral ventricle region through a 200-μm glass needle (**Fig. 5-15c, II**). Since the behavior of electronics in solution is similar to that of synthetic polymeric networks, we can continuously inject a relatively large amount of electronics into the lateral ventricle to ensure that injected electronics, when unfolding, can be in contact with the lateral ventricle wall. After 5 weeks, immunostaining of horizontal slice showed that electronics unfolded into a volume with 1.5-mm diameter covering the inner area of lateral ventricle and connecting to the lateral walls. Immunostaining shows that the ribbons from electronics in contact with the caudoputamen interpenetrate with cells merging into the astrocytic-characteristic tube-like structure (**Fig. 5-15g-i**)[33]. Control experiment from the same rodent shows same level of glial fibrillary acidic protein (GFAP) expression demonstrating little chronic tissue response to the electronics. Importantly, there is migration of neural outgrowth cells from both sides of the lateral ventricle into the interior space of the unfolded mesh in the cavity. Those cells formed high density and tight junctions on the ribbons of electronics in chain-structures, which followed the direction of ribbons from electronics (**Fig. 5-16**). These results together with the capability of electronics to monitor cellular electrophysiological and pharmacological

activity show a potential application to use injectable electronics to directly mobilize and monitor the adult stem neurons from lateral ventricle region to brain injury for therapy.

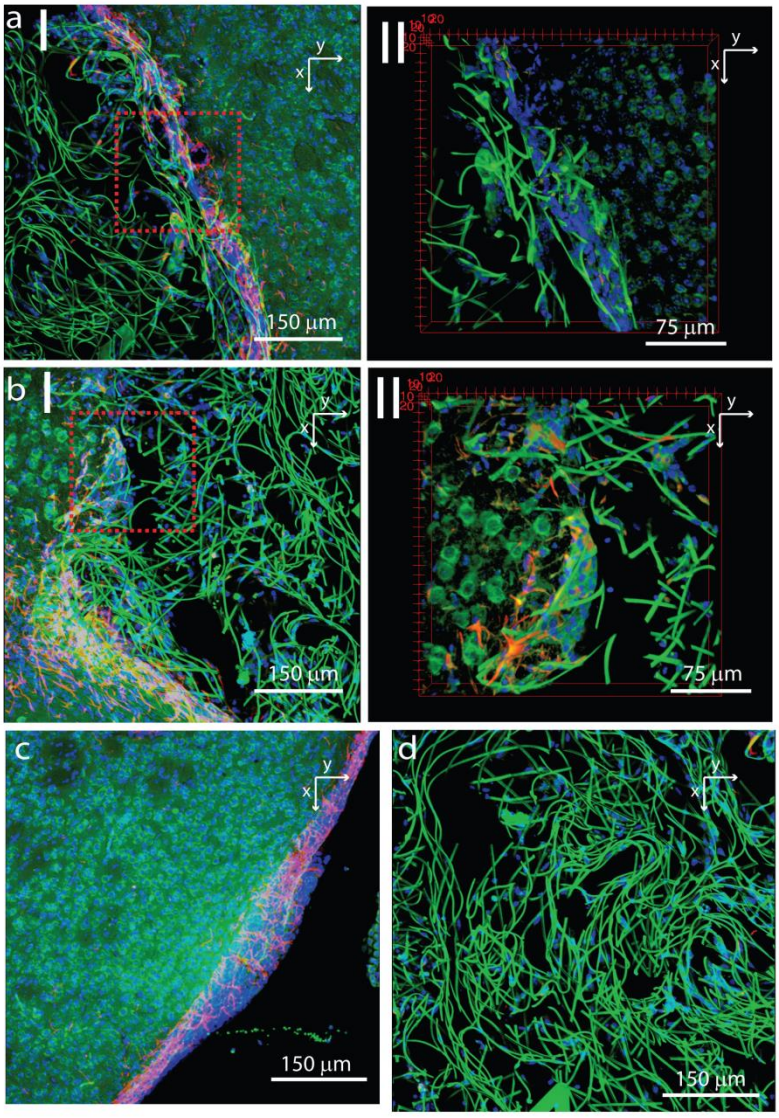

Figure 5-16 Interface between electronics and tissue in in-vivo system. a, Projection of 30 um thick volume of slice shows the interface between electronics in **in-vivo** with subventricular zone (**I**) and 3D render of red dashed box highlighted zoomed-in region (**II**). **b**, Projection of 30 um thick volume of slice shows the interface between electronics in in-vivo with staria (**I**) and 3D render of red dashed box highlights zoomed-in region (**II**). Blue: DAPI, green: SU-8 and NeuN and red: GFAP. **c**, Control sample shows subventricular zone without device. **d**, Projection of 80 um thick volume for the region highlighted by white box in **Fig. 5-15 g**. Blue: DAPI, green: SU-8 ribbon and neurons and red: GFAP.

5.4 Conclusion

The methods and mechanical designs introduced here represent new concepts for electronics fabrication and delivery. The future potential development is to (1) increase the complexity of electronics while keeping its nanoscale-thickness to maintain the syringe injectable property, (2) investigate different materials as supporting materials for injectable electronics to achieve the subsequent dissolving of materials releasing the sensing unit inside the injected subject to allow those unit to behave like colloidal in the subject for better integration, (3) further develop a non-surgical implantation bioelectronics and (4) create cellular therapy by using injectable electronics as scaffold for stem cell delivery, mobilization and monitoring.

5.5 Bibliography

1. Reuss, R. H., Hopper, D. G. & Park, J. *MRS Bull.* **31**, 447 (2006).
2. Thakor, N. V. *Sci. Transl. Med.* **5**, 210ps17 (2013).
3. Kim, D. H. *et al. Science* **320**, 507 (2008).
4. Kaltenbrunner, M. *et al. Nature* **499**, 458 (2013).
5. Timko, B. P. *et al. Nano Lett.* **9**, 914 (2009).
6. Cherenack, K. & van Pieterson, L. *J. Appl. Phys.* **112**, 091301 (2012).
7. Kim, D. H. *et al. Science* **333**, 838 (2011).
8. Tian, B. *et al. Nature Mater.* **11**, 986 (2012).
9. Rousche, P. J. *et al. IEEE Trans. Biomed. Eng.* **48**, 361 (2001).
10. Kim, T. *et al. Science* **340**, 211 (2013).
11. Troyk, P. P. *Annu. Rev. Biomed. Eng.* **1**, 177 (1999).
12. Liu, J. *et al. Proc. Natl. Acad. Sci. USA* **110**, 6694 (2013).

13. Alivisatos, P. A. *et al. ACS nano* **7**, 1850 (2013).

14. Deisseroth, K. & Schnitzer, M. J. *Neuron* **80**, 568 (2013).

15. Bencherif, S. A. *et al. Proc. Natl. Acad. Sci. USA* **109**, 19590 (2012).

16. Hillel, A. T. *et al. Sci. Transl. Med.* **3**, 93ra67 (2011).

17. Bible, E. *et al. Nature Protoc.* **4**, 1440 (2009).

18. Davidson, B. L. & Breakefield, X. O. *Nat. Rev. Neurosci.* **4**, 353 (2003).

19. Cui, Y., Wei, Q., Park, H. & Lieber, C. M. *Science* **293**, 1289 (2001).

20. Lieber, C. M. & Wang, Z. L. *MRS Bull.* **32**, 99 (2007).

21. Du, J., Roukes, M. L. & Masmanidis, S. C. *J. Micromech. Microeng.* **19**, 075008 (2009).

22. Patolsky, F., Zheng, G. & Lieber C. M. *Nat. Protoc.* **1**, 1711 (2006).

23. Qing, Q. *et al. Nat. Nanotechnol*. **9**, 142 (2014).

24. Lee, H., Bellamkonda, R. V., Sun, W. & Levenston, M. E. *J. Neural Eng.* **2**, 81 (2005).

25. Steif, P. S. *Mechanics of Materials.* (Pearson, 2012).

26. Sen, S., Subramanian, S. & Discher, D. E. *Biophys. J.* **89**, 3203 (2005).

27. Dai, J., Sheetz, M. P., Wan, X. & Morris, C. E. *J. Neurosci.* **18**, 6681 (1998).

28. Yoshida Kozai, T. D. *et al. Nat. Mater.* **11**, 1065 (2013).

29. Seri, B. *et al. J. Neurosci.* **21**, 7153 (2001).

30. Koiter, W. T. *Elastic Stability of Solids and Structures*. (Cambridge University Press, 2008).

31. Tada, H., Paris, P. C. & Irwin, G. R. *Stress Analysis of Cracks Handbook.* (ASME Press, 2000).

32. Selby, K. & Miller, L. E. *J. Mater. Sci.* **10**, 12 (1975).

33. Alvarez-Buylla, A. & Carcia-Verdugo, J. M. *J. Neurosci.* **22**, 629 (2002).

34. Cuitis, M. A., Faull, R. L. M. & Eriksson, P. S. *Nat. Rev. Neurosci.* **8**, 712 (2007).

35. Goldman, S. *Nat. Biotechnol.* **23**, 862 (2005).